Novel Transition Metal Molybdates for Catalytic Oxidative Dehydrogenation

By

DORON LEVIN

M. S. Chemical Engineering Practice, Massachusetts Institute of Technology, 1995
B. Sc. Honors (Operations Research), University of South Africa, 1993
B. Sc. Engineering (Chemical), University of the Witwatersrand, 1991

Submitted to the Department of Chemical Engineering
in Partial Fulfillment of the Requirements for the Degree of

DOCTOR OF PHILOSOPHY

in Chemical Engineering

at the

MASSACHUSETTS INSTITUTE OF TECHNOLOGY

June 1997

Signature of Author.....
Department of Chemical Engineering, May 14, 1997

Certified by.....
Jackie Y. Ying
Raymond A. and Helen E. St. Laurent Associate Professor
Thesis Advisor

Accepted by.....
Robert E. Cohen
St. Laurent Professor of Chemical Engineering
Chairman, Committee for Graduate Students

Novel Transition Metal Molybdates for Catalytic Oxidative Dehydrogenation

by

Doron Levin

Submitted to the Department of Chemical Engineering
on May 14, 1997 in Partial Fulfillment of the
Requirements for the Degree of Doctor of Philosophy
in Chemical Engineering

ABSTRACT

Catalytic oxidative dehydrogenation of lower alkanes is important as an alternative low-temperature processing route for the production of alkenes from feedstocks of low-cost saturated hydrocarbons. The catalyst needs to be active at low temperature to minimize total oxidation of the hydrocarbons. The catalysts investigated can be represented by the formula $A_{1+\delta}Mo_{1-\delta/3}O_4$, where A is a transition metal such as nickel, cobalt or zinc, and $-1/5 \leq \delta \leq 1/3$. The catalysts were synthesized by calcination of layered ammonium transition-metal molybdate (LTM) materials having a general formula $(NH_4)H_{2x}A_{3-x}O(OH)(MoO_4)_2$, where A is the transition metal and $0 \leq x \leq 3/2$. These LTM phases can be synthesized by a novel *chimie douce* synthesis technique from calcined layered double hydroxide precursors, or via precipitation. The structure of the nickel member of this LTM series was solved, *ab initio*, from powder X-ray data using a combination of 3-dimensional Patterson and Difference Fourier techniques, and refined using the Rietveld method. The location of the transition metals on a crystallographic site of variable occupancy allowed for careful manipulation of the chemical composition of these precursors. The transition metal/molybdenum ratio of the precursor is inherited by the catalyst, leading to single phase non-stoichiometric molybdates under reaction conditions for the entire range of transition metal/ molybdenum ratios studied. These catalysts were tested for the catalytic oxidative dehydrogenation of propane. The effect of the choice of transition metal (A) and the extent of non-stoichiometry (δ) were studied. The maximum overall yield and the activities of the catalysts are highly sensitive to the catalyst composition and the amount and nature of the oxidant used. AC Impedance Spectroscopy was used to correlate the electronic nature of the catalyst surface to the defect chemistry of the material. The electronic properties of the catalyst serves to influence both the nature and the extent of the oxygen surface coverage, with a more reactive surface coverage leading to higher propane conversion. Knowledge of the structure-property relationship of these materials facilitated the optimization of catalytic activity through the ability to design new catalysts by molecular-level engineering.

Thesis Advisor: Jackie Y. Ying
Title: Raymond A. and Helen E. St. Laurent Associate Professor

ACKNOWLEDGMENTS

Looking back over the last 5 years, I realize that my time spent at graduate school was very influential in my intellectual and emotional development. There were many people over this time frame who, for better or worse, had a direct bearing on my experiences here, and while I will mention those who had the greatest impact, I would like to apologize to anyone who feels slighted by their omission. First and foremost, I would like to acknowledge Prof. Jackie Ying for her support and guidance during my time her at M.I.T. Her enthusiasm for research and her willingness to allow me to pursue a new research area are greatly appreciated. Her support of my work and constructive criticism thereof contributed to the development of this thesis. I would also like to thank the members of my thesis committee: Prof. Klavs Jensen, Prof. Charles Satterfield, and Prof. Bernhardt Wuensch for their advice over the course of this thesis.

I would also like to acknowledge the help, guidance, encouragement and friendship of Dr. Stuart Soled at Exxon. This thesis developed from the research I undertook during the Summer of 1993 at the Corporate Research Laboratories of Exxon, and the contributions of Stu Soled are greatly appreciated.

In my years in the Nanostructured Materials Research Group, I have had the pleasure of interacting with many talented, bright individuals. They are Postdoctoral associates: Andreas Tschöpe, Tao Sun, and Christian Mehnert, and Graduate students: Kenneth Bryden, Darren Castro, Lei Zhang, Larry Panchula, Mark Fokema, Michael Wong, and Andrey Zarur. I thank all of them for their friendship and their help around the lab. I would also like to acknowledge the help of Jennifer Pell, David Bem, and Joel Houmes during the stage of my research that was more Chemistry than Chemical Engineering. I would also like to acknowledge the assistance of Ron Kuse, William Tran, and William Engmann for their research contributions towards understanding the chemistry of layered double hydroxide materials. I would especially like to thank Dr. Andreas Tschöpe for his assistance at the initial, and most difficult stage, of my research.

I would also like to acknowledge the great job that Linda Mousseau and Ellen Weene did in handling the day-to-day administrative tasks of the group. I'd also like to thank Elaine Aufiero and Janet Fischer in the student office for their assistance during my stay here at M.I.T. Financial support of the National Science Foundation (CTS-9257223 and CTS-9411901) is appreciated.

I would also like to mention some of the people who showed me that there was life beyond the hallowed halls of M.I.T., and the list includes Aviva Cowen, Michael Zatman, Andrew Yablon, Dalia Trachtenberg, Debbie Fass, Robin Michnick, and numerous other members of the community at Harvard Hillel.

Last, but not least, the love and support of my parents and my family across the miles that physically separated us gave me the strength and encouragement to complete this thesis.

TABLE OF CONTENTS

1. INTRODUCTION 9
1.1. Background 9
1.2. Pillaring of Layered Materials 10
1.3. Transition Metal Molybdates and their Use as Catalysts 11
1.4. Oxidative Dehydrogenation of Propane 14
1.5. Thesis Objectives 15

2. SYNTHESIS AND CHARACTERIZATION OF LAYERED TRANSITION METAL MOLYBDATES 16
2.1. *Chimie Douce* Synthesis of a Layered Ammonium Zinc Molybdate 16
2.1.1. Introduction 16
2.1.1.1. Structure of LDH Precursor 16
2.1.1.2. Thermal Decomposition of Layered Double Hydroxide Precursor 17
2.1.1.3. Reconstitution of Layered Double Hydroxides - "Memory Effect" 18
2.1.2. Experimental Synthesis 19
2.1.2.1. Preparation of the Metastable Mixed Oxide Precursor 19
2.1.2.2. *Chimie Douce* Synthesis of Zn-LTM 21
2.1.3. Characterization of Zn-LTM 22
2.1.4. Generality of the *chimie douce* reaction for the synthesis of LTM materials 24
2.2. Synthesis of a Layered Ammonium Nickel Molybdate by Chemical Precipitation 26
2.2.1. Introduction 26
2.2.2. Experimental Synthesis 27
2.2.3. Characterization 27

3. CRYSTAL STRUCTURE DETERMINATION OF LAYERED TRANSITION METAL MOLYBDATES 31
3.1. Introduction 31
3.2. Crystal Structure Determination by Rietveld Refinement 31
3.2.2. Solution and Refinement of the Ni-LTM Structure 32
3.2.3. Solution and Refinement of Zn-LTM Structure 36
3.3. Description of LTM Crystal Structure 39
3.3.1. General Structure 39
3.3.2. Assignment of Hydrogen Atoms 42
3.4. Solid Solution Series 48
3.5. The Relationship between the LTM and LDH Crystal Structures 52

4. NON-STOICHIOMETRIC TRANSITION METAL MOLYBDATES FROM LTM PRECURSORS 54
4.1. Synthesis 54
4.2. Characterization of Transition Metal Molybdates Prepared from LTM Precursors 55
4.2.1. X-Ray Diffraction (XRD) 56
4.2.2. B.E.T. Surface areas 57
4.2.3. Diffuse Reflectance Infrared Fourier Transform (DRIFT) Spectroscopy 58
4.2.4. Electrical Conductivity 58
4.2.4.1. Theory 58
4.2.4.2. Conductivity Dependence on Oxygen Partial Pressure .. 61
4.2.4.3. Experimental Setup 63
4.2.4.4. Impedance Measurements 66
4.3. Phase Determination of Non-Stoichiometric Nickel Molybdates 67
4.4. Surface Area Determination of Non-Stoichiometric Nickel Molybdates 72
4.5. Modeling the Defect Structure of Non-Stoichiometric Nickel Molybdates 73
4.5.1. Balance Relationships for Ionic Point Defects in Ternary Molybdates .. 74
4.5.2. The Defect Structure of Non-Stoichiometric Nickel Molybdate 77
4.6. Electronic Properties of Non-Stoichiometric Nickel Molybdates 78
4.6.1. Experimental Results 79
4.6.2. Correlation of Conductivity Data with Defect Structure of $Ni_{1-\delta}Mo_{1-\delta/3}O_4$ 85

5. OXIDATIVE DEHYDROGENATION OF PROPANE BY NON-STOICHIOMETRIC TRANSITION METAL MOLYBDATES 87
5.1. Experimental 87
5.1.1 Determination of Steady-State Activity 87
5.1.2. Determination of Transient Catalytic Behavior 88
5.2. ODH of Propane Using Oxygen as the Oxidant 90
5.2.1. Effect of Transition Metal in Stoichiometric Transition Metal Molybdates 90
5.2.2. Effect of Non-Stoichiometry in the Ni-Mo-O System 91
5.2.3. Effect of Oxygen:Propane Ratio 94
5.3. ODH of Propane Using Nitrous Oxide as the Oxidant 95
5.3.1. Steady-State Results: Effect of Non-Stoichiometry 97
5.3.2. Effect of Nitrous Oxide:Propane Ratio 98
5.4. Pulse Experiments: Effect of Non-Stoichiometry 100
5.5. Structure/Catalytic Property Relationship 102

6. CONCLUSIONS AND FUTURE DIRECTIONS 107

7. REFERENCES 109

LIST OF FIGURES

Figure 1.1. Structure of α-$MnCoMoO_4$, shown in polyhedron representation. 13
Figure 1.2. Structure of α-$CoMoO_4$, showing chains of close-packed octahedra. 13
Figure 2.1. Schematic representation of LDH. 17
Figure 2.2. Powder X-ray diffraction pattern of a) $Zn_4Al_2(OH)_{12}CO_3 \cdot 4H_2O$, and b) the calcined LDH precursor. 20
Figure 2.3. Change in pH during *chimie douce* reaction. 22
Figure 2.4. PA-FTIR spectrum of Zn-LTM 23
Figure 2.5. Powder X-ray diffraction pattern of Zn-LTM. 24
Figure 2.6. ^{27}Al NMR spectra of a) calcined $Zn_4Al_2(OH)_{12}CO_3 \cdot 4H_2O$ and b) calcined $Mg_4Al_2(OH)_{12}CO_3 \cdot 4H_2O$. 26
Figure 2.7. Powder X-ray diffraction pattern of Ni-LTM. 28
Figure 2.8. PA-FTIR spectrum of ammonium nickel molybdate. 29
Figure 2.9. FT-Raman spectrum of Ni-LTM. 30
Figure 3.1. X-ray diffraction patterns of a) Zn-LTM, and b) $(NH_4)HNi_2(OH)_2(MoO_4)_2$, showing isostructural relationship. 32
Figure 3.2. Synchrotron powder X-ray data, including Rietveld fit and residuals for $(NH_4)HNi_2(OH)_2(MoO_4)_2$. The set of short vertical bars below the data set indicates the position of possible Bragg reflections. 34
Figure 3.3. Powder X-ray data, including Rietveld fit and residuals for Zn-LTM. The set of short vertical bars below the data set indicates the position of possible Bragg reflections. 37
Figure 3.4. Basal plane of $(NH_4)HNi_2(OH)_2(MoO_4)_2$, viewed along [001]. 41
Figure 3.5. Crystal structure of Ni-LTM, viewed along [010], showing three-layer arrangement in polyhedron representation. 43
Figure 3.6. Crystal structure of Ni-LTM, viewed in polyhedron representation. 44
Figure 3.7. Difference Fourier map showing partial (010) plane. Successive contour lines differ by 0.3 $e^-/Å^2$. Dashed contours are negative. 46
Figure 3.8. Possible locations for framework hydrogens: (a) in tetrahedral site associated with bridging hydroxyl; (b) as bridging water. 48
Figure 3.9. Difference Fourier map showing partial (010) plane. Successive contour lines differ by 0.3 $e^-/Å^2$. Dashed contours are negative. Difference Fourier map calculated for $\mathbf{R}_{wp} = 13.5\%$, $\mathbf{R}_p = 10.4\%$. 49
Figure 3.10. Arrangement of tetrahedral and octahedral sites within the unit cell area. 51
Figure 3.11. Variation in the number of cations in octahedral coordination resulting from *chimie douce* reaction. 53
Figure 4.1. Weight loss as a function of temperature for the $(NH_4)HNi_2(OH)_2(MoO_4)_2 \rightarrow NiMoO_4$ transformation. 56
Figure 4.2. Derivative of heat flow (mW/min) for calcination of Ni-LTM phases. 57

Figure 4.3. RC-circuit diagram for single resistor and capacitor in parallel. 60
Figure 4.4. Impedance plane plot for a depressed circular arc. 61
Figure 4.5. Schematic of apparatus for conductivity measurements. 64
Figure 4.6. Schematic of sample holder for electrical conductivity measurements. 65
Figure 4.7. XRD patterns collected at 550 °C following *in situ* calcination of precursors with a Ni/Mo ratio of (a) 0.75, (b) 1.0, and (c) 1.5. 68
Figure 4.8. Simulated diffraction pattern of β-$NiMoO_4$. The set of short vertical bars below the pattern indicate the position of possible Bragg reflections. 70
Figure 4.9. XRD patterns of (a) α-$NiMoO_4$ derived by precalcining Ni-LTM at 550 °C, scanned at 25 °C, (b) material in (a) reheated to 550 °C, and (c) material in (a) heated to 700 °C. 71
Figure 4.10. DRIFT spectra collected at 550 °C following *in situ* calcination of precursors with a Ni/Mo ratio of (a) 0.75, (b) 1.0, and (c) 1.5. 72
Figure 4.11. Impedance data for $Ni_{0.903}Mo_{1.032}O_4$ at 587 °C in 1 kPa of O_2. 81
Figure 4.12. Conductivity of $Ni_{0.8}Mo_{1.067}O_4$ in 1 kPa and 10 kPa O_2, displaying Arrhenius-type behavior. 82
Figure 4.13. Dependence of conductivity on oxygen partial pressure (kPa) for materials with Ni/Mo ratios of 0.75, 1.0, and 1.5. 83
Figure 4.14. Conductivity of $Ni_{0.8}Mo_{1.067}O_4$ displaying Arrhenius-type behavior in format for the determination of E_a. 84
Figure 4.15. Dependence of conductivity on N_2O partial pressure (kPa) for the material having a Ni/Mo ratio of 0.75. 85
Figure 5.1. Schematic of reactor setup. 89
Figure 5.2. Propene yield as a function of Ni content (ϵ) for $Ni_\epsilon Co_{1-\epsilon}MoO_4$ catalysts. 91
Figure 5.3. Propane conversion as a function of Ni content (ϵ) for $Ni_\epsilon Co_{1-\epsilon}MoO_4$ catalysts. 92
Figure 5.4. Product selectivity as a function of Ni content (ϵ) for $Ni_\epsilon Co_{1-\epsilon}MoO_4$ catalysts. 92
Figure 5.5. Propene yield as a function of Ni/Mo ratio. 93
Figure 5.6. Selectivity towards propene at 20 % propane conversion. 94
Figure 5.7. Propene yield as a function of Ni/Mo ratio and feed O_2:C_3H_8 ratio. 95
Figure 5.8. Propane conversion as a function of Ni/Mo ratio and feed O_2:C_3H_8 ratio. 96
Figure 5.9. Propene yield as a function of Ni/Mo ratio. 97
Figure 5.10. Propene yield as a function of Ni/Mo ratio for O_2 and N_2O as oxidants. 98
Figure 5.11. Propene yield as a function of Ni/Mo ratio and feed N_2O:C_3H_8 ratio. 99
Figure 5.12. Propane conversion as a function of Ni/Mo ratio and feed N_2O:C_3H_8 ratio. . . . 100
Figure 5.13. Concentration profiles of all species in pulse experiment. 101
Figure 5.14. N_2 concentration profiles in pulse experiments over catalysts having a Ni/Mo ratio of 0.75 (●), 0.875 (■), 1.0 (▾), and 1.5 (▴). 103

LIST OF TABLES

Table 3.1. Final Positional and Thermal Parameters for Ni-LTM 35
Table 3.2. Crystallographic data for $(NH_4)HNi_2(OH)_2(MoO_4)_2$ from Rietveld Refinement of powder X-ray diffraction data 35
Table 3.3. Final Positional and Thermal Parameters for Zn-LTM 38
Table 3.4. Crystallographic data for $(NH_4)HZn_2(OH)_2(MoO_4)_2$ from Rietveld Refinement of powder X-ray diffraction data 38
Table 3.5. Selected Interatomic Distances for $(NH_4)HA_2(OH)_2(MoO_4)_2$ 40
Table 3.6. Selected Interatomic Angles 40
Table 3.7. Calculated Hydrogen Positions 45
Table 3.8. Variables defining the compositions of structures having the general formula $(NH_4)H_{2x}Ni_{3-x}O(OH)(MoO_4)_2$ 50
Table 4.1. Catalysts Derived from $(NH_4)HA_{2\epsilon}B_{2-2\epsilon}(OH)_2(MoO_4)_2$ Precursors 54
Table 4.2. Catalysts Derived from $(NH_4)H_{2x}Ni_{3-x}O(OH)(MoO_4)_2$ Precursors 55
Table 4.3. Structure Model for β-$NiMoO_4$ 69
Table 4.4. B.E.T. Surface Areas of $Ni_{1+\delta}Mo_{1-\delta/3}O_4$ Series Catalysts 73
Table 4.5. Kröger and Vink Notation for Some Defects in Ni-Mo-O System 74
Table 4.6. Ionic Disorder Types with Two Different Kinds of Point Defects 76
Table 4.7. Defect Concentration Relations for Cationic Disorder Types in $NiMoO_4$ 77
Table 4.8. Activation Energy of Conduction at 1 kPa O_2 83

1. INTRODUCTION

1.1. Background

The synthesis of catalysts has often been described as an art, with a series of detailed and sometimes arcane processing procedures needed to be followed in order to ensure good reproducibility of catalyst performance.[1] The scientific development of new catalysts has certainly progressed a great deal away from the "try-everything-on-the-shelf" approach of the early twentieth century. However, the fundamental relationship between catalyst properties and catalyst performance remains unclear for most systems. As a result, catalyst research typically follows the path of synthesis of new catalytic phases followed by extensive characterization of the catalyst and investigations into the reaction mechanism to explain the observed performance. Despite significant improvements in characterization techniques over the past two decades, a true understanding of the events taking place on a catalyst surface remains an enigma.

The main objectives in the design of a catalyst for a specific reaction are the maximization of catalytic activity and selectivity. Typically, activity and selectivity are inversely correlated, with gains in activity usually coming at the expense of a loss in selectivity. There are two main features of a catalyst that determines its activity and selectivity. The first feature is the intrinsic activity of the catalyst structure itself that is mainly a function of the microscopic catalyst composition. The composition of the catalyst, especially that of the surface regions, affects its ability to interact with a reactant molecule in the desired manner. Superimposed on this intrinsic activity is an influencing parameter determined by the overall morphology of the macroscopic catalyst structure. The ability of a reactant molecule to reach an active site on the catalyst surface, as well as the ability of the product molecule to diffuse away from the active site will influence the overall yield. The catalyst morphology may pose further restrictions on the reactions that take place by limiting certain transition-state configurations due to steric hindrance, as occurs with certain reactions taking place on some zeolite catalysts. An understanding of these two catalyst features is important to be able to engineer desired properties into a catalyst.

The field of catalyst synthesis is certainly very varied. An area that has received increased attention is the development of catalytic materials from layered precursors. Interest in this area can be attributed to the search for shape-selective catalysts that overcome the small pore diameter

limitation of alumino-silicate- and alumino-phosphate-based zeolites. The desire to use lamellar precursors to host catalytically active species arose from the idea that individual active sites could be isolated on "pillars" or molecular props between these sheets of atoms forming the lamellar host, and by controlling the distribution of these molecular props, shape selectivity can be engineered into a catalyst structure.

1.2. Pillaring of Layered Materials

Pillared layered structures (PLS) are derivative materials prepared by linking molecules to a layered host. The process referred to as "pillaring" involves the intercalation of a robust, bulky molecule into a lamellar host with the concomitant expansion of the host structure in a uniaxial direction such that the basal spacing increases to a value comparable to the van der Waal's dimension of the guest species. Pillared layered structures are an excellent example of materials by design. Synthesis of these PLS can be accomplished by modification of the host-structure chemical composition, chemical or structural modification of the interlayer region, or both.

There has been extensive research into the preparation of PLS, focused mainly on structural modification of the interlayer region. Examples include the pillaring of smectites, such as montmorillonite, by ion-exchange with polycationic species, e.g. Al_{13}-polyhydroxypolymer $(Al_{13}O_4(OH)_{24}(H_2O)_{12})^{7+}$,[2-7] Zr-hydroxypolymers $(Zr_4(OH)_8(H_2O)_{16})^{8+}$,[8-9] and other oligocations. One common feature of these materials, termed cross-linked smectite (CLS) molecular sieves, or pillared interlayered clays (PILC), is that they are prepared without chemical modification of the host composition. Other examples of PLS prepared by modification of only the interlayer region include the pillaring of layered double hydroxides (LDHs), also known as hydrotalcite-like materials or anionic clays, by various anionic species. Examples include the pillaring of LDHs with polyoxometalate (POM) anions of the $[XM_{12}O_{40}]^{m-}$ or Keggin ion type by direct anion exchange,[10-15] or utilizing an organic anion-pillared precursor that was subsequently exchanged with the appropriate isopolymetalate under mildly acidic conditions.[16-17] To the best of my knowledge, however, no new layered structure had been prepared by the simultaneous modification of both the chemical composition of the host structure and the interlayer region.

There has been considerable interest in the use of polyoxometalate ions that have a Keggin or Dawson ion structure as the interlayer species. The reason for this lies in the variety of

catalytically active metals that form these complex bulky ions by the linking of M-O polyhedra. In particular, compounds of Groups 5 and 6 transition metals such as vanadium and molybdenum are known to be catalytically active for a wide variety of different reactions. For example, hydro-desulfurization of petroleum on molybdenum containing catalysts is one of the largest heterogeneous catalytic processes employed world-wide.[18] Molybdenum-based catalysts are also active for coal liquefaction,[19] a process of increasing industrial importance. The application of molybdenum-based catalysts for the selective oxidation of olefins to unsaturated aldehydes and acids, and the use of bismuth molybdate for the synthesis of acrylonitrile by ammoxidation of propene[20] are further examples of the versatility of molybdenum compounds for catalytic applications.

1.3. Transition Metal Molybdates and their Use as Catalysts

There are two main properties that make the chemistry of molybdates so rich: i) molybdenum can appear in either octahedral or tetrahedral coordination in a variety of structures, and ii) polymolybdates can be formed in which the MoO_3/MO ratio, where M is a transition metal, is high. In general, polymolybdates formed by solid state reactions are composed of chains of Mo-O polyhedra, whereas polymolybdates formed by precipitation from aqueous media tend to form complex and bulky polymolybdate ions that may be isolated from each other by M-O polyhedra.[21]

The solution-based synthesis of first-row transition-metal molybdates yields an interesting array of phases. Pioneering work in this field by Pezerat and his coworkers identified a series of phases having ideal formulas $MMoO_4 \cdot H_2O$, $AHM_2O(MoO_4)_2 \cdot H_2O$, and $A_{2-x}(H_3O)_xM_2O(MoO_4)_2$,[22-26] where $A = NH_4^+$, Na^+, or K^+ and $M = Zn^{2+}$, Co^{2+}, or Ni^{2+}. Preparation of these phases was found to be dependent on the amount of base used and these phases were designated as Φ_c, Φ_x, and Φ_y respectively.[22] The crystal structures of phases Φ_x and Φ_y were determined by Pezerat from a limited number of reflections obtained from Weissenberg film data on very small crystals.[25] These materials were shown to exhibit variable and non-stoichiometric compositions. A theory of non-stoichiometry based on cationic and anionic vacancies compensated by the presence of protons was proposed.[25,26] This theory was investigated using phase Φ_x of a compound in which $A = K^+$ and $M = Mg^{2+}$.[27-30] However, the limited data used in the structure determinations (122 and 147 reflections for the Φ_x and Φ_y crystals respectively) and the large residuals ($R = 0.09$ for phase Φ_x) raised doubts as to the completeness of the structure determination. For this reason, a fundamental structural study of the phases Φ_x and Φ_y, for the compound in which $A = Na^+$ and $M = Zn^{2+}$, was initiated by Clearfield and

his coworkers about 10 years after the publication of Pezerat's work.[31,32] These studies confirmed the structure of phase Φ_x using a single crystal grown hydrothermally.[31] However, attempts to confirm the structure of phase Φ_y were unsuccessful due to the preparation of an alternate phase resulting from their synthesis conditions.[32] Subsequently, analogs of phase Φ_x, $NaM_2(OH)(H_2O)(MoO_4)_2$ (where M = Mn[33] and Ni[34]), and of the alternate phase $NaM(OH)(MoO_4)$ (where M = Cu[35]) were prepared using reflux and hydrothermal reactions and were characterized.

The transition metal molybdates most widely used in catalysis are molybdates of divalent transition metal cations that include Mn, Fe, Co and Ni. These molybdates, having a general formula $MMoO_4$, have the structure of phase Φ_c. This phase, however, has three different polymorphic representations:

i) type M of α-$MnMoO_4$,[36] that is monoclinic, space group C2/*m*, in which Mn is in octahedral coordination and Mo is in tetrahedral coordination. This structure, shown schematically in Figure 1.1, is composed of blocks of four edge-sharing MO_6 octahedra, linked together through isolated MoO_4 tetrahedra.

ii) type C of α-$CoMoO_4$,[37] that is monoclinic, space group C2/*m*, in which both Co and Mo are in distorted octahedral coordination. This structure is more compact than type M, and is about 6% denser than the corresponding α-$MnMoO_4$ isotype. The structure is built up of edge-sharing Co and Mo octahedra that form infinite chains parallel to the *c* axis, as shown in Figure 1.2. Each chain is joined to four other chains by corner sharing of oxygen atoms, with a displacement in the *c* direction of one octahedron of the central chain relative to its four neighbors. Between the filled chains occur chains of unfilled octahedra.

iii) type N of wolframite $NiWO_4$,[38] the high-pressure phase that is the most compact structure, being about 13-14% more dense than C isotypes and 19% more dense than M isotypes.[39] The structure can be considered as a distorted hexagonal close-packing of oxygen atoms with one quarter of the octahedral holes filled with M and Mo each.

Transition metal molybdates have been examined as multicomponent catalytic systems for a number of reactions. In particular, catalysts based on the combination of nickel, cobalt and molybdenum find wide use in hydrotreating reactions, such as hydrodesulfurization and hydrodenitrogenation.[1] There have been numerous studies on the Co-Mo-O system for the one-step oxidation of propene to acrylic acid.[21] In this system, activity for the partial oxidation of propene is suggested to be due to the dispersion of MoO_3 in the form of a thin layer over $CoMoO_4$, the

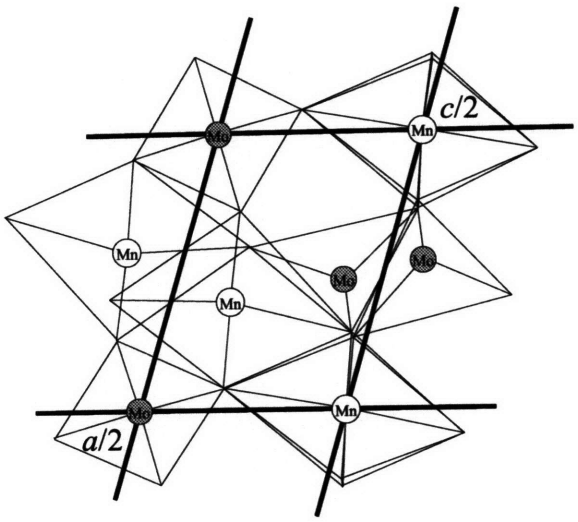

Figure 1.1. Structure of α-$MnMoO_4$, shown in polyhedron representation.

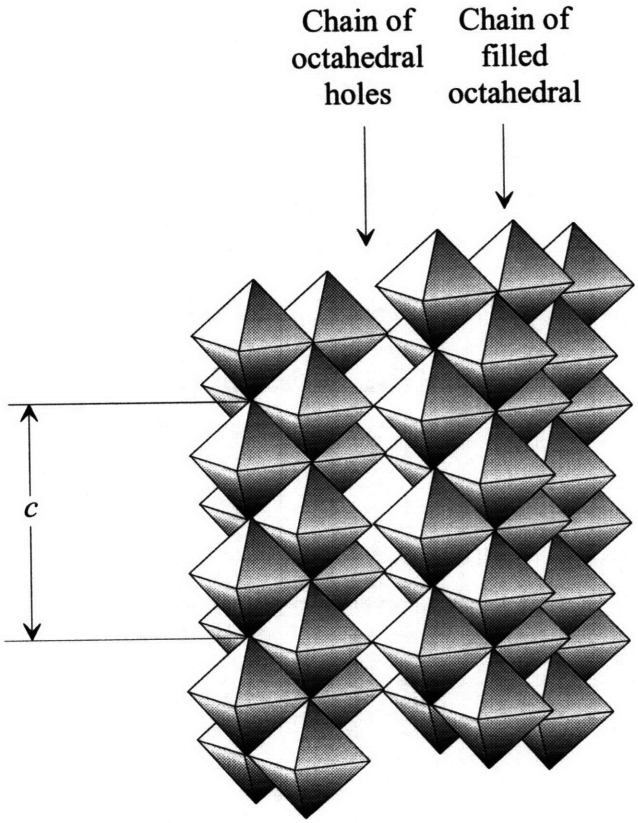

Figure 1.2. Structure of α-$CoMoO_4$, showing chains of close-packed octahedra.

catalyst being in fact MoO_3 supported on $CoMoO_4$. Excess MoO_3 has also been shown to be an important factor in the selective oxidation of butene to butadiene and maleic anhydride over Ni-Mo-O catalysts.[40] These examples illustrate the dependence of the catalyst activity on the M/Mo ratio, and suggests that careful attention needs to be placed on an understanding of the relationship between the molybdenum and transition metal content and their effect on catalytic performance. In addition to the selective oxidation of alkenes, transition metal molybdates are also known to be catalytically active for the oxidative dehydrogenation reactions of lower alkanes.

1.4. Oxidative Dehydrogenation of Propane

There has been increased industrial interest in the oxidative dehydrogenation (ODH) of paraffins to olefins,[41] due to several limitations in thermal and catalytic dehydrogenation processes. The thermodynamics of thermal dehydrogenation of light paraffins to olefins are such that under conditions of low temperature and high pressure, the equilibrium favors the paraffin. Catalytic dehydrogenation at elevated temperatures leads to undesirable side reactions such as cracking and coking of the catalyst. In addition, paraffin dehydrogenation is strongly endothermic, making the process extremely energy intensive. For example, dehydrogenation of propane to propene is given by:

$$C_3H_8 \rightarrow C_3H_6 + H_2 \qquad \Delta H_f^0 = +29.7 \text{ kcal/mol.} \qquad \textbf{(1.1)}$$

To supply the heat of reaction, hydrogen oxidation can be coupled with dehydrogenation:

$$C_3H_8 + \tfrac{1}{2}\, O_2 \rightarrow C_3H_6 + H_2O \qquad \Delta H_f^0 = -28.1 \text{ kcal/mol.} \qquad \textbf{(1.2)}$$

The addition of oxygen to the feed, however, exposes the synthesized olefins to oxidation conditions that could result in the formation of economically-useless carbon oxides:

$$C_3H_6 + 9/2\, O_2 \rightarrow 3\, CO_2 + 3\, H_2O \qquad \Delta H_f^0 = -460.4 \text{ kcal/mol} \qquad \textbf{(1.3)}$$

$$C_3H_6 + 3\, O_2 \rightarrow 3\, CO + 3\, H_2O \qquad \Delta H_f^0 = -257.5 \text{ kcal/mol.} \qquad \textbf{(1.4)}$$

Therefore, desired catalysts for oxidative dehydrogenation of lower alkanes need to be sufficiently active for hydrogen atom abstraction from a C-H bond, yet operate at temperatures that minimize oxygenation of the desired products.

A variety of catalysts have been studied for the oxidative dehydrogenation of propane,[41] with particular research interest focused on catalysts containing magnesium, vanadium and oxygen.[42-46] In addition, catalysts based on transition metal molybdates, typically bismuth, cobalt and nickel molybdates,[47-53] have received recent attention. Of the transition metal molybdates, those based on nickel, and in particular the stoichiometric $NiMoO_4$, have attracted the greatest interest. $NiMoO_4$ presents two polymorphic phases at atmospheric pressure: a low temperature α phase (type C, isostructural to α-$CoMoO_4$), and a high temperature β phase (type M, isostructural to α-$MnMoO_4$).[47,49,54] These phases differ primarily in the coordination of molybdenum that is distorted octahedral in the α phase and distorted tetrahedral in the β phase. It has been shown that cooling a β phase below 170 °C leads to a $\beta \rightarrow \alpha$ phase transition that requires reheating to 700 °C to reverse.[48] The β phase has been shown to be almost twice more selective in propene formation than the α phase for comparable conversion at the same temperature.[47] A similar effect has been noted for oxidative dehydrogenation of butane, with the β phase being approximately three times more selective in butene formation than the α phase.[55] The reason for the difference in selectivities is unknown, but the properties of the phases are known to be dependent on the precursors from which they are derived.

1.5. Thesis Objectives

The overall objective of this thesis is the development of a catalyst that is active for the oxidative dehydrogenation of lower alkanes. In particular, the oxidative dehydrogenation of propane into propene, a widely used polymer precursor, was chosen as the test reaction, with maximization of the propene yield being a major criterion. This thesis seeks not only the engineering of a catalyst for this reaction, but also the development of an understanding of the relationship between the catalyst properties and its synthesis history. By focusing on how the processing procedures and parameters affect the structures of the various precursors and the catalyst itself, phases that have optimal catalytic activity can be prepared. A knowledge of the relationship between the properties and the structure of the catalyst will provide a framework for the design of new catalysts by molecular-level engineering.

2. SYNTHESIS AND CHARACTERIZATION OF LAYERED TRANSITION METAL MOLYBDATES

2.1. *Chimie Douce* Synthesis of a Layered Ammonium Zinc Molybdate

2.1.1. Introduction

A novel room-temperature *chimie douce* synthesis technique that produced a member of the class of layered transition-metal molybdate (LTM) materials using calcined LDHs as precursors was discovered. In this synthesis, a new layered structure was prepared by the simultaneous modification of both the chemical composition of a layered host structure and the interlayer region. These new materials, while being related structurally to the original LDH, have undergone a modification of the host chemical composition with complete transformation of the interlayer region.

2.1.1.1. Structure of LDH Precursor

Layered double hydroxides (LDHs), or the so-called anionic clays are, in terms of charge, mirror images of the extensively studied family of cationic smectite clay minerals. The structure, synthesis, and properties of these materials have been extensively reviewed.[56]

The structure of LDHs, shown schematically in Figure 2.1, is very similar to that of brucite, $Mg(OH)_2$, where octahedra of Mg^{2+} (6-fold coordinated to OH^-) share edges to form infinite sheets. These sheets are stacked on top of each other and are held together by hydrogen bonding. Isomorphous substitution of a divalent cation in the lattice by a trivalent cation having similar radius results in a positive charge generated in the hydroxy sheet. This net positive charge is compensated for by incorporation of hydrated anions in the interlayer region.

The composition of LDHs is typically represented by the general formula:

$$[M^{II}_{(1-x)}M^{III}_{x}(OH)_2]^{x+}[A^{n-}_{x/n}\cdot zH_2O],$$

where A^{n-} is the gallery anion and M^{II} and M^{III} are the divalent and trivalent cations respectively. Typically M^{II} may be Mg^{2+}, Zn^{2+}, Ni^{2+}, Co^{2+}, Fe^{2+}, and M^{III} may be Al^{3+}, Cr^{3+}, Co^{3+} or Fe^{3+}. There is

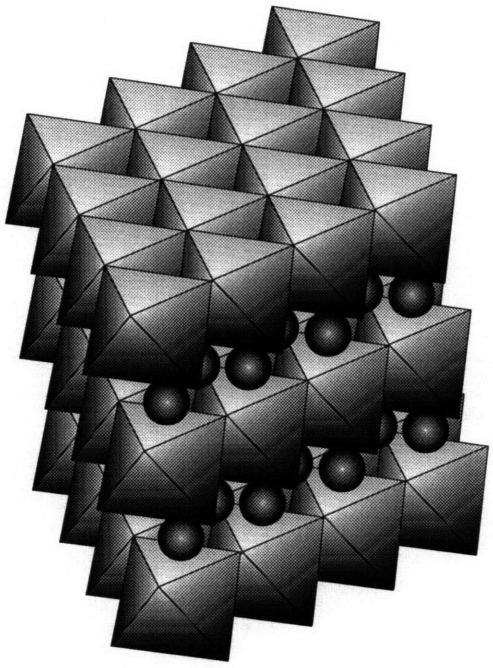

Figure 2.1. Schematic representation of LDH.

essentially no limitation to the nature of the anion and A^{n-} is typically CO_3^{2-}, NO_3^-, OH^-, or Cl^-. Many compositions are possible, depending on the combination of M^{II}, M^{III}, A^{n-}, and the layer cation stoichiometry. Typically, the trivalent cation substitution parameter, x, given by $M^{III}/(M^{II} + M^{III})$, is in the range of 0.17 to 0.33.

LDHs crystallize in either the $R\bar{3}m$ space group (rhombohedral phase) or the $P6_3/mmc$ space group (hexagonal phase). In the rhombohedral phase, three double-layers are present per unit cell, resulting in the hydroxyl stacking sequence BC-CA-AB-BC (where A, B, and C are the three threefold axes at x,y = 0,0; 2/3,1/3; and 1/3,2/3).[57] In the hexagonal phase, only two double-layers are present per unit cell, leading to a hydroxyl stacking sequence BC-CB-BC. Only the three-layered rhombohedral phase is known for synthetic LDHs formed by coprecipitation from aqueous media.

2.1.1.2. Thermal Decomposition of Layered Double Hydroxide Precursor

The thermodynamically stable products of calcination of a $M^{II}M^{III}$-LDH in an inert gas are a spinel $M^{II}M^{III}{}_2O_4$ and free $M^{II}O$. At temperatures between initial LDH decomposition and spinel

phase formation, a series of metastable phases, both crystalline and amorphous, form.[58] The properties of these phases depend on the cations constituting the original LDH, preparation and thermal decomposition conditions, and the presence of impurities.[56]

The process of thermal decomposition of a carbonate LDH consists of dehydration, represented by the formula,

$$[M^{II}_{1-x}M^{III}_{x}(OH)_2]^{x+}[(x/2)CO_3^{2-}\cdot zH_2O] \rightarrow [M^{II}_{1-x}M^{III}_{x}(OH)_2]^{x+}[(x/2)CO_3^{2-}] + zH_2O \qquad \textbf{(2.1)}$$

followed by dehydroxylation and decarbonation, yielding a mixed oxide phase at temperatures less than 550 °C, given by

$$[M^{II}_{1-x}M^{III}_{x}(OH)_2]^{x+}[(x/2)CO_3^{2-}] \rightarrow M^{II}_{1-x}M^{III}_{x}O_{1+x/2} + x/2\,CO_2 + H_2O \qquad \textbf{(2.2)}$$

2.1.1.3. Reconstitution of Layered Double Hydroxides - "Memory Effect"

The term "memory effect" describes the capacity of samples prepared by thermal decomposition of LDH precursors containing a volatile anion such as carbonate, to reconstitute the original layered structure upon adsorption of various anions,[59] or simply upon exposure to air.[60] This process can be represented by the formula,

$$M^{II}_{1-x}M^{III}_{x}O_{1+x/2} + x/mB^{m-} + (1+x/2)\,H_2O \rightarrow [M^{II}_{1-x}M^{III}_{x}(OH)_2]^{x+}[x/mB^{m-}] + xOH^- \qquad \textbf{(2.3)}$$

The reconstitution behavior is governed by the electrostatic interaction between the positively charged host layer and the interlayer anions. Since the rehydrolysis process generates OH^- ions, the degree of uptake will be governed by the anion exchange equilibrium between B^{m-} and OH^- for the LDH. As suggested by the reconstitution reaction (2.3), the pH of the reacting solution should increase with the progress of the reaction.

This reconstitution process had been used as a method for altering the composition of a LDH. By thermally decomposing an easily synthesized carbonate form of LDH to a mixed oxide phase and then exposing the latter to an aqueous solution, a desirable anion, B^{m-}, could be intercalated. Using

this method, isopolyoxometalates such as $V_{10}O_{28}^{6-}$ and $Mo_7O_{24}^{6-}$ anions had been incorporated into a LDH structure upon reconstitution.[61-63] This technique had also been used to incorporate certain dicarboxylic acid dianions.[64] However, despite literature claims to the contrary,[63] the reconstitution reaction (2.3) is *not* general, but depends significantly on the composition of the metastable mixed oxide phase and the nature of the anion B^{m-}. The counter cation, C^{q+}, present from the salt from which B^{m-} is derived, can also be involved in the reaction of the metastable mixed oxide. Perturbing the metastable oxide by exposing it to an aqueous solution of specific B^{m-} and C^{q+} ions can lead to reactions producing new, highly crystalline phases. As an example thereof, the reaction between a Zn/Al mixed oxide and ammonium and molybdate ions that produced a layered ammonium zinc molybdate termed Zn-LTM is presented.

2.1.2. Experimental Synthesis

The overall synthesis route of the Zn-LTM can be represented as follows:

$$\text{Zn,Al salts} \xrightarrow{\text{Precipitation}} \text{Zn/Al-LDH} \xrightarrow{\text{Calcination}} \text{Zn/Al Mixed Oxide} \xrightarrow{\textit{Chimie Douce}\ \text{Reaction}} \text{Zn-LTM}$$

2.1.2.1. Preparation of the Metastable Mixed Oxide Precursor

The mixed oxide precursor for the synthesis of Zn-LTM was derived from $Zn_4Al_2(OH)_{12}CO_3 \cdot zH_2O$ LDH. The LDH was synthesized by coprecipitation at constant pH, under conditions of low supersaturation. The precursor was prepared by adding a solution of $Zn(NO_3)_2 \cdot 6H_2O$ and $Al(NO_3)_3 \cdot 9H_2O$ to a solution of KOH and K_2CO_3, at relative rates such that a constant pH of 9.0 was maintained. The temperature of precipitation was 55±2 °C. Following precipitation, the material was aged in the mother liquor overnight at 70 °C. The material was then filtered, washed, and dried at 110 °C and at atmospheric pressure. The X-ray diffraction pattern of this material, shown in Figure 2.2(a), has sharp and symmetrical peaks characteristic of a well-crystallized Zn/Al-LDH.[65] The X-ray diffraction analysis confirmed the absence of a secondary zincite (ZnO) phase. The single phase LDH was expected as x = Al/(Zn+Al) = 0.33 was in the range of 0.3 to 0.4 in which single phase Zn/Al LDHs form.[65] The pattern was indexed in rhombohedral symmetry on hexagonal axes with a = 3.06(5) Å and c = 22.65(5) Å, determined by a least squares method.

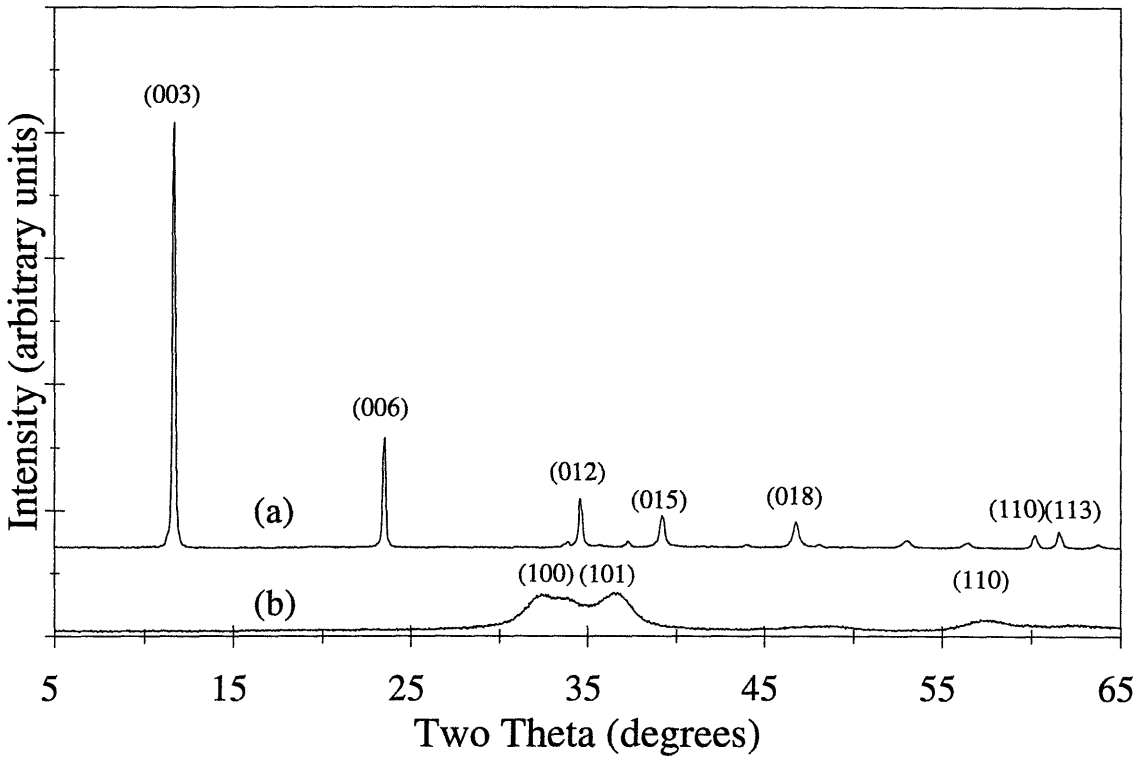

Figure 2.2. Powder X-ray diffraction pattern of a) $Zn_4Al_2(OH)_{12}CO_3 \cdot 4H_2O$, and b) the calcined LDH precursor.

Lattice parameter determination by least squares involves the minimization of the residual, R, given by

$$R = \sum_{i=1}^{n} \left(\sin^2\theta_o - \sin^2\theta_c \right)^2 \qquad \textbf{(2.4)}$$

where θ_o are the observed peak positions, and θ_c are the calculated peak positions determined by

$$\sin^2\theta_c = \lambda^2 \left(\frac{h^2 + k^2 + hk}{3a^2} + \frac{l^2}{4c^2} \right) \qquad \textbf{(2.5)}$$

for a hexagonal crystal system, where λ is the wavelength of the radiation used, and h, k and l are the Miller indices of the peak. Substituting Equation (2.5) into (2.4), the lattice parameters a and

c may be determined by solving the system of equations given by

$$\frac{\partial R}{\partial a} = 0; \qquad \frac{\partial R}{\partial c} = 0 \qquad \textbf{(2.6a and b)}$$

The Zn_4Al_2-LDH was calcined in air at 500 °C for 3.5 hours. The X-ray diffraction pattern of the calcined precursor is shown in Figure 2.2(b). The broad peaks are in similar positions to those of ZnO (zincite), which allowed for the indexing of the peaks on a hexagonal unit cell. A least-squares procedure was used to estimate the lattice constants from the (100), (101), (110) and (112) peak positions. The lattice constants of the calcined LDH (a = 3.21(3) Å, c = 5.12(3) Å) are smaller than those of pure ZnO (a = 3.24982(9) Å, and c = 5.20661(15) Å (PDF Card #36-1451)), which lead to the conclusion that the calcined LDH was a poorly crystalline Zn/Al solid solution conforming to the zincite lattice structure.

2.1.2.2. *Chimie Douce* Synthesis of Zn-LTM

The Zn-LTM phase was synthesized by adding the metastable mixed oxide to a solution of ammonium heptamolybdate (0.05 M $Mo_7O_{24}^{6-}$ and 0.3 M NH_4^+) at room temperature. Progress of the reaction was followed by monitoring the pH. A typical pH profile over the course of the reaction is shown in Figure 2.3. The pH profile indicates the complexity of the solution chemistry occurring during the *chimie douce* reaction. The variation in the pH reflects a complex competition between the generation and consumption of hydroxyl ions. Increases in pH result from the generation of hydroxyl ions by rehydrolysis of the zinc oxide and reaction of the hydrolyzed de-aluminated defect zinc oxide with molybdate anions. Hydroxyl ions are consumed by the reactions

$$Mo_7O_{24}^{6-} + 8\,OH^- \rightarrow 7\,MoO_4^{2-} + 4H_2O \qquad \textbf{(2.7)}$$

and

$$m\,Al^{3+} + n\,OH^- \rightleftharpoons Al_m(OH)_n^{(3m-n)+} \qquad \textbf{(2.8)}$$

leading to a lowering of the pH. The *chimie douce* reaction was deemed complete after observation of a constant pH. Following completion of the reaction, the product was recovered by filtration, washed with deionized water, and dried overnight at 110 °C. The product, called Zn-LTM, was a fine white powder.

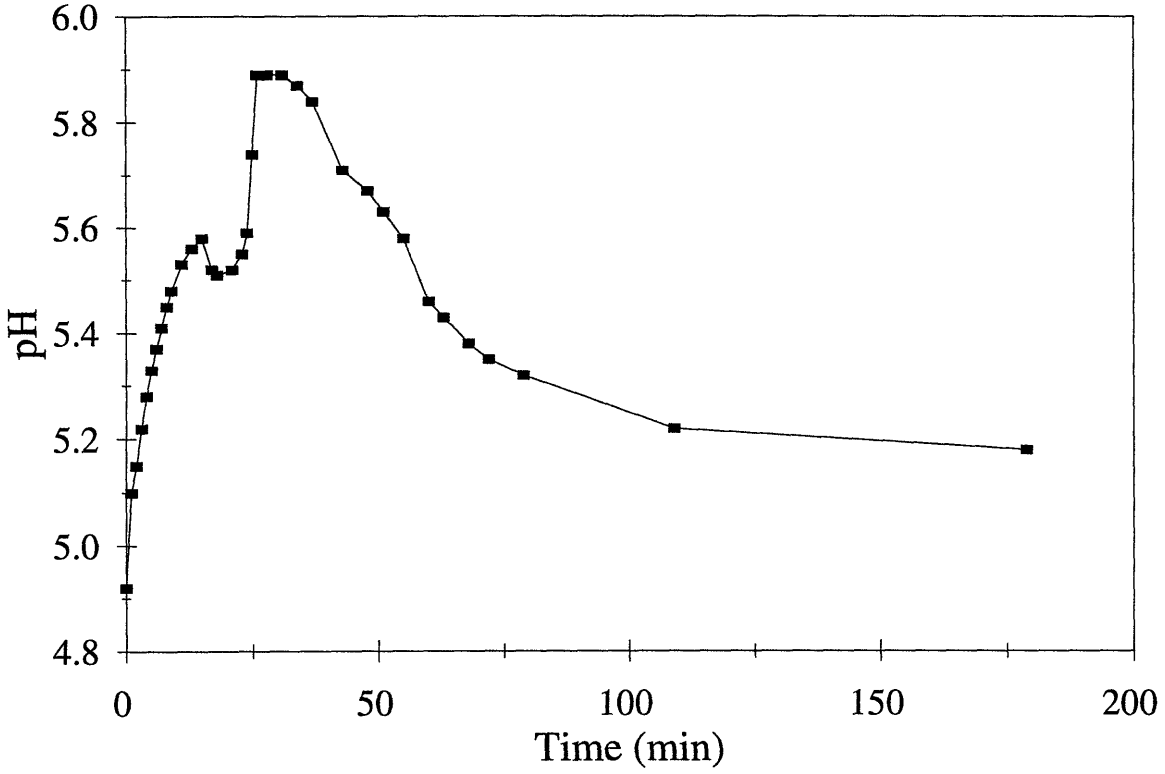

Figure 2.3. Change in pH during *chimie douce* reaction.

2.1.3. Characterization of Zn-LTM

Elemental Analysis

Elemental analysis of the LDH and the Zn-LTM was determined by X-ray fluorescence (Oneida Research Services, Whitesboro, New York). The Zn and Al content of the Zn_4Al_2-LDH was 41.2 and 8.02 wt.% respectively, giving a Zn/Al molar ratio of 2.1. Following *chimie douce* reaction with ammonium heptamolybdate solution, the Zn-LTM product analyzed as 33.8 wt.% Mo, 0.63 wt.% Al, and 24.6 wt.% Zn. The Zn/Mo and Zn/Al molar ratios in the product were therefore 1.07 and 16.1 respectively. There was thus an almost eight-fold increase in the Zn/Al ratio, resulting from Al leaving the solid on reaction with the ammonium heptamolybdate solution. The loss of Al from the structure led to the designation of this compound as Zn-LTM, as opposed to Zn-Al-LTM.

Infrared Spectroscopy

The photoacoustic Fourier-transform infrared (PA-FTIR) spectrum of the Zn-LTM is shown in Figure 2.4. This spectrum was collected with a 2.5 kHz rapid-scan at 8 cm^{-1} resolution, using a MTEC Model 200 Photoacoustic cell in a BioRad FTS-60A spectrometer. The PA-FTIR spectrum confirmed the presence of NH_4^+ ions in the structure, as evidenced by the ν_3 N-H asymmetric stretch in the region 3300-3050 cm^{-1} and the ν_4 H-N-H deformation at 1408 cm^{-1}.[66] The spectrum also shows the presence of an overtone at 2820 cm^{-1} ($2\nu_4$) and a combination band at 3040 cm^{-1} ($\nu_2+\nu_4$).[66] The broad band in the region 1600-2000 cm^{-1} arises from the interaction of ν_4 with the torsional oscillation ν_6 of the ammonium on its lattice site,[66] suggesting that the ammonium ion is not freely rotating. The PA-FTIR characterization proved that repeated washing of the material had failed to remove the ammonium ions, leading to the conclusion that the ammonium ions were a part of the crystal structure.

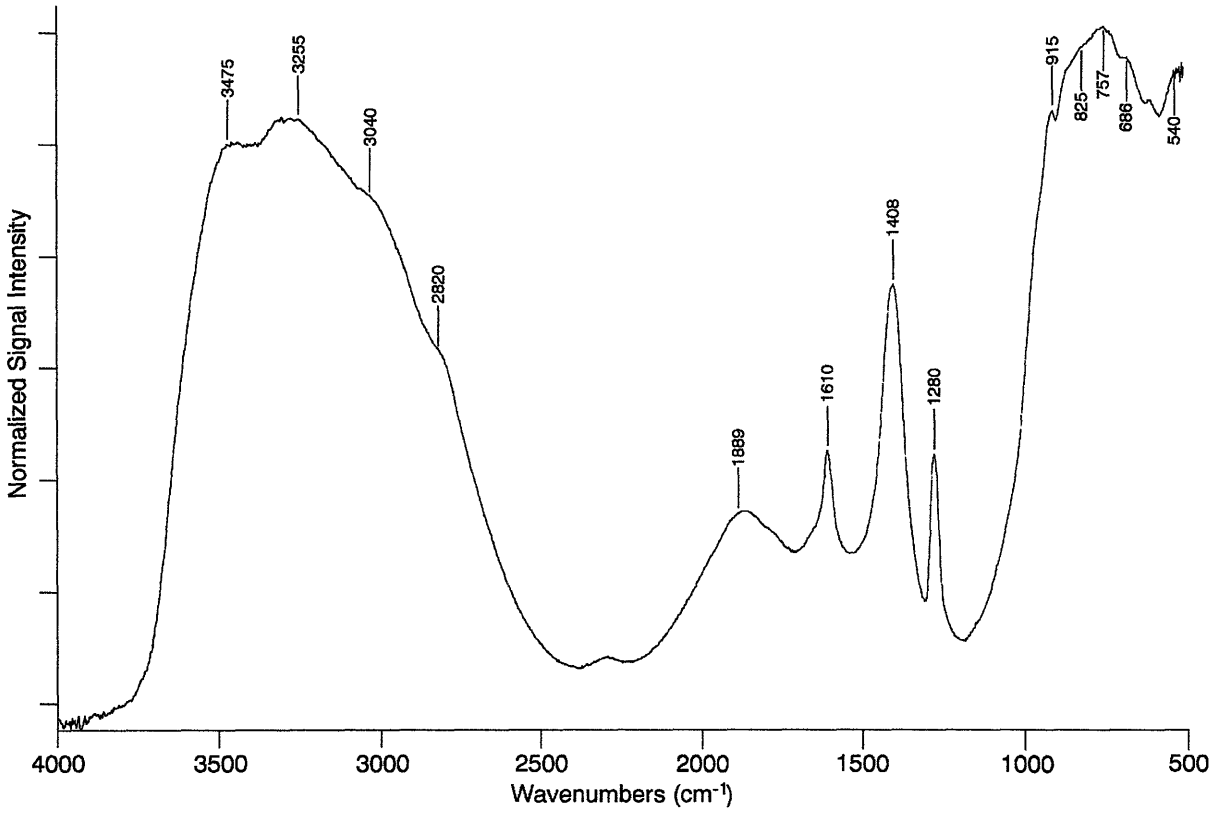

Figure 2.4. PA-FTIR spectrum of Zn-LTM

X-ray Diffraction

A powder X-ray diffraction pattern of this material, collected on a Siemens D5000 θ/θ diffractometer operated at 45 kV and 40 mA with CuKα radiation, is shown in Figure 2.5. A step-scanned diffraction pattern was collected from 10 to 90° 2θ (0.02° step, 2.5 sec/step, sum of 3 scans) for use in Rietveld refinement of the structure. This diffraction pattern is significantly different from ZnO and bears no resemblance to that expected from a LDH pillared with the heptamolybdate anion.[61,62]

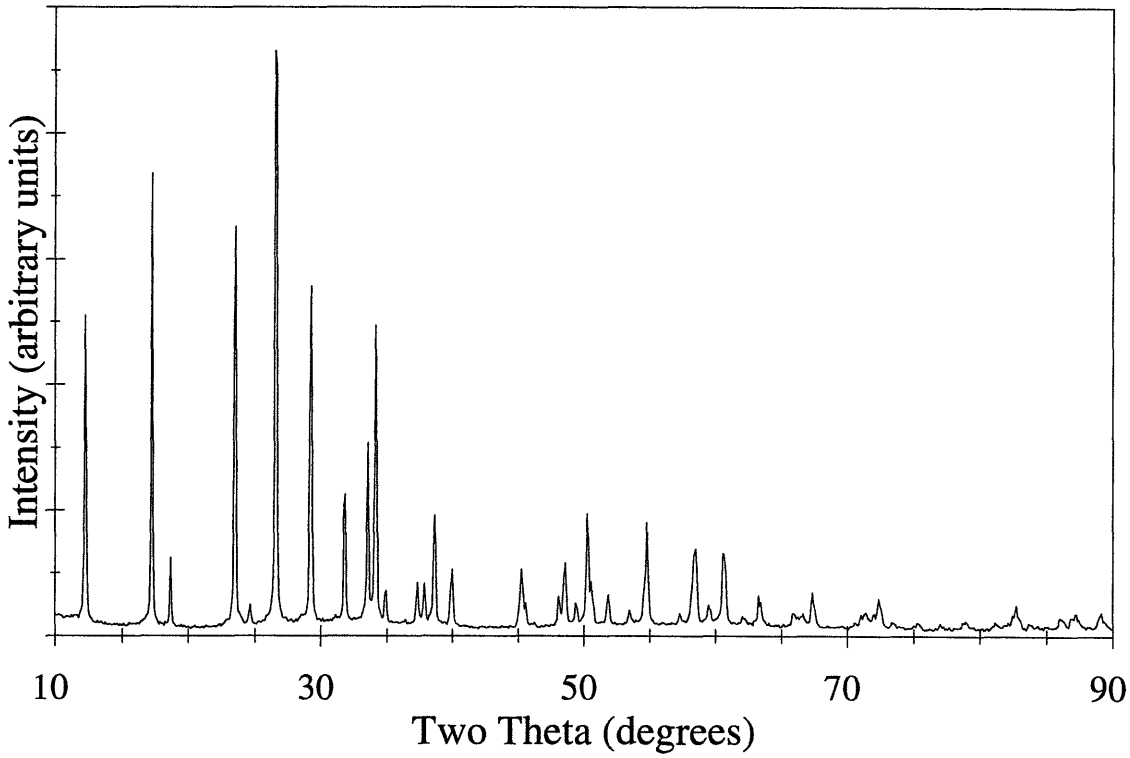

Figure 2.5. Powder X-ray diffraction pattern of Zn-LTM.

2.1.4. Generality of the *chimie douce* reaction for the synthesis of LTM materials

The *chimie douce* reaction with ammonium heptamolybdate solutions only occurred with mixed oxide phases derived from LDHs of the form $[Zn_{(1-x-y)}M^{II}_{y}Al_{x}(OH)_2]^{x+}[(CO_3)_{x/2}\cdot zH_2O]$, where M^{II} was Cu^{2+}, Co^{2+} and Ni^{2+}, and $(1-x-y)/x > 1$. No *chimie douce* reaction with ammonium

heptamolybdate solutions occurred for mixed oxide phases prepared from $[M^{II}_{(1-x)}Al_x(OH)_2]^{x+}[(CO_3)_{x/2}\cdot zH_2O]$ precursors, where $M^{II} = Mg^{2+}$ or Ni^{2+} (i.e. any M^{II} whose corresponding oxide, $M^{II}O$, is of the rock-salt structure). In the latter case, the heptamolybdate anion is pillared between the reconstituted LDH,[60,61] without forming the LTM crystalline phase.

To investigate the reason for the reactivity of the aluminum-substituted oxide phases, samples of $Zn_4Al_2(OH)_{12}CO_3\cdot zH_2O$ and $Mg_4Al_2(OH)_{12}CO_3\cdot zH_2O$ were calcined at 500 °C for 3.5 hours in air, allowed to cool in a desiccator, and then examined by ^{27}Al Magic Angle Spinning Nuclear Magnetic Resonance (MAS NMR) spectroscopy. Solid state aluminum NMR spectra were acquired at room temperature with Magic Angle Spinning on a Chemagnetics CMX-500 operating at 130.27 MHz. Samples were typically spun at frequencies of 6 kHz and the spectra were referenced to aqueous solutions of aluminum sulfate (resonance frequency = 0 ppm). The NMR spectra of the Al-substituted ZnO phase and the Al-substituted MgO phase are shown in Figures 2.6 (a) and (b) respectively. The peak around 0 ppm is attributed to octahedrally coordinated aluminum, Al_O, and the peak around 65-70 ppm is attributed to tetrahedrally coordinated aluminum, Al_T.[67] Comparing integrated peak intensities, the Al_T/Al_O ratios were determined to be 5.25 for the calcined Zn_4Al_2-LDH and 0.75 for the calcined Mg_4Al_2-LDH. The result for the Al_T/Al_O ratio for the calcined Mg_4Al_2-LDH is in agreement with a value of 0.70 reported in the literature.[68] These results seem to indicate that a very high proportion of tetrahedrally coordinated Al is a requisite for the *chimie douce* reaction producing the LTM phase.

It is interesting to compare the fraction of tetrahedrally coordinated aluminum in the calcined Al-substituted ZnO phase to the Al content of Zn-LTM powder, as determined by chemical analysis. Using integrated peaks intensities of the NMR data shown in Figure 2.6 (a), the percentage of tetrahedrally coordinated aluminum was found to be 84%. If, assuming that all tetrahedrally coordinated aluminum and none of the octahedrally coordinated aluminum enter into solution on *chimie douce* reaction, there will be a reduction in the cation content from a Zn_4Al_2 precursor to a $Zn_4Al_{0.32}$ product, resulting in a Zn/Al ratio of 12.5. The Zn/Al ratio determined by chemical analysis was 16.1. Since accurate determination of a true Al_T percentage in the sample is complicated by asymmetric line broadening from secondary quadrupolar effects, there is sufficiently reasonable agreement between the NMR and chemical analyses to suggest that the *chimie douce* reaction proceeds via loss of tetrahedrally coordinated aluminum from the metastable mixed oxide phase.

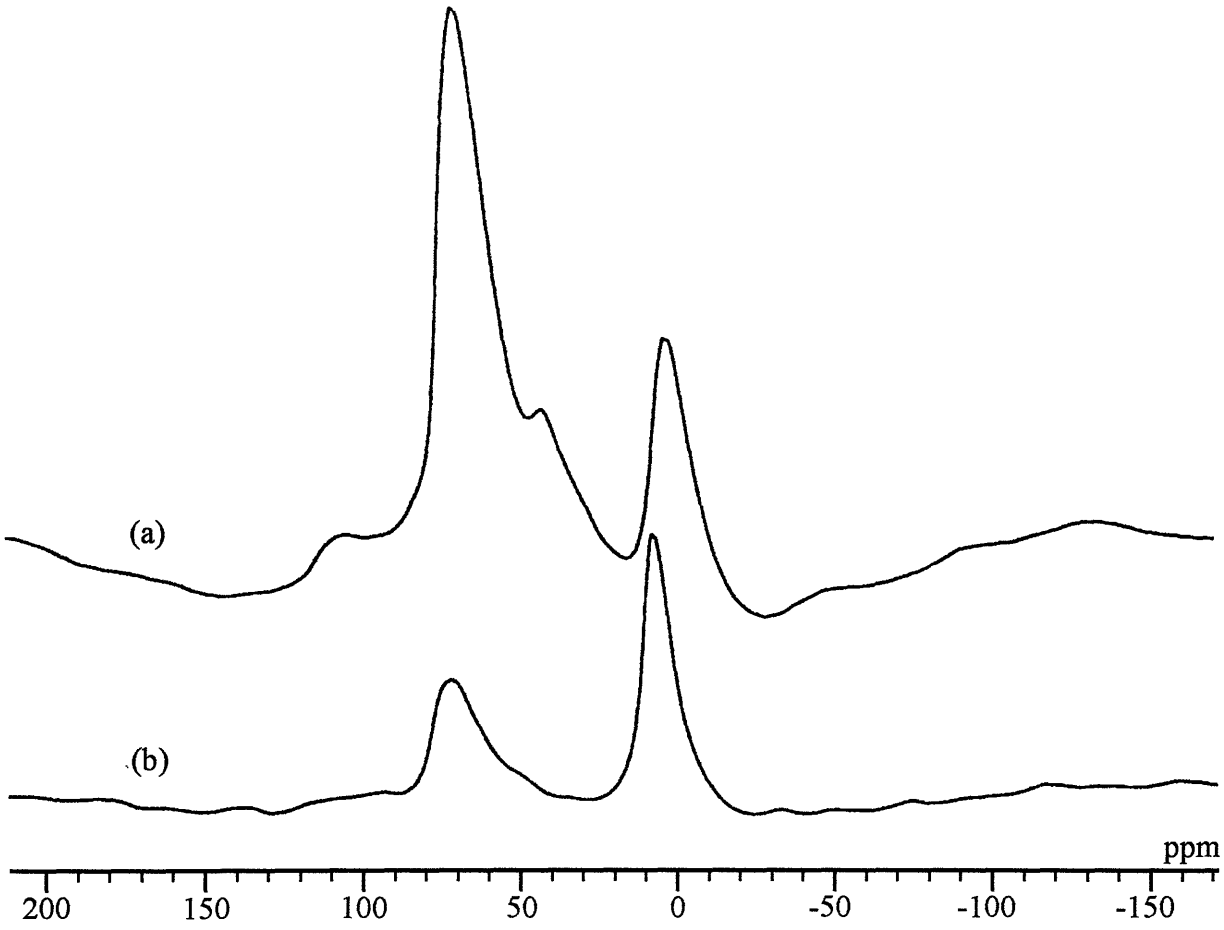

Figure 2.6. ^{27}Al NMR spectra of a) calcined $Zn_4Al_2(OH)_{12}CO_3 \cdot 4H_2O$ and b) calcined $Mg_4Al_2(OH)_{12}CO_3 \cdot 4H_2O$.

2.2. Synthesis of a Layered Ammonium Nickel Molybdate by Chemical Precipitation

2.2.1. Introduction

The success of the *chimie douce* synthesis route is dependent on certain properties of the metastable mixed oxide phase prepared by mild calcination of a LDH precursor. These properties include having a large percentage of tetrahedrally coordinated aluminum, a property typically satisfied by mixed oxide phase having a wurtzite structure. No *chimie douce* reaction with ammonium heptamolybdate solutions has been found to occur for mixed oxide phases prepared from LDH precursors whose corresponding oxide is of the rock-salt structure. This limitation in the synthesis route can, however, be overcome by using chemical precipitation to prepare other members

of the class of LTM materials.

2.2.2. Experimental Synthesis

An ammonium nickel molybdate was prepared by chemical precipitation, following a method described by Astier.[69] Ammonium heptamolybdate ($(NH_4)_6Mo_7O_{24}\cdot 4H_2O$) and nickel nitrate ($Ni(NO_3)_2\cdot 6H_2O$) were used to prepare a solution containing 0.10 mole Mo and 0.10 mole Ni. The initial pH of this green solution was 4.6. The addition of concentrated ammonium hydroxide (28.8% NH_3) precipitated a green solid that dissolved in an excess of ammonia giving a deep blue solution of pH 8.6. This solution was heated with constant stirring for four hours, leading to the formation of a pale green precipitate. The pH of the solution just prior to the recovery of the product was 5.6. The product was isolated by vacuum filtration, washed with deionized water, and dried overnight at 110 °C and atmospheric pressure. The product was a fine green powder.

2.2.3. Characterization

Synchrotron X-ray Diffraction

A powder X-ray diffraction pattern, collected on the X-10B beamline at Brookhaven National Laboratory's National Synchrotron Light Source, is shown in Figure 2.7. A Ge(220) monochromator and Ge(111) analyzer were used[70] and the wavelength was determined to be 1.1278 Å. The direct beam FWHM was equal to 0.0085 degrees and the beam intensity was 1.5E10 photons/sec. A flat tray sample holder was used. Data were collected in the range 5-62° 2θ with a step size of 0.015°.

Using the monoclinic cell of Astier,[69] the pattern was indexed and lattice constants were refined by least squares. Investigation of the relationships between the lattice constants showed that $a \cong b\sqrt{3}$ and $\cos\beta \cong -a/3c$. These relationships suggested that a higher degree of symmetry was present and the pattern was indexed using a rhombohedral cell on hexagonal axes. The indexed reflections showed systematic absences consistent with the space group $R\bar{3}m$ (No. 166). This symmetry is identical to that of the rhombohedral layered double hydroxide (LDH) precursor used in the *chimie douce* synthesis of the isostructural ammonium zinc molybdate.

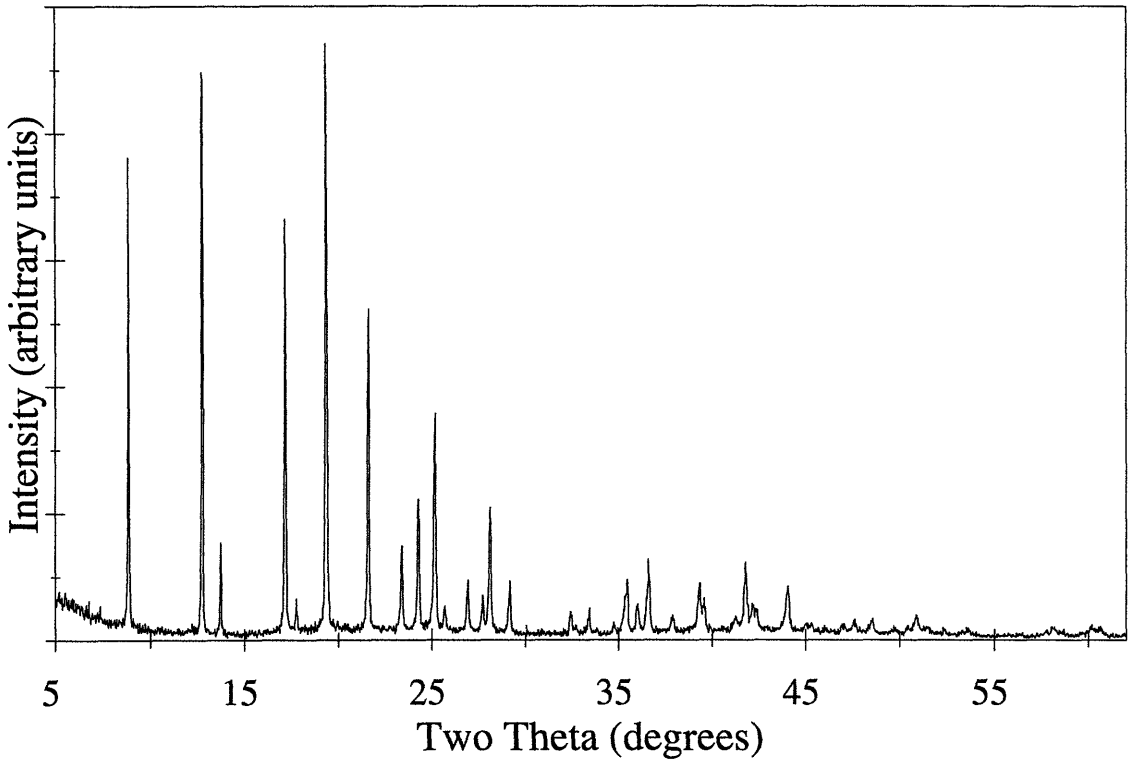

Figure 2.7. Powder X-ray diffraction pattern of Ni-LTM.

Elemental Analysis

The nickel and molybdenum content of the powder was determined using X-ray fluorescence (Oneida Research Services, Whitesboro, New York). The metal ratio (Ni/Mo) in the solid, 0.99, agreed well with the Ni/Mo ratio in the starting solution.

Infrared Spectroscopy

The photoacoustic Fourier-transform infrared (PA-FTIR) spectrum of the precipitate is shown in Figure 2.8. This spectrum was collected with a 2.5 kHz rapid-scan at 8 cm^{-1} resolution, using a MTEC Model 200 Photoacoustic cell on a BioRad FTS-60A spectrometer. This spectrum confirmed the presence of NH_4^+ ions in the structure, as evidenced by the ν_3 N-H asymmetric stretch in the region 3300-3050 cm^{-1} and the ν_4 H-N-H deformation at 1410 cm^{-1}.[66] The spectrum also shows the presence of an overtone at 2823 cm^{-1} ($2\nu_4$) and a combination band at 3028 cm^{-1} ($\nu_2+\nu_4$).[66] The broad

band in the region 1600-2000 cm^{-1} arises from the interaction of ν_4 with the torsional oscillation ν_6 of the ammonium on its lattice site,[66] suggesting that the ammonium ion is not freely rotating. The PA-FTIR characterization proved that repeated washing of the material could not remove the ammonium ions, leading to the conclusion that the ammonium ions were a part of the crystal structure.

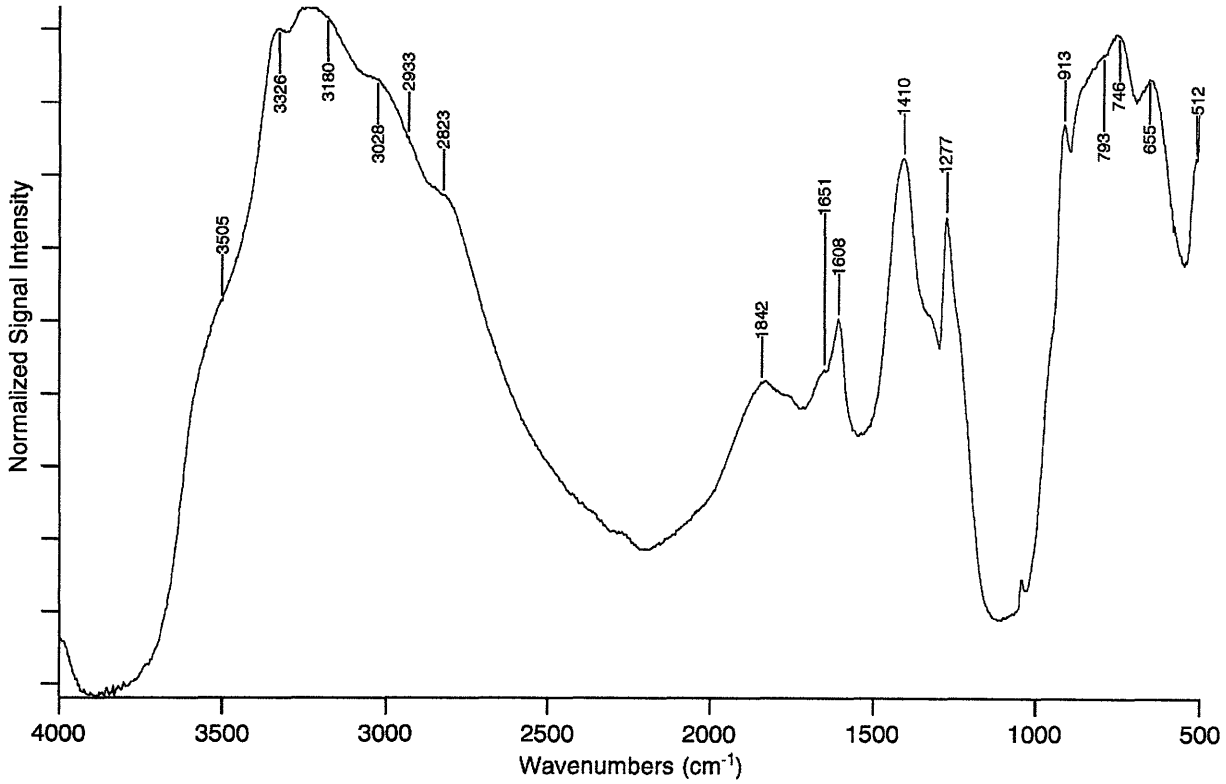

Figure 2.8. PA-FTIR spectrum of Ni-LTM.

Raman Spectroscopy

The Raman spectrum of the precipitate, collected with a BioRad FT-Raman spectrometer, is shown in Figure 2.9. The excitation source was a Nd-YAG laser operated at 1064 nm with input power of 60 mW. The signal was detected with a liquid nitrogen-cooled Ge detector. The Raman spectrum is relatively simple and confirmed the tetrahedral coordination of the molybdate anion. The two strong bands at 904 cm^{-1} and 321 cm^{-1} were assigned to a ν_1 symmetric stretch and a ν_2

symmetric bend, respectively.[71] The presence of only one symmetric stretch suggested that the molybdenum was occupying a single crystallographic tetrahedral site.

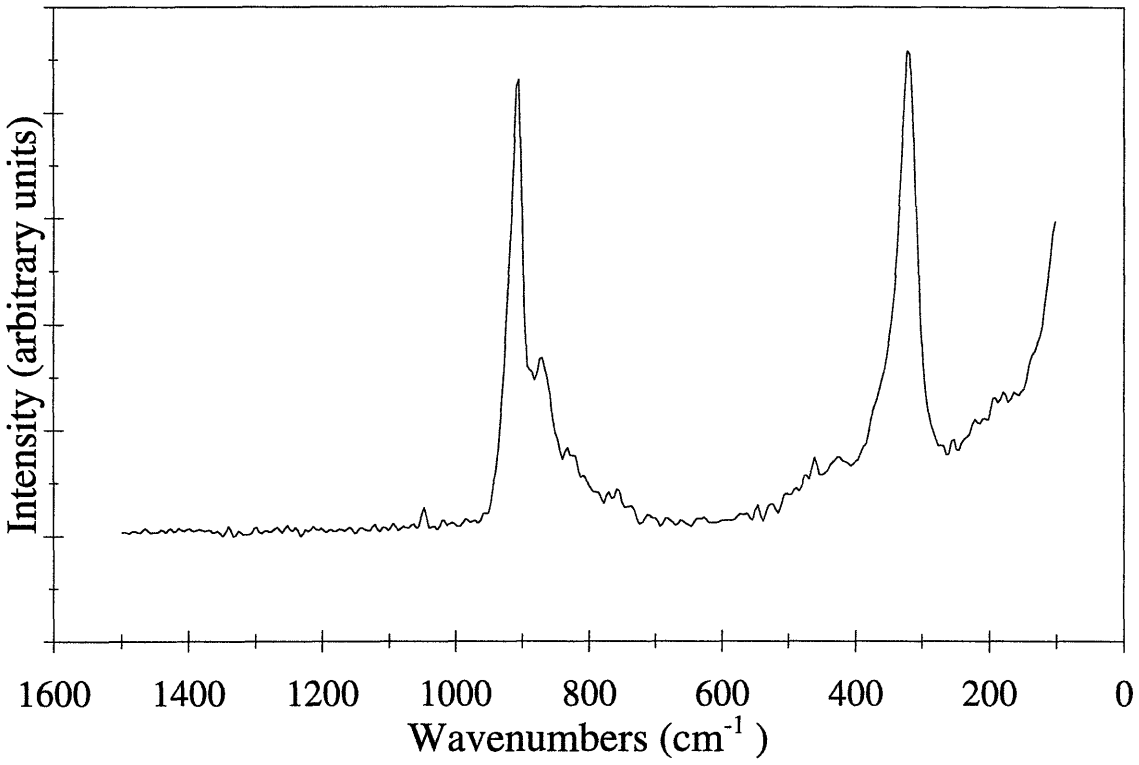

Figure 2.9. FT-Raman spectrum of Ni-LTM.

3. CRYSTAL STRUCTURE DETERMINATION OF LAYERED TRANSITION METAL MOLYBDATES

3.1. Introduction

The investigation into the crystal structure of this family of layered transition metal molybdates resulted from an exploration of the reactivity of metastable mixed oxide phases. From this work, a novel room-temperature *chimie douce* synthesis technique leading to the preparation of a layered ammonium zinc molybdate was discovered. In this *chimie douce* reaction, a metastable aluminum-substituted zincite phase, prepared by calcination of Zn/Al layered double hydroxide ($Zn_4Al_2(OH)_{12}CO_3 \cdot 4H_2O$), was reacted with a solution of ammonium heptamolybdate at room temperature to produce a highly crystalline compound termed Zn-LTM. The desire to solve the structure of this unknown material led to the search for a suitable isostructural compound. A search of the JCPDS database identified an isostructural phase (PDF card #40-674) reported by Astier,[69] a precipitated powder belonging to a family of ammonium-divalent cation-molybdenum oxides. As an example of this phase, an ammonium nickel molybdate compound had been prepared by direct precipitation from a solution of nickel nitrate and ammonium heptamolybdate, a route that did not involve LDH precursors. The X-ray diffraction patterns of Zn-LTM and this ammonium nickel molybdate (Figure 3.1 (a) and (b), respectively) clearly show that the two phases are isostructural. No detailed structural data were, however, known for this ammonium nickel molybdate. It was obvious, though, that knowledge of the structure of one would allow for rapid refinement of the other. The *ab initio* crystal structure determination of the ammonium nickel molybdate phase was therefore undertaken.

3.2. Crystal Structure Determination by Rietveld Refinement

The crystal structure of the Ni-LTM analog prepared by precipitation was solved first. The reason for choosing the nickel analog in preference to the Zn-LTM phase was the fact that the nickel analog only contained a single divalent cation (Ni), while the Zn-LTM phase seemed to contain both Al^{3+} and Zn^{2+}, in a ratio that differed significantly from the LDH precursor. The solution of the crystal structure of the precipitated Ni-LTM was, however, facilitated by the knowledge that an isostructural analog could be prepared from a LDH precursor. This had suggested $R\bar{3}m$ as the probable space group, in analogy to the rhombohedral LDH. In addition, the lattice parameters of

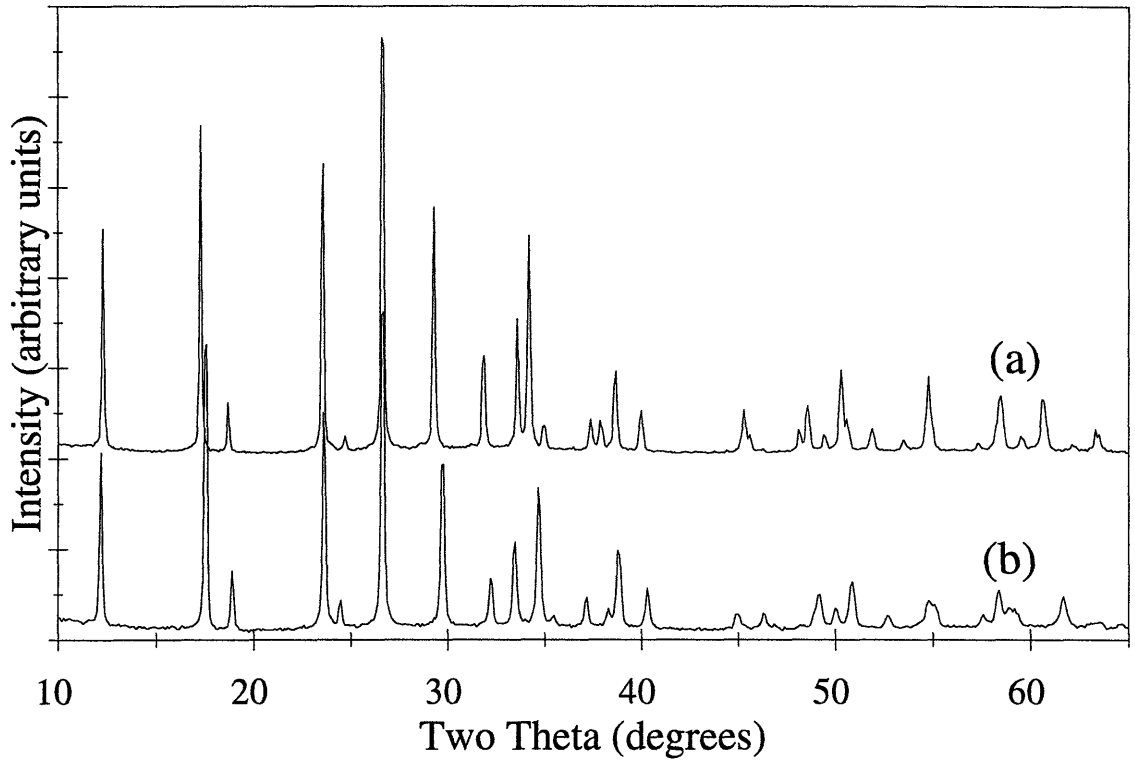

Figure 3.1. X-ray diffraction patterns of a) Zn-LTM, and b) $(NH_4)HNi_2(OH)_2(MoO_4)_2$, showing isostructural relationship.

the Zn-LTM seemed related to those of the LDH precursor. The XRD patterns of the Zn-LTM shown in Figure 2.6, and of the Zn-Al LDH shown in Figure 2.2(a), were indexed in a rhombohedral cell on hexagonal axes. For the Zn-LTM, $a \approx 2\ a_0$ and $c \approx c_0 - 1$ Å, where a_0 and c_0 are the lattice parameters of the original LDH, suggesting that the Zn-LTM could be a supercell of a modified LDH.

3.2.2. Solution and Refinement of the Ni-LTM Structure

A least squares refinement of the peak positions gave an initial hexagonal unit cell with parameters $a = 6.01$ Å and $c = 21.87$ Å. With this cell, the initial molybdenum and nickel atom positions were identified using three-dimensional Patterson methods. The oxygen and nitrogen atoms were then found using successive difference Fourier syntheses. The model was refined by the Rietveld method using the General Structure Analysis System (GSAS).[72] The refinement included

scale, background, lattice parameters, zero-point error, the Gaussian profile, the Lorentzian profile, asymmetry, anisotropic peak broadening, atom positions, nickel site occupancy, and thermal parameters. Isotropic temperature parameters were used for oxygen and nitrogen and anisotropic temperature parameters for molybdenum and nickel. X-ray anomalous dispersion coefficients were calculated using FPRIME within GSAS.[72] No corrections were made for absorption or extinction.

The refinement converged with $\mathbf{R}_{wp}$ = 13.5%† and $\mathbf{R}_p$ = 10.4%‡. The data, fit and residuals are shown in Figure 3.2. The atomic positions and thermal parameters are listed in Table 3.1 and a summary of the refinement parameters in Table 3.2. The temperature factors listed in Table 3.1 are expressed as either U_{iso} or u_{ij}, where the thermal correction (T") to the structure factor is either

$$T'' = e^{-(8\pi^2 U_{iso} \sin^2\theta/\lambda^2)} \tag{3.1}$$

for isotropic thermal motion, or

$$T'' = e^{-[2\pi^2(u_{11}h^2a^{*2} + \ldots + 2u_{12}hka^*b^* + \ldots)]} \tag{3.2}$$

for anisotropic thermal motion. The main concern over the refined parameters resulted from the low value of the nickel occupancy. This value, 0.575(6), is a bit far from the theoretical value of 0.667. The most significant residual occurs for the (101) peak at 12.8° 2θ, probably due to preferred orientation causing the observed intensity to be significantly larger than the calculated intensity. In an attempt to reduce the residual of this peak, the refinement program reduced the nickel occupancy factor until further reductions were offset by increased residuals at other peaks. However, attempts to correct for preferred orientation using GSAS did not result in a significant improvement in the overall fit, or lead to a significant increase in the nickel occupancy.

---

† $R_{wp} = \sqrt{\frac{\sum w(I_o - I_c)^2}{\sum w I_o^2}}$ where w is a weight derived from an error propagation scheme and assumed to be uncorrelated, and I_o and I_c are the observed and calculated intensities, respectively.

‡ $R_p = \frac{\sum |I_o - I_c|}{\sum I_o}$

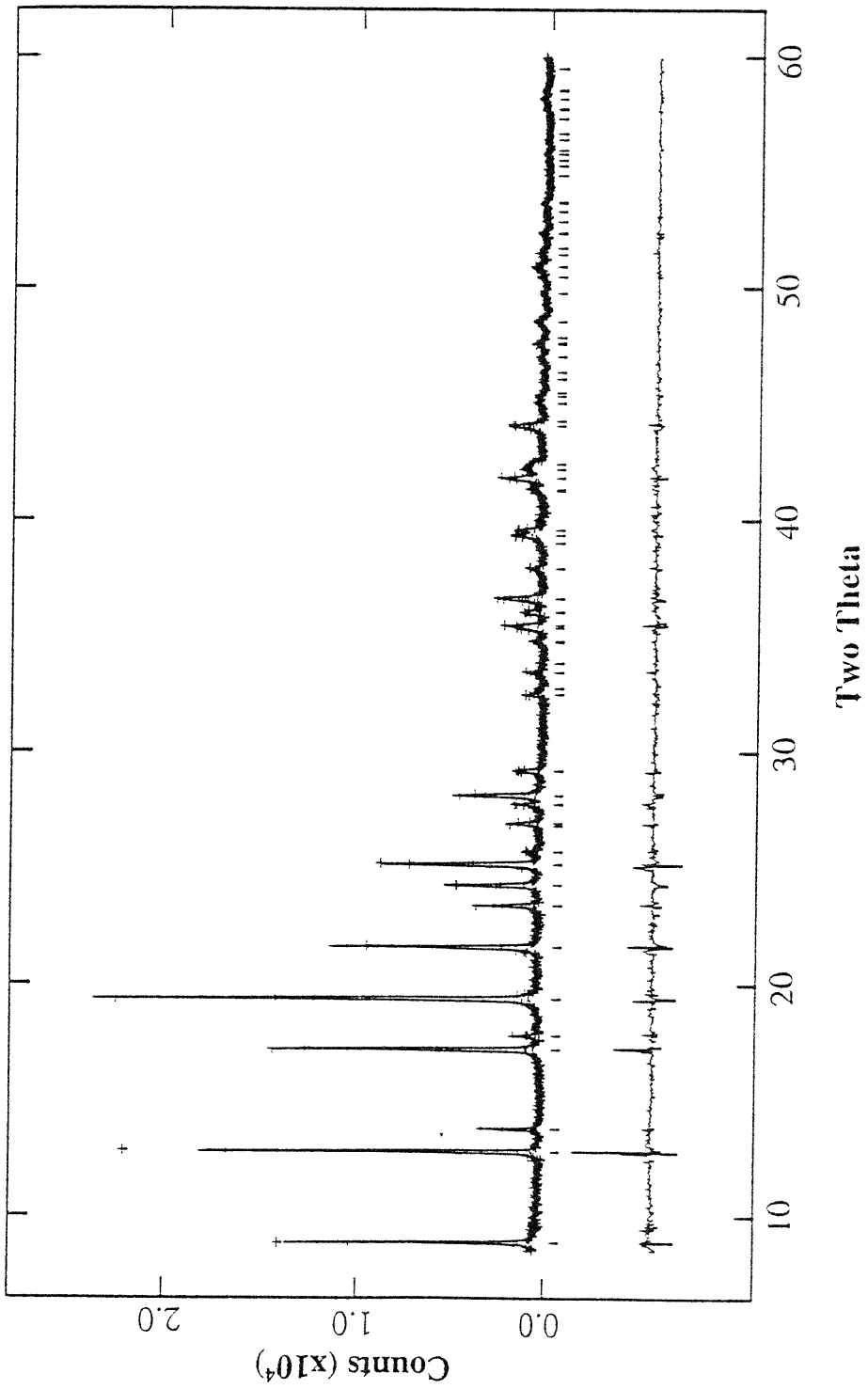

Figure 3.2. Synchrotron powder X-ray data, including Rietveld fit and residuals for $(NH_4)HNi_2(OH)_2(MoO_4)_2$. The set of short vertical bars below the data set indicates the position of possible Bragg reflections.

Table 3.1. Final Positional and Thermal Parameters for Ni-LTM

Atom	Wyckoff	x	y	z	U_{iso}*100	Fraction
Mo	6(c)	0	0	0.08850(10)	5.7†	1.0
Ni	9(e)	½	0	0	4.1‡	0.575(6)
O(1)	6(c)	0	0	0.2952(6)	6.8(5)	1.0
O(2)	6(c)	0	0	0.1636(7)	9.6(7)	1.0
O(3)	18(h)	0.3072(14)	0.1536(7)	-0.06067(29)	6.9(3)	1.0
N	3(b)	0	0	½	4.1(6)	1.0

† $(u_{11} = u_{22})*100 = 7.0(2)$, $u_{33}*100 = 3.1(2)$, $u_{12}*100 = 3.47(8)$, $u_{13} = u_{23} = 0$

‡ $u_{11}*100 = 3.8(3)$, $u_{22}*100 = 5.3(4)$, $u_{33}*100 = 3.2(3)$, $u_{12}*100 = 2.6(2)$, $u_{13}*100 = -0.09(14)$, $u_{23}*100 = -0.17(28)$

Table 3.2. Crystallographic data for $(NH_4)HNi_2(OH)_2(MoO_4)_2$ from Rietveld Refinement of powder X-ray diffraction data

Formula	$(NH_4)HNi_2(OH)_2(MoO_4)_2$
Formula weight (g/mol)	490.34
Space group	$R\bar{3}m$
a (Å)	6.0147(4)
c (Å)	21.8812(13)
V (Å^3)	685.53(7)
Z	3
D_{calc} (g/cm^3)	3.446
$\mathbf{R}_{wp}$	13.5%
$\mathbf{R}_p$	10.4%
$\mathbf{R}_{exp}$	2.2%

Consistency Check of Determined Structure

The bond-valence method[73-75] was used to check whether the determined Mo-O and Ni-O bond distances support a valence of +6 and +2 for the Mo and Ni respectively. The valence, V_i, of the metal atom was calculated from

$$V_i = \sum_j v_{ij} \tag{3.3}$$

where v_{ij} is the valence of a bond between two atoms i and j, and is empirically defined by

$$v_{ij} = \exp\left[\frac{(R_{ij} - d_{ij})}{0.37}\right] \tag{3.4}$$

where R_{ij} is the bond-valence parameter and d_{ij} is the bond length. For Mo^{VI}-O and Ni^{II}-O bonds, values of R = 1.907 Å and R = 1.654 Å respectively were used.[74] Using the values for d_{Ni-O} and d_{Mo-O} presented in Table 3.5, the valence of the molybdenum and nickel atoms were calculated as +7.06 and +1.77 respectively. These calculated values differ from the assumed valencies of +6 and +2 by +17.7% and -11.5% respectively. These error margins correspond to a combined error of about ±0.05 Å in R_{ij} and the bond length. As the reported accuracy of R_{ij} is ±0.02 Å,[74] the determined crystal structure is consistent.

3.2.3. Solution and Refinement of Zn-LTM Structure

Knowledge of the crystal structure of the ammonium nickel molybdate analog, $(NH_4)HNi_2(OH)_2(MoO_4)_2$, allowed for the rapid refinement of the structure of the Zn-LTM. Rietveld refinements were performed using General Structure Analysis System, GSAS,[72] using the structure of an isostructural nickel analog, $(NH_4)HNi_2(OH)_2(MoO_4)_2$, as a starting model. The refinement converged with $\mathbf{R}_{wp}$ = 9.8% and $\mathbf{R}_p$ = 7.9%. The data, fit and residuals are shown in Figure 3.3. The atomic positions and thermal parameters are listed Table 3.3 and the summary of the refinement in Table 3.4. The refinement included background, lattice parameters, the Gaussian profile, the Lorentzian profile, asymmetry, atom positions and thermal parameters. Isotropic temperature parameters were used for all atoms except molybdenum.

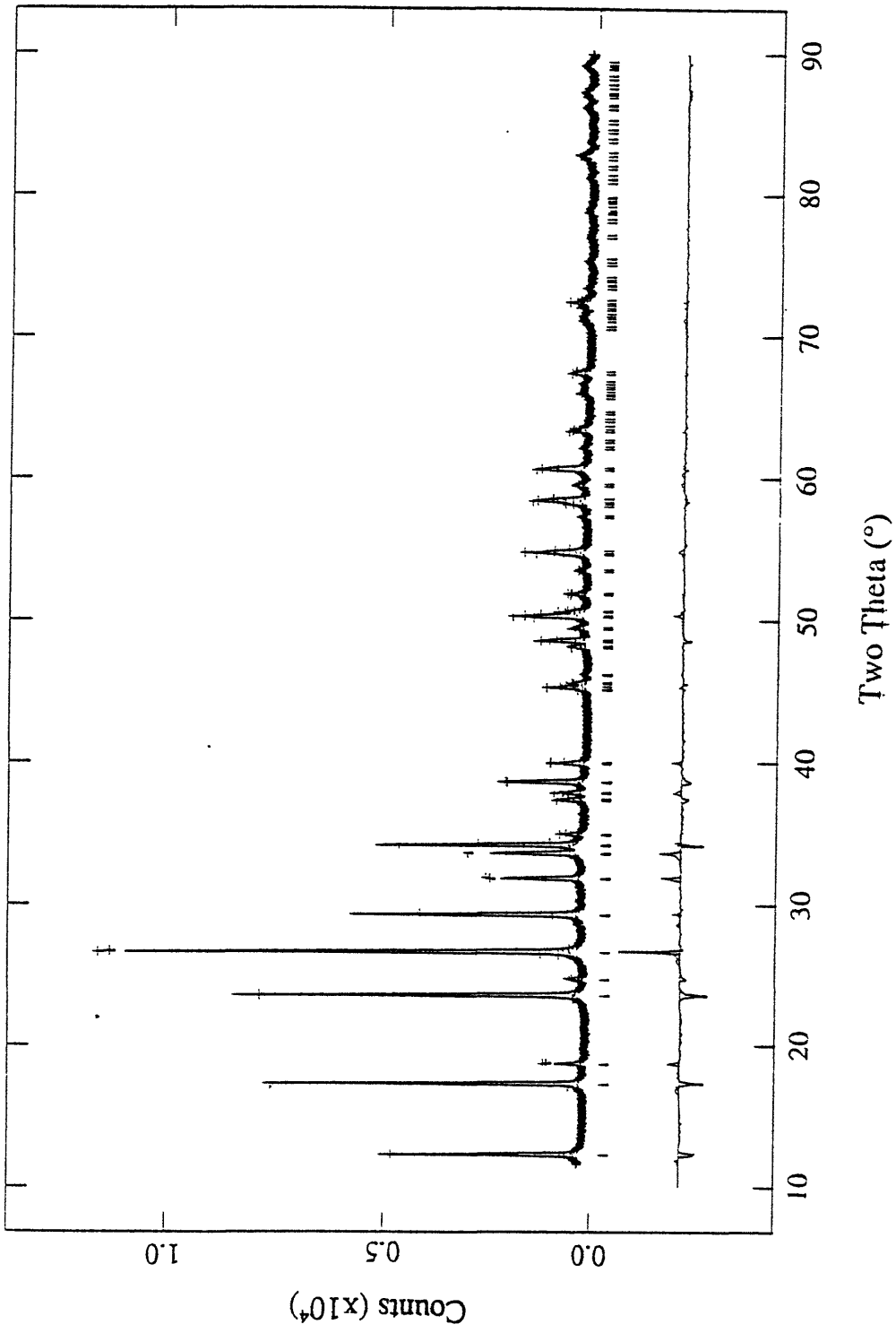

Figure 3.3. Powder X-ray data, including Rietveld fit and residuals for Zn-LTM. The set of short vertical bars below the data set indicates the position of possible Bragg reflections.

Table 3.3. Final Positional and Thermal Parameters for Zn-LTM

Atom	Wyckoff	x	y	z	U_{iso}*100	Fraction
Mo	6(c)	0	0	0.09229(8)	†	1.0
Zn	9(e)	½	0	0	2.06(13)	0.642(4)
O(1)	6(c)	0	0	0.2996(4)	1.83(32)	1.0
O(2)	6(c)	0	0	0.1719(6)	7.37(48)	1.0
O(3)	18(h)	0.3137(10)	0.1568(5)	-0.06476(24)	4.40(24)	1.0
N	3(b)	0	0	½	0.5(0)‡	1.0

† $(u_{11} = u_{22})*100 = 2.91(8)$, $u_{33}*100 = 0.76(8)$, $u_{12}*100 = 1.45(4)$, $u_{13} = u_{23} = 0$
‡ Not refined

Table 3.4. Crystallographic data for $(NH_4)HZn_2(OH)_2(MoO_4)_2$ from Rietveld Refinement of powder X-ray diffraction data

Formula	$(NH_4)HZn_2(OH)_2(MoO_4)_2$
Formula weight (g/mol)	498.9
Space group	$R\bar{3}m$
a (Å)	6.10767(15)
c (Å)	21.6409(6)
V (Å^3)	699.13(4)
Z	3
D_{calc} (g/cm^3)	3.56
Background: Cosine Fourier Series	12 terms
$\mathbf{R_{wp}}$	9.8 %
$\mathbf{R_p}$	7.9 %
$\mathbf{R_F}$	9.6 %
$\mathbf{R_{exp}}$	5.2 %

In an attempt to account for the small percentage of Al reported by chemical analysis, Al atoms were placed on the same 9(e) site as Zn. When the fractional occupancy for the Al was set on the basis of the elemental analysis, the thermal parameter for Al increased immediately to 0.400, the maximum that GSAS will allow, after a few cycles of refinement. Alternatively, when the thermal parameter of the Al was constrained to equal that of the Zn, and the fractional occupancy was allowed to vary, the occupancy refined to zero. This lead to the conclusion that the Al is not actually in the structure itself, but is probably present as a small amorphous phase. This assumption is supported by the relatively high number of terms (12) required to fit the background satisfactorily.

3.3. Description of LTM Crystal Structure

The crystal structure of the Ni-LTM will be discussed as being representative of the class of LTM materials. The structure of the Zn-LTM is identical to that of the Ni analog, with zinc replacing nickel in the discussion that follows.

3.3.1. General Structure

The framework of the ammonium nickel molybdate consists of sheets of distorted nickel octahedra to which tetrahedral molybdate groups are bonded. These layers are stacked in the *c* direction and are held together by hydrogen bonding. The nickel atoms defining these layers are located at site 9(e) which has variable occupancy ranging from ½ to 1. If the occupancy of this site is one, the arrangement of nickel atoms can be considered as a pattern of two alternating strings, one being Ni–Ni–Ni, the other being Ni–□–Ni, where □ represents an ordered cation vacancy. This ordered cation vacancy is independent of the nickel occupancy. As the nickel occupancy deviates from unity, additional disordered vacancies appear in both strings. For the compound studied, the Ni/Mo ratio is 1 and three of every nine nickel sites are vacant. The coordination of oxygens about the nickel atoms is distorted octahedral, with a tetragonal contraction along the C_4 axis running through O(1)–Ni–O(1). The bond distances and angles defining the distorted octahedra are shown in Tables 3.5 and 3.6. The nickel atoms are linked to each other through double oxygen bridges. Each nickel octahedron shares edges with a maximum of four adjacent octahedra, thereby creating the sheets of octahedra perpendicular to the *c* axis.

Table 3.5. Selected Interatomic Distances for $(NH_4)HA_2(OH)_2(MoO_4)_2$

Atom Pair	Distance (Å)	
	A = Ni	**A = Zn**
Bonded		
Mo-O(2)	1.643(14)	1.722(12)
Mo-O(3) (x3)	1.712(7)	1.763(5)
A-O(1) (x2)	1.926(5)	1.908(4)
A-O(3) (x4)	2.243(5)	2.295(5)
Non-bonded		
Mo-Mo (across layer)	3.873(13)	3.992(8)
A-A (between adjacent layers)	7.294(13)	7.213(6)
O(2)-O(1)	2.880(18)	2.746(6)
N-O(1)	4.486(13)	4.337(6)
N-O(2)	3.473(3)	3.528(6)
N-O(3)	2.981(6)	2.889(5)

Table 3.6. Selected Interatomic Angles

Atoms	Angle (°)	
	A = Ni	**A = Zn**
O(2)-Mo-O(3) (x3)	110.83(23)	109.75(18)
O(3)-Mo-O(3) (x3)	108.08(24)	109.19(18)
A-O(1)-A (x3)	102.7(4)	106.28(2)

The absence of a nickel atom at the origin generates ordered vacancies in the sheet. These ordered vacant octahedral sites are capped, both above and below, by tetrahedral molybdate groups. Disordered vacant octahedral sites resulting from a reduction in the nickel occupancy from unity are, however, not capped by tetrahedral molybdate groups. The molybdate tetrahedra above and

below an ordered vacancy are related to each other by an inversion center midway between them. The tetrahedra share three of their corners with the nickel-oxygen octahedra at O(3). Since there are four O(3) atoms in each octahedron, four octahedral corners are shared with four different molybdate tetrahedra. Each molybdate tetrahedron shares corners with six different nickel octahedra, generating the hexagonal arrangement shown in Figure 3.4.

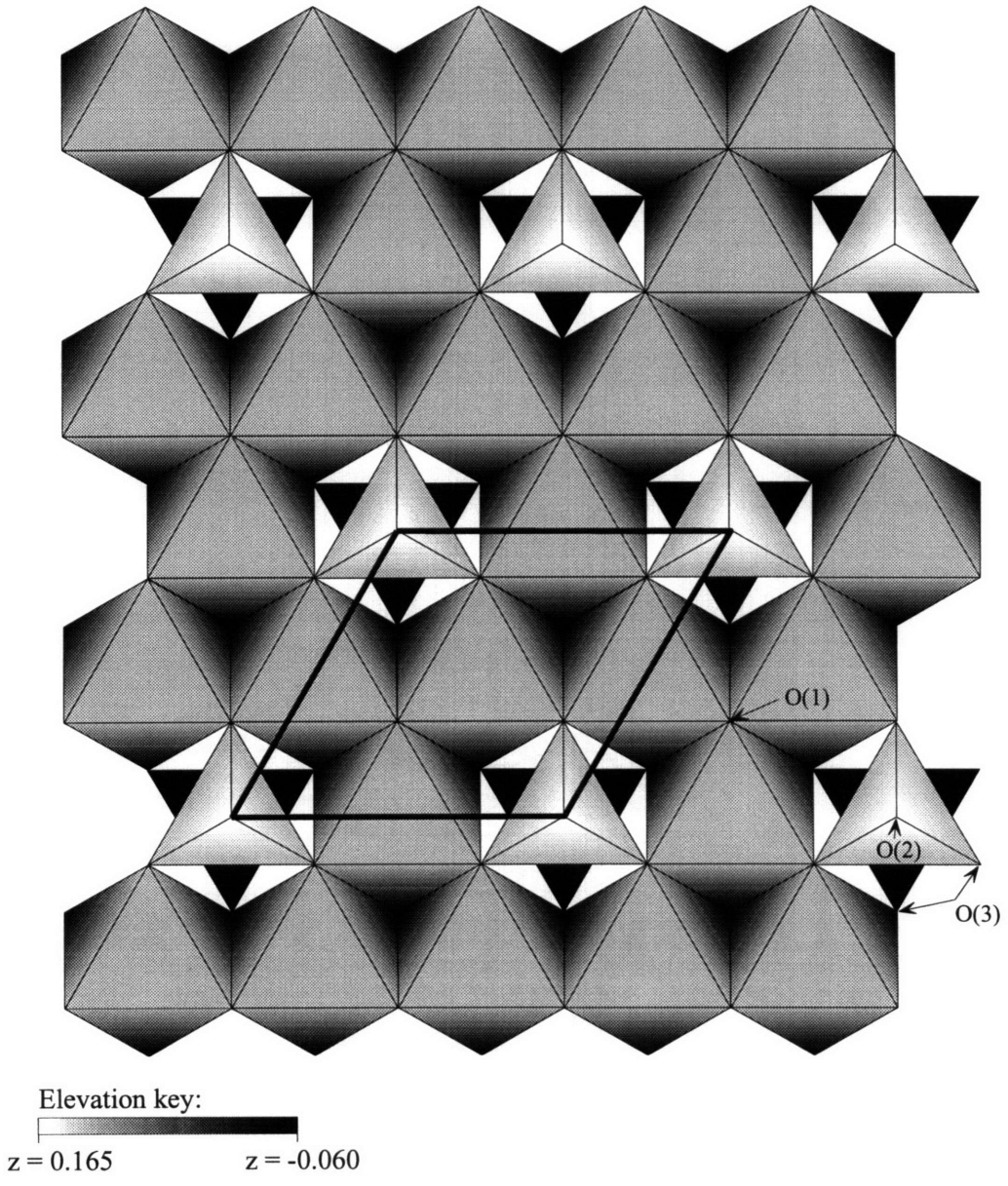

Figure 3.4. Basal plane of Ni-LTM, viewed along [001].

The three nickel molybdate layers defining the unit cell are stacked at a separation of $c/3$ = 7.2938(12) Å. In these layers, the position of the permanently vacant octahedral site capped by the molybdate groups follows the sequence A-B-C-A (where A, B, and C are the three threefold axes at x,y = 0,0; 2/3,1/3; and 1/3,2/3). This three-layer arrangement is shown in Figure 3.5. Between each layer, in the space defined by O(3) oxygens of six tetrahedral molybdates, lie ammonium ions. The positions of the nitrogen atoms follow the sequence C-A-B-C. The N-O(3) distance of 2.98 Å suggests that the ammonium ions are oriented with three of the four hydrogens directed towards O(3), thereby anchoring the ammonium ion via a hydrogen bonding mechanism. The arrangement of O(3) atoms is symmetrically equivalent above and below the nitrogen, suggesting that two orientations for the ammonium ions are possible. The ammonium ions can likely be found in either orientation with equal probability. The restriction on the orientation of the ammonium ions is supported by the infrared spectroscopic analysis that suggested that the ammonium ions are not freely rotating. The ammonium ions do not serve to connect the array of layers in the [001] direction, the N-O(1) distance of 4.49 Å being too long for hydrogen bonding. The vertical distance between O(2), the apical oxygen of the molybdate tetrahedra, and O(1), the bridging oxygen of the adjacent nickel layer, is 2.88 Å, suggesting that these two oxygens are involved in hydrogen bonding via hydroxyl protons that serves to connect the layers. Figure 3.6 illustrates a three-dimensional polyhedron representation of the crystal structure.

3.3.2. Assignment of Hydrogen Atoms

The non-hydrogen elements of the unit cell, as determined by elemental analysis and the refinement of the powder X-ray data, suggested an initial formula for this compound as "$(NH_4)_3Ni_6O_6(MoO_4)_6$." However, inspection of this formula shows that an additional 9 hydrogen atoms must be present to ensure charge balance. In the compound "$(NH_4)_3H_9Ni_6O_6(MoO_4)_6$" there are 21 hydrogen atoms to be placed in the unit cell, 9 of which are associated with the nickel-molybdenum-oxygen framework, the balance belonging to ammonium ions. The positions of the hydrogen atoms were tentatively determined by considering the crystal chemistry in regions of residual electron density (~ 1 $e^-/Å^2$) in the difference Fourier maps.

The positions of the hydrogen atoms of the ammonium groups (H(1) and H(2)) were determined by calculation using a N–H distance of 1.03 Å[76] and are shown in Table 3.7. It appears that two possible orientations of the ammonium ions are possible, as inferred from crystallographic

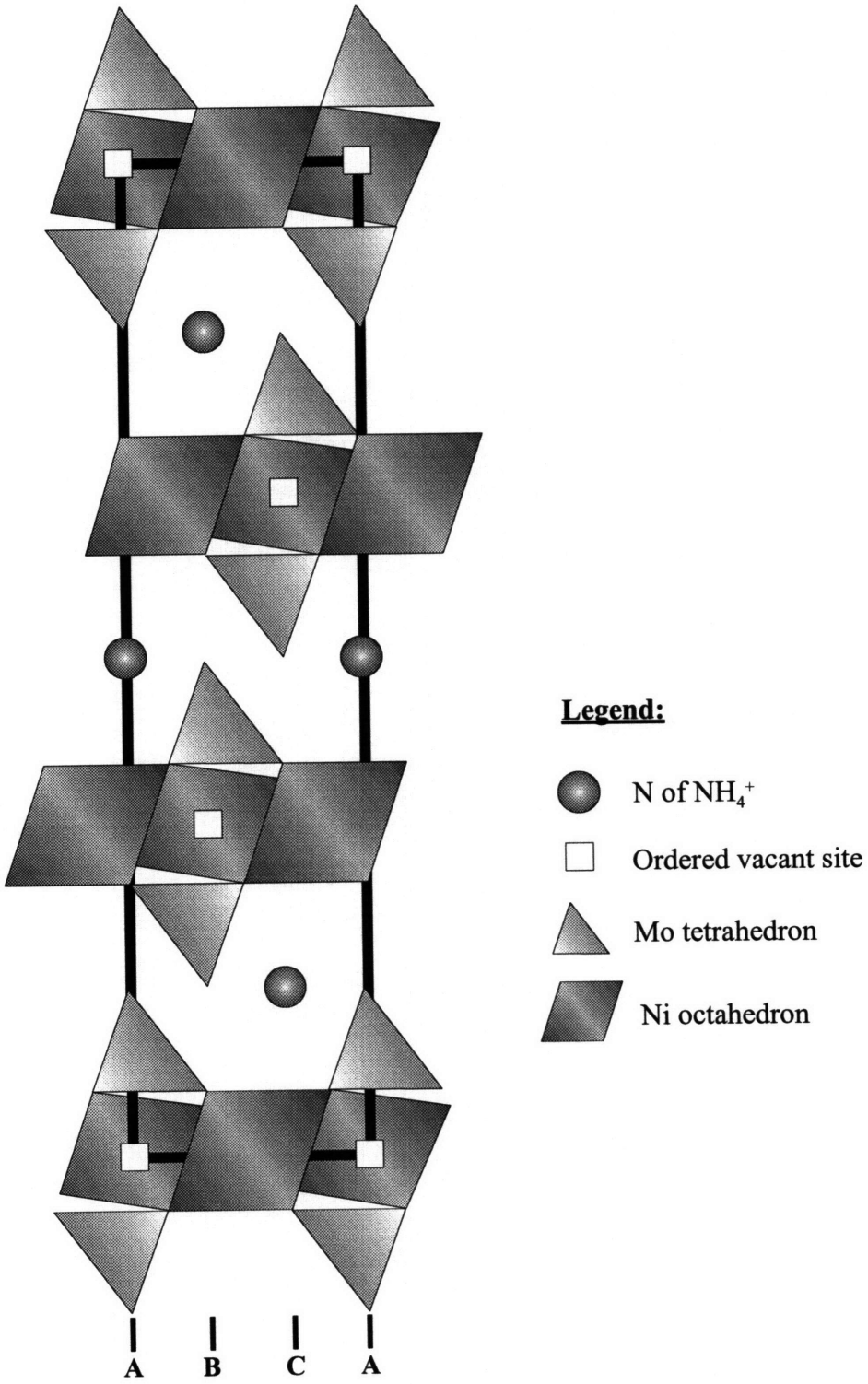

Figure 3.5. Crystal structure of Ni-LTM, viewed along [010], showing three-layer arrangement in polyhedron representation.

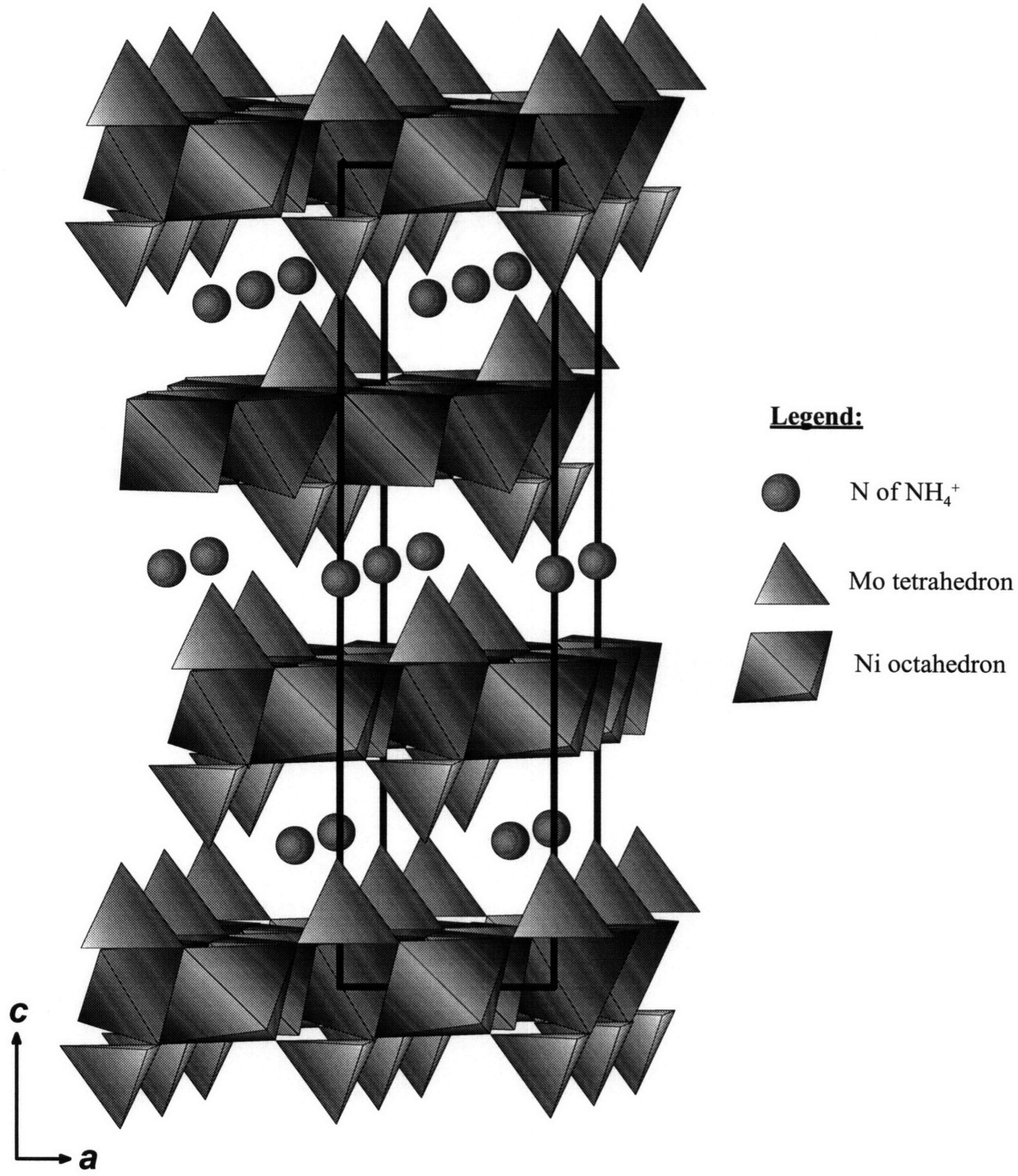

Figure 3.6. Crystal structure of Ni-LTM, viewed in polyhedron representation.

and PA-FTIR analysis. The coordination of O(3) oxygens around the nitrogen is octahedral with a N–O(3) distance of 2.98 Å. On the basis of the PA-FTIR analysis that showed the ammonium ions not rotating freely, it was surmised that the ammonium ions are tethered by hydrogen bonds between N–H and O(3). Consequently, the hydrogen atom H(2) was placed along the line joining N and O(3), at a distance of 1.03 Å from the nitrogen. Since the arrangement of O(3) atoms is symmetrically equivalent above and below the nitrogen atom, occupancies of ½ were assigned to H(1) and H(2) to account for the equal probability of finding the ammonium ion in either orientation.

Table 3.7. Calculated Hydrogen Positions

Atom	Wyckoff	x	y	z	Fraction
H(1)	6(c)	0	0	0.4529	½
H(2)	18(h)	0.2711	0.5422	0.1301	½
H(3)	6(c)	0	0	0.2506	1
H(4)	6(c)	0	0	0.3430	½

An additional 9 hydrogens needed to be assigned to the nickel-molybdenum-oxygen framework to ensure charge balance. The presence of a strong O–H stretching band in the PA-FTIR spectrum suggested that the bridging oxygen O(1) acts as a bridging hydroxyl. The O(1)–O(2) distance of 2.88 Å is also indicative of possible hydrogen bonding in the [001] direction that could serve to connect the layers. The hydrogen atom H(3) was therefore placed in a position such that the O(1)–H(3) distance is 0.97 Å.[77] The location of a hydrogen atom at this site with full occupancy (Table 3.7) accounts for 6 of the 9 hydrogens in the framework and makes all the bridging O(1) atoms bridging hydroxyls.

It is interesting to compare the difference Fourier maps before and after the placement of these hydrogens. A difference Fourier map of the partial (010) plane, calculated before the placement of the hydrogens, is shown in Figure 3.7. In addition to the residual density at the site of the heavy molybdenum atom, there are three crystallographically independent regions of positive electron density (~ 1 $e^-/Å^2$), designated in Figure 3.7 as ρ_1, ρ_2 and ρ_3. The region of electron density ρ_1 corresponds to the H(1) hydrogen of the ammonium group centered at 0 0 ½. The symmetry

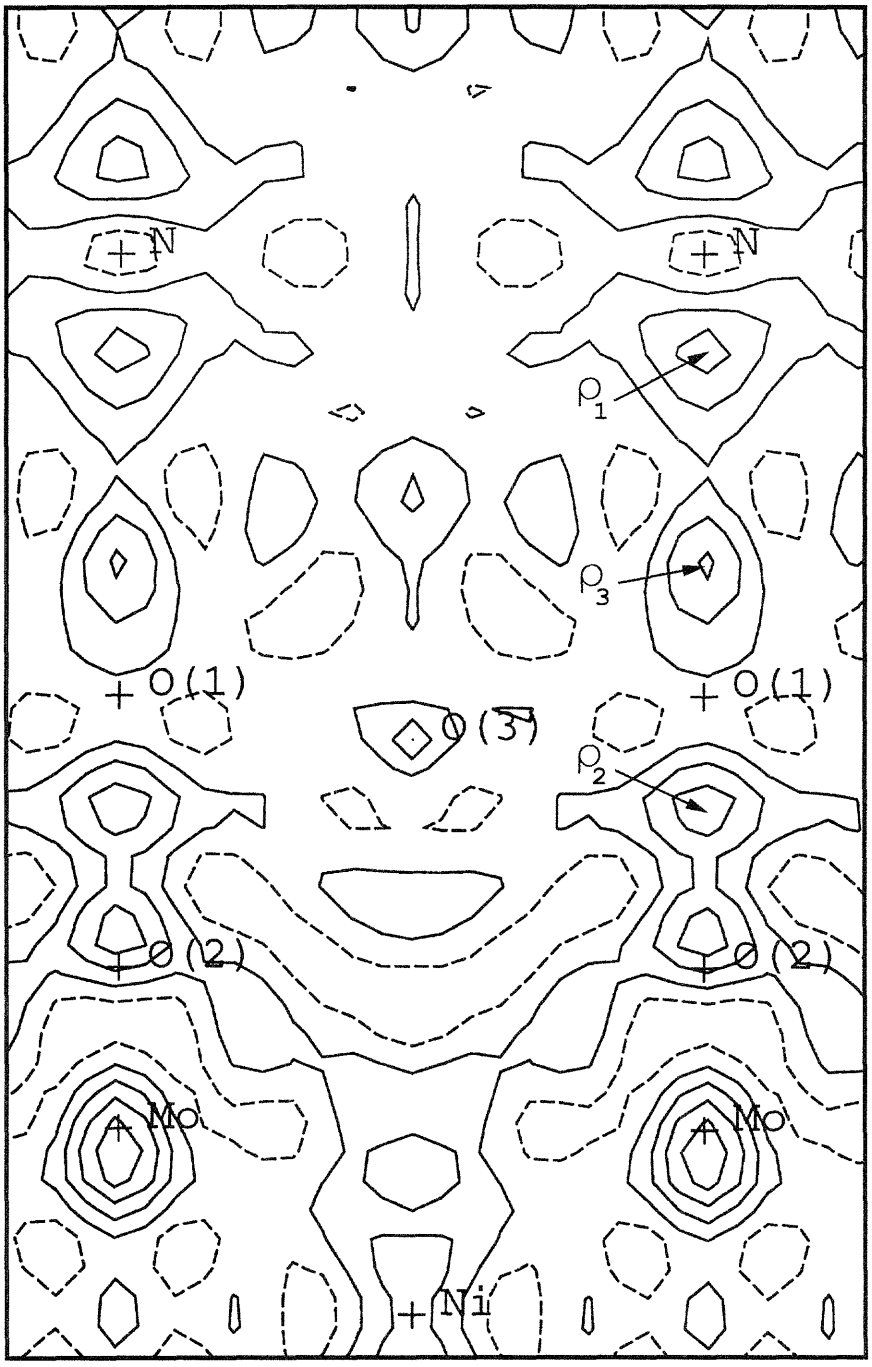

Figure 3.7. Difference Fourier map showing partial (010) plane. Successive contour lines differ by 0.3 $e^-/Å^2$. Dashed contours are negative.

equivalent position above the nitrogen is clearly visible in Figure 3.7. The other hydrogens (H(2)) forming the ammonium group are not in the plane shown in Figure 3.7.

The region of electron density ρ_2 corresponds to the H(3) hydrogen belonging to O(1). It was the presence of this residual electron density in the difference Fourier map that suggested that O(1) acts as bridging hydroxyl group for the hydrogen bonding between O(1) and O(2). An alternative location for the H(3) hydrogen, closer to O(2) along the line joining O(1) and O(2), would make the apical molybdate oxygen a hydroxyl, leading to the possible chemical formula $(NH_4)HNi_2O_2(MoO_3OH)_2$. There was, however, no experimental evidence to support this model which was therefore rejected. With the H(3)–O(1) distance set at 0.97 Å, the H(3)····O(2) distance of 1.90 Å is consistent with hydrogen bonding linking adjacent nickel molybdate layers through the interaction of the apical molybdate oxygen with the bridging hydroxyl.

An additional 3 hydrogens needed to be placed in the nickel-molybdenum-oxygen framework of the unit cell to ensure charge balance. The excellent correspondence between the observation of residual electron density at the sites calculated to contain hydrogens led to the speculation that the region ρ_3 could also be indicative of the location of hydrogens. This region of residual electron density ρ_3 corresponds to a tetrahedral site with point symmetry *3m* associated with the O(1) oxygen. This region of residual electron density was, therefore, tentatively assigned to a hydrogen, designated H(4), occupying this tetrahedral site. This arrangement is shown in Figure 3.8(a). An alternative location for these remaining hydrogens is shown in Figure 3.8(b). In this alternative model, half the bridging O(1) oxygens would be bridging waters and the remainder bridging hydroxyls, giving a possible chemical formula of $(NH_4)Ni_2OH(H_2O)(MoO_4)_2$. The presence of an H–O–H bending vibration band in the PA-FTIR spectrum cannot support the model shown in Figure 3.8(b) since the same band appears for the compound having full occupancy of the nickel site, i.e. $(NH_4)Ni_3O(OH)(MoO_4)_2$. (As indicated in section 3.4., a compound having full occupancy of the nickel site has only 3 framework hydrogens, making half the bridging oxygens hydroxyls). It is the presence of surface adsorbed water on the compound that gives rise to the H–O–H bending mode in the PA-FTIR spectrum. The assignment of hydrogens in the manner discussed above led to the chemical formula for this compound as $(NH_4)HNi_2(OH)_2(MoO_4)_2$.

Accurate refinement of these hydrogen positions is not possible with powder X-ray data. However, using the calculated hydrogen positions, a final difference Fourier map was calculated

using a default thermal parameter of 0.025 $Å^2$ for the hydrogen atoms and is shown in Figure 3.9. This figure illustrates that the remaining residual electron density greater than 0.5 $e^-/Å^2$ is associated with the heavy molybdenum atom.

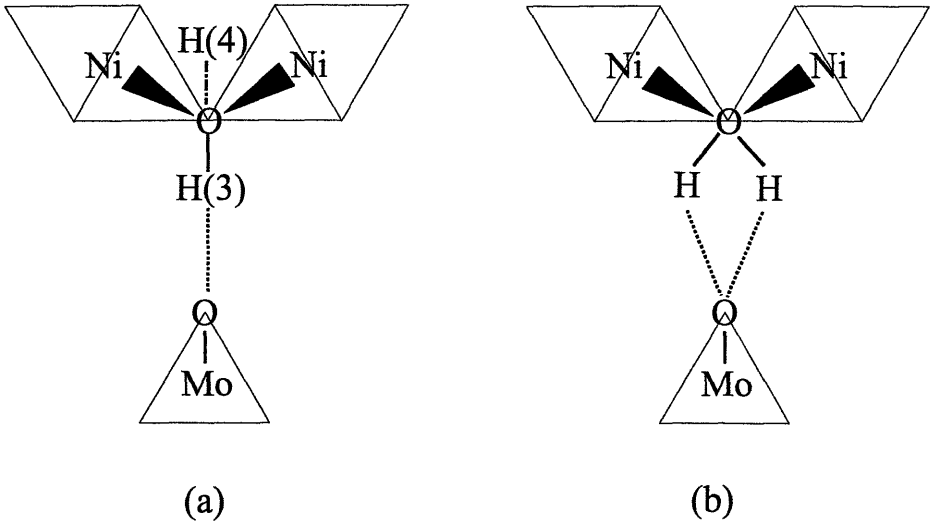

Figure 3.8. Possible locations for framework hydrogens: (a) in tetrahedral site associated with bridging hydroxyl; (b) as bridging water.

3.4. Solid Solution Series

Based on the structure of $(NH_4)HNi_2(OH)_2(MoO_4)_2$ as described above, it is proposed that this material is a member of a solid solution series of $(NH_4)H_{2x}Ni_{3-x}O(OH)(MoO_4)_2$, where $0 \leq x \leq 3/2$. The non-stoichiometry arises from variable occupancy of the nickel position. The nickel atom is situated at position 9(e) and I have proposed that the occupancy of this site can vary from ½ to 1. Since molybdenum sits at site 6(c) with full occupancy, the Ni/Mo ratio should theoretically be able to vary from 0.75 to 1.5.

The preparation of this compound with various Ni/Mo ratios has been carried out by Astier.[69] Even with solutions having atomic Ni/Mo ratios varying from 0.25 to 2.0, the final precipitated solids contained experimentally determined Ni/Mo ratios only between 0.8 and 1.6.[69] The structure now explains this composition range. The compounds having the general formula $(NH_4)H_{2x}Ni_{3-x}O(OH)(MoO_4)_2$ with $x = 0$, 0.5, 1 and 1.5 were chosen as examples to illustrate this solid solution series. All the necessary crystallographic variables are summarized in Table 3.8.

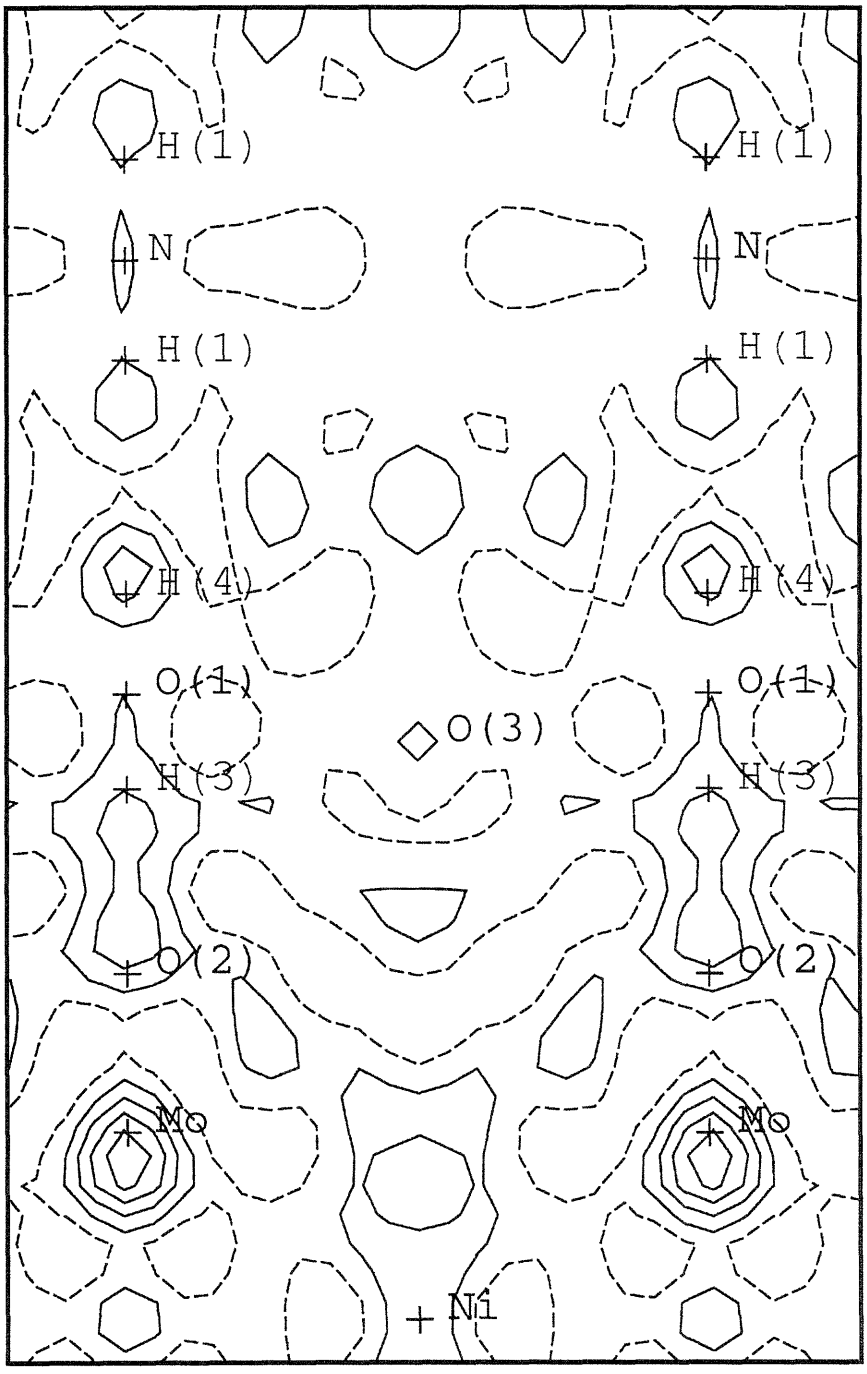

Figure 3.9. Difference Fourier map showing partial (010) plane. Successive contour lines differ by 0.3 $e^-/Å^2$. Dashed contours are negative. Difference Fourier map calculated for $\mathbf{R}_{wp}$ = 13.5%, $\mathbf{R}_p$ = 10.4%.

Table 3.8. Variables defining the compositions of structures having the general formula $(NH_4)H_{2x}Ni_{3-x}O(OH)(MoO_4)_2$

x	Ni/Mo ratio	Ni site occupancy	Fraction of O(1) as hydroxyl	Proton occupancy of T_2 site‡	Formula
0.0	1.5	1	½	0	$(NH_4)Ni_3O(OH)(MoO_4)_2$
0.5	1.25	5/6	1	0	$(NH_4)Ni_{2.5}(OH)_2(MoO_4)_2$
1.0	1.0	2/3	1	½	$(NH_4)HNi_2(OH)_2(MoO_4)_2$
1.5	0.75	½	1	1	$(NH_4)H_2Ni_{1.5}(OH)_2(MoO_4)_2$

‡ T_2 site = tetrahedral site having point symmetry *3m*

The upper limit to the Ni/Mo ratio is set by the maximum occupancy of the Ni site. The maximum Ni/Mo ratio occurs at full nickel occupancy, giving a Ni/Mo ratio of 1.5. In this compound, $(NH_4)Ni_3O(OH)(MoO_4)_2$, half the bridging O(1) atoms would be hydroxyls, the remainder being oxygen. In this compound, there are no additional associated H(4) hydrogens. As the occupancy of the nickel position decreases, the number of hydrogens should increase to maintain charge balance. The additional hydrogens initially convert the bridging O(1) oxygens into hydroxyls, such that at a nickel occupancy of 5/6, all the bridging O(1) oxygens are hydroxyls. Any further decrease in the nickel occupancy would then lead to the incorporation of associated H(4) hydrogens.

As shown in Figure 3.10, the two layers of four close-packed oxygens contained within the unit cell area generate 4 octahedral sites and 8 tetrahedral sites. The four octahedral sites are occupied by 3-*x* nickel atoms, one ordered vacancy (shown in Figure 3.10 as □), and *x* disordered vacancies. The eight tetrahedral sites consist of two groups, six sites having point symmetry *m* and designated T_1, and two sites having point symmetry *3m*, designated T_2. I am proposing that only the T_2 sites accommodate the associated hydrogens.

The structure determined in this study, $(NH_4)HNi_2(OH)_2(MoO_4)_2$, corresponds to the compound with $x = 1$. In this compound, the occupancy of the nickel site is 2/3, giving a Ni/Mo ratio of 1. To ensure charge balance, all the bridging O(1) atoms are hydroxyls and half the T_2 sites contain associated hydrogens. The minimum Ni/Mo ratio occurs at a nickel occupancy of ½, giving

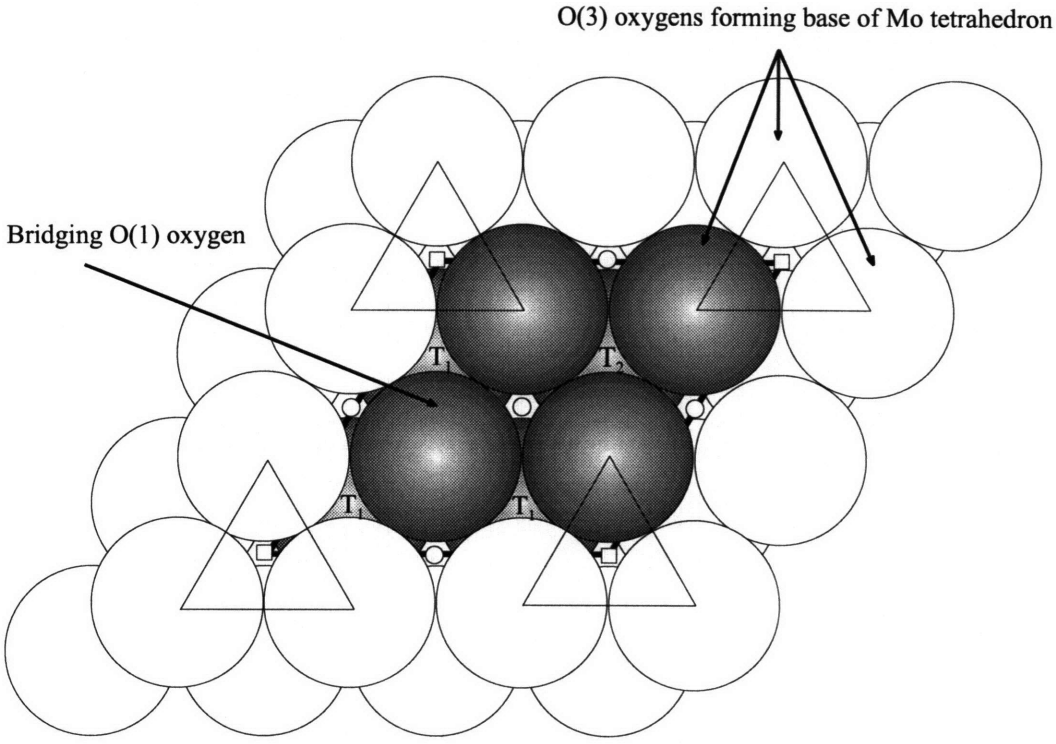

Note: Only upper 4 tetrahedral sites are visible

Legend:

□ Octahedral site which is permanently vacant

○ Octahedral site which may be occupied by Ni^{2+} cation

Figure 3.10. Arrangement of tetrahedral and octahedral sites within the unit cell area.

a Ni/Mo ratio of 0.75. In this compound, $(NH_4)H_2Ni_{1.5}(OH)_2(MoO_4)_2$, all the bridging O(1) atoms would be hydroxyls and each would have an associated hydrogen accommodated in its tetrahedral site, T_2. At this Ni/Mo ratio, all the tetrahedral sites having point symmetry *3m* would be occupied by hydrogens. It is therefore being proposed that the minimum in the Ni/Mo ratio is set by the inability of the structure to accommodate any more hydrogens required for charge balancing.

An attempt was made to verify these proposals. The synthesis of a deuterated analog of the Ni-LTM, $(ND_4)DNi_2(OD)_2(MoO_4)_2$, was attempted for investigation using neutron diffraction. While H_2O and NH_4OH could be readily substituted by commercially available D_2O and ND_4OD (Cambridge Isotope Laboratories, Inc., Andover, MA), problems arose in the elimination of protons present in the precursor salts $(NH_4)_6Mo_7O_{24}\cdot 4H_2O$ and $Ni(NO_3)_2\cdot 6H_2O$. The salts were dehydrated

in a furnace to eliminate the water of dehydration, but the protons remaining from the NH_4^+ ions could not be successfully eliminated. Refluxing the precipitated powder in a solution of ND_4Cl, prepared by neutralization of ND_4OD with DCl, was unable to exchange out the protons. This residual proton content resulted in a data set, collected on the BT1 neutron diffractometer at the National Institute of Standards and Technology (Gaithersberg, MD), that was not of a sufficient quality to allow for refinement of the hydrogen positions.

3.5. The Relationship between the LTM and LDH Crystal Structures

The crystal structure of Zn-LTM is related to the parent LDH. Both structures have, as a basic framework, sheets of zinc (and aluminum) octahedra running perpendicular to the *c* axis. The type and occupancy of the octahedral sites however, differ in the two structures. In the LDH framework, the metal cations fully occupy site 3(a), such that a_0 equals the cation-cation distance within the sheet (Figure 3.11 (a)). However, in the Zn-LTM structure, the metal cations occupy site 9(e) with variable occupancy. Consequently, *a* for the LTM structure depends on the Mo-Mo distance, a distance equivalent to that between consecutive ordered vacancies at the origin (Figure 3.11 (b)). In a LTM structure, there can be a maximum of three metal cations per layer in the unit cell. Typically, however, there are only two metal cations per layer in the unit cell, as is the case in Zn-LTM. If we define a supercell of the LDH with $a' = 2\ a_0$, $c' = c_0$, the area of the unit supercell would be almost identical to that of the LTM cell. In this equivalent area supercell however, there would be four metal cations per layer (Figure 3.11 (c)). Therefore, the *chimie douce* synthesis reaction, while reconstructing the fundamental layered nature of the structure from the metastable zincite phase, reduces the number of octahedrally coordinated cations in the layers.

This reduction in the number of cations determined crystallographically complements the elemental analysis of the Zn-LTM phase. Elemental analysis had shown that the final product contained only 0.63% Al. This suggested that, on reaction with the ammonium heptamolybdate solution, the tetrahedral Al in the zincite phase left the solid phase and entered into solution. XPS analyses of the elemental composition of the surface region of calcined Mg-Al LDHs reported in the literature have indicated that the surface regions were enriched in Al.[68] This evidence, together with the ^{27}Al NMR data, suggests that the reactivity of the calcined Zn_4Al_2-LDH results from the presence of the tetrahedrally coordinated Al. Upon reaction, the Al enters into solution, thereby preventing the reconstruction of the LDH phase (which requires a positively charged framework

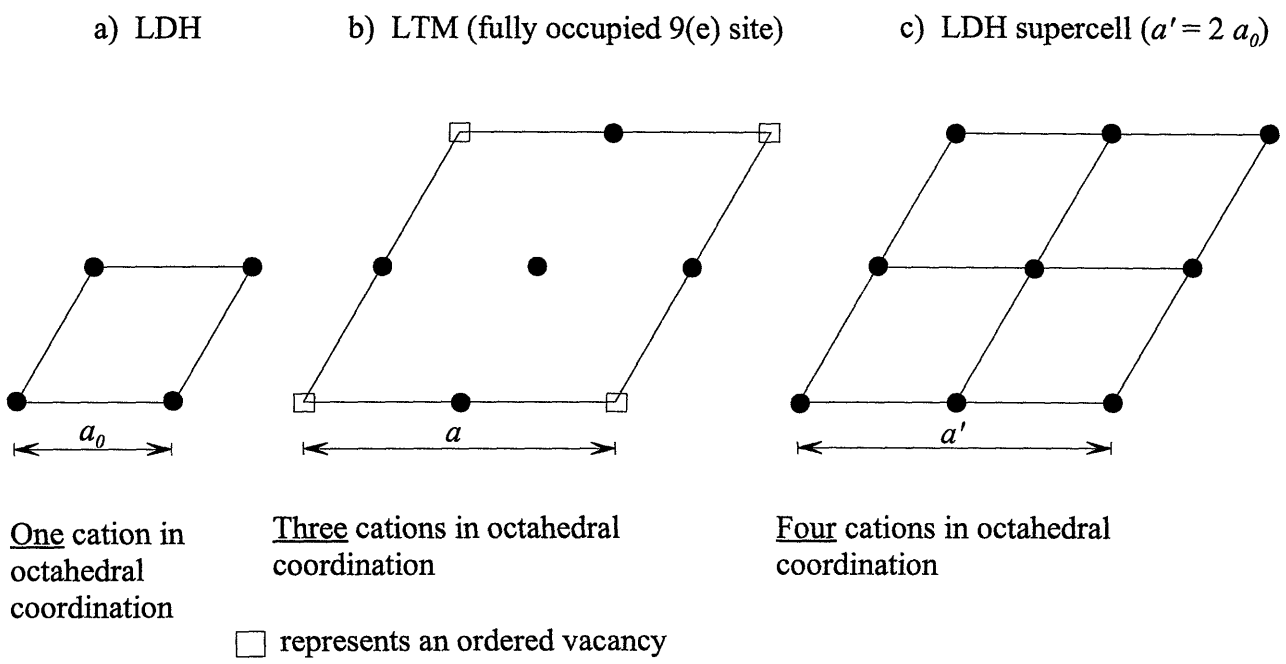

Figure 3.11. Variation in the number of cations in octahedral coordination resulting from *chimie douce* reaction.

resulting from trivalent cation substitution in the divalent lattice.) The loss of cations by this mechanism generates the vacancies in the octahedral sites of the oxide/hydroxide sheets required for the formation of the LTM structure.

Comparing the LTM structure with the LDH structure, it is interesting to note that the charge on the framework has been reversed. The LDH structure consists of positively charged sheets with intercalated anions such as CO_3^{2-} in the interlayer region. The LTM structure, however, consists of negatively charged layers, which leads to the incorporation of cations, e.g. NH_4^+, in the interlayer region. Therefore, this *chimie douce* reaction has changed not only the chemical and structural features of the LDH precursor, but its electronic nature as well.

4. NON-STOICHIOMETRIC TRANSITION METAL MOLYBDATES FROM LTM PRECURSORS

4.1. Synthesis

The transition metal molybdates were synthesized by calcination of layered transition metal molybdate (LTM) precursors. The precursors were synthesized by precipitation from aqueous solution, following the method described in section 2.2.2. Ammonium heptamolybdate (Aldrich Chemical Co.) and nitrate salts of nickel, cobalt, and zinc (99.999% purity, Aldrich Chemical Co.) were used to prepare LTM precursors for a series of stoichiometric transition metal molybdates of the form $A_{\epsilon}B_{1-\epsilon}MoO_4$, where A and B are Ni, Co or Zn, and $0 \leq \epsilon \leq 1$, as indicated in Table 4.1. A second series of LTM precursors was synthesized for the preparation of non-stoichiometric nickel molybdates of the form $Ni_{1+\delta}Mo_{1-\delta/3}O_4$ where $-1/5 \leq \delta \leq 1/3$, as shown in Table 4.2.

Table 4.1. Catalysts Derived from $(NH_4)HA_{2\epsilon}B_{2-2\epsilon}(OH)_2(MoO_4)_2$ Precursors

A/B Ratio	Precursor Formula	Catalyst Formula
N/A	$(NH_4)HNi_2(OH)_2(MoO_4)_2$	$NiMoO_4$
3	$(NH_4)HNi_{1.5}Co_{0.5}(OH)_2(MoO_4)_2$	$Ni_{0.75}Co_{0.25}MoO_4$
2	$(NH_4)HNi_{1.33}Co_{0.67}(OH)_2(MoO_4)_2$	$Ni_{0.67}Co_{0.33}MoO_4$
1	$(NH_4)HNiCo(OH)_2(MoO_4)_2$	$Ni_{0.5}Co_{0.5}MoO_4$
1/2	$(NH_4)HNi_{0.67}Co_{1.33}(OH)_2(MoO_4)_2$	$Ni_{0.33}Co_{0.67}MoO_4$
1/3	$(NH_4)HNi_{0.5}Co_{1.5}(OH)_2(MoO_4)_2$	$Ni_{0.25}Co_{0.75}MoO_4$
N/A	$(NH_4)HCo_2(OH)_2(MoO_4)_2$	$CoMoO_4$
N/A	$(NH_4)HZn_2(OH)_2(MoO_4)_2$	$ZnMoO_4$
1	$(NH_4)HNiZn(OH)_2(MoO_4)_2$	$Ni_{0.5}Zn_{0.5}MoO_4$

Table 4.2. Catalysts Derived from $(NH_4)H_{2x}Ni_{3-x}O(OH)(MoO_4)_2$ Precursors

x	Ni/Mo Ratio	Precursor Formula	Catalyst Formula	δ
0.0	1.5	$(NH_4)Ni_3O(OH)(MoO_4)_2$	$Ni_{1.333}Mo_{0.889}O_4$	0.333
0.5	1.25	$(NH_4)Ni_{2.5}(OH)_2(MoO_4)_2$	$Ni_{1.176}Mo_{0.941}O_4$	0.176
1.0	1.0	$(NH_4)HNi_2(OH)_2(MoO_4)_2$	$NiMoO_4$	0.000
1.25	0.875	$(NH_4)H_{1.5}Ni_{1.75}(OH)_2(MoO_4)_2$	$Ni_{0.903}Mo_{1.032}O_4$	-0.097
1.5	0.75	$(NH_4)H_2Ni_{1.5}(OH)_2(MoO_4)_2$	$Ni_{0.80}Mo_{1.067}O_4$	-0.200

The catalysts were prepared for characterization by calcination in air at 550 °C in a box furnace. For the catalytic studies, catalysts were prepared by *in situ* calcination of the LTM precursors at 550 °C. Thermogravimetric analysis on a Perkin Elmer Series 7 TGA showed that the weight loss was independent of the calcination atmosphere. The weight loss as a function of temperature is shown in Figure 4.1 for the preparation of a $NiMoO_4$ phase. The Ni-LTM phase decomposes with the loss of water and ammonia from the structure. Thermal analysis by differential scanning calorimetry on a Perkin Elmer Series 7 DSC showed that the transformation from the Ni-LTM to the $Ni_{1+\delta}Mo_{1-\delta/3}O_4$ phase occurred over a temperature range from 350 °C to 425 °C, as shown in Figure 4.2. These thermal analysis studies showed that at a temperature of 550 °C at which the transition metal molybdate phase was prepared, characterized, and studied for catalytic activity, the transformation from the LTM precursor was complete.

4.2. Characterization of Transition Metal Molybdates Prepared from LTM Precursors

The structure and properties of the stoichiometric transition metal molybdates, such as $NiMoO_4$, $ZnMoO_4$ and $CoMoO_4$, are fairly well known. As a result thereof, the research effort presented here is focused on understanding the structure and properties of a series of non-stoichiometric nickel molybdates of the form $Ni_{1+\delta}Mo_{1-\delta/3}O_4$, where $-1/5 \leq \delta \leq 1/3$. Specific attention was placed on understanding how the structure and properties of these nickel molybdates vary with a change in the Ni/Mo ratio.

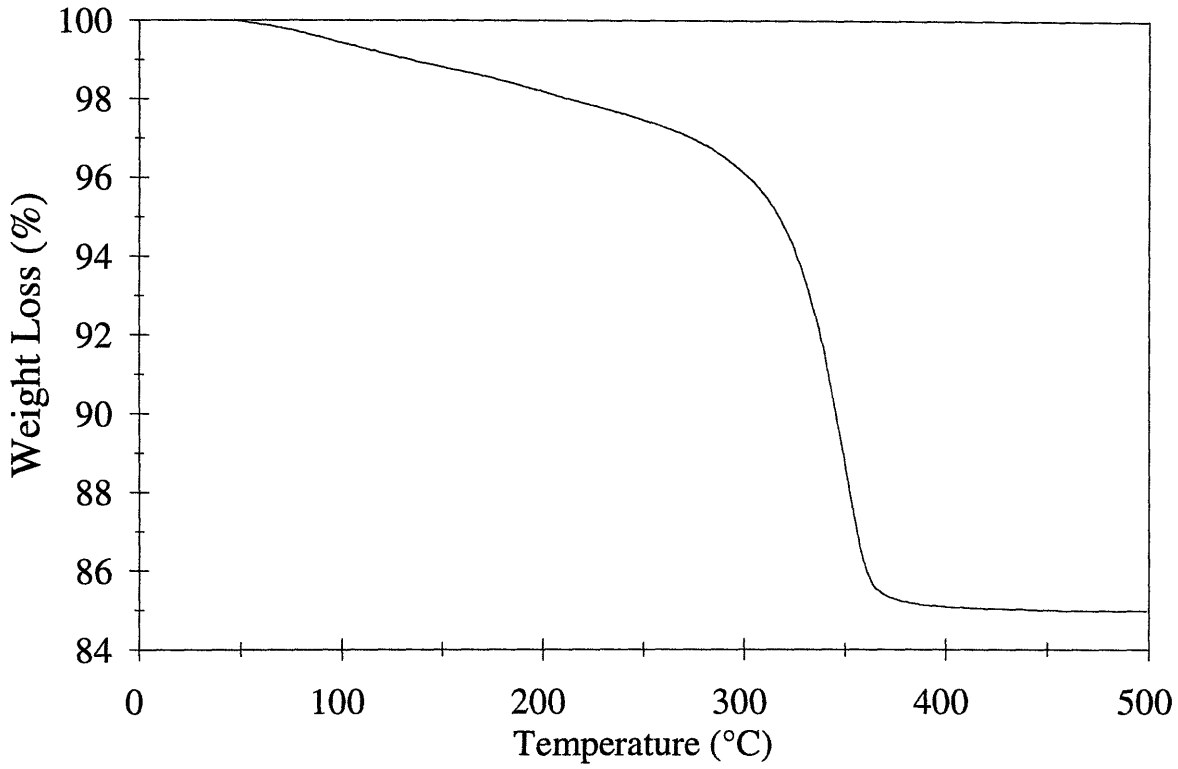

Figure 4.1. Weight loss as a function of temperature for the $(NH_4)HNi_2(OH)_2(MoO_4)_2 \rightarrow NiMoO_4$ transformation.

4.2.1. X-Ray Diffraction (XRD)

XRD patterns were collected using a Siemens D5000 θ/θ diffractometer operated at 45 kV and 40 mA with CuKα radiation from a sealed tube. XRD patterns of the precipitated LTM precursors and the calcined phases were collected at room temperature.

The room-temperature XRD patterns of the calcined transition metal molybdates were, however, not always true reflections of the actual phase present under reaction conditions due to a β→α phase transformation that occurs on cooling with Ni-based molybdates.[49] To fully characterize this phase, high temperature powder XRD patterns were collected with CuKα radiation using a Rigaku RU200 rotating anode θ/2θ diffractometer equipped with a Rigaku 2311B high temperature attachment. The high temperature attachment was controlled using a Rigaku PTC-10C programmable temperature controller. Due to the vertical alignment of the sample holder, the Ni-

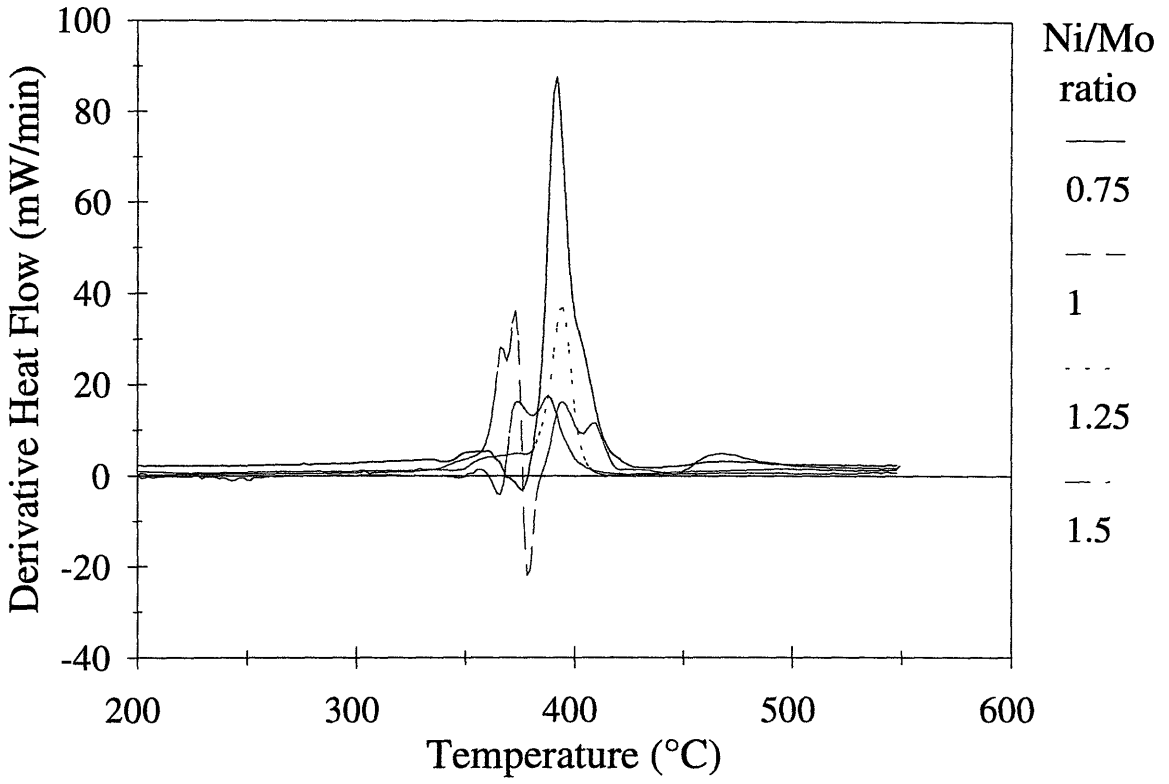

Figure 4.2. Derivative of heat flow (mW/min) for calcination of Ni-LTM phases.

LTM precursors were pressed into pellets of 8 mm diameter for analysis. The pellets were mounted to the vertical sample holder and held in place by two 0.008" platinum wires that ran across the upper and lower portion of the pellet face. For an analysis, the sample was ramped to 550 °C at a rate of 20 °C/min in air, and then held isothermally for 30 minutes before collecting a scan. Following this scan, the sample was ramped to 700 °C at a rate of 20 °C/min and held there for 30 minutes before a scan was collected.

4.2.2. B.E.T. Surface areas

B.E.T. surface areas were measured using a Micromeritics ASAP 2010 instrument by adsorption of nitrogen at 77 K. The samples were prepared by degassing at 150 °C for 2 hours.

4.2.3. Diffuse Reflectance Infrared Fourier Transform (DRIFT) Spectroscopy

The nature of the phase present under reaction conditions was further characterized by collecting infrared spectra of the materials following *in situ* calcination of the precursors in a high-temperature diffuse reflectance accessory. Infrared spectra were collected using a BioRad FTS-60A spectrometer equipped with a Harrick Scientific DRA3-HTC high temperature accessory. This accessory enabled a controlled atmosphere to be maintained around the sample under investigation. The Ni-LTM precursors, prepared as a 10 wt% mixture with KBr, were calcined with high purity He flowing through the cell at a rate of 30 ml/min. The DRIFT spectra were collected at a sample temperature of 550 °C.

4.2.4. Electrical Conductivity

The electrical conductivity of the series of non-stoichiometric nickel molybdates listed in Table 4.2 was characterized by 2-probe AC Impedance Spectroscopy. Initial attempts to characterize the electrical conductivity using 4-probe DC measurements were unsuccessful due to the mixed ionic/electronic nature of the material. On application of an applied voltage, the current decayed over time. The reason for this phenomena is the movement of vacancies and anions under the application of an external electric field that sets up an internal chemical potential by the separation of charged species, counteracting the external applied field. To overcome this complication, impedance spectroscopy,[78] an AC measurement technique, was used to determine the conductivity of the materials.

4.2.4.1. Theory

Impedance is to alternating current what resistance is to direct current. In a DC determination of resistance, measurement of the current (I) resulting from the application of a voltage (V) enables the resistance to be calculated by Ohm's law:

$$R = \frac{V}{I} \tag{4.1}$$

In an analogous fashion, a time-dependent sinusoidal voltage $V_\omega(t) = V_0\sin(\omega t)$ can be applied across a sample and the resulting time-dependent current $I_\omega(t) = I_0\sin(\omega t+\phi)$, where ω is the radial

frequency of the signal and ϕ is a phase shift, can be measured to enable the impedance to be calculated by

$$Z(\omega) = \frac{V_\omega(t)}{I_\omega(t)} \tag{4.2}$$

$Z(\omega)$ is, in general, a complex quantity, and can be represented as a magnitude and phase, $|Z(\omega)|e^{-i\phi}$, or as the sum of real and imaginary terms, $Z(\omega) = Z_\omega' + i\,Z_\omega''$, where $Z_\omega' = |Z(\omega)|\cos(\phi)$ and $Z_\omega'' = |Z(\omega)|\sin(\phi)$. Z_ω'' is often plotted against Z_ω' as a function of the frequency of the applied signal to enable the resistance of the sample to be determined.

Figure 4.3 shows the RC-circuit diagram for a simple system consisting of a single RC-circuit, and the expected impedance data. The impedance of a single parallel RC-circuit is given by:[79]

$$Z(\omega) = \frac{1}{\frac{1}{R} + i(2\pi\omega)C} \tag{4.3}$$

where R is the resistance of the resistant element (Ω), C is the capacitance of the capacitive element (Farads), *i* is the square root of -1, and ω is the frequency (Hz). The real and imaginary parts of $Z(\omega)$ can be determined by multiplying equation (4.3) by its complex conjugate, giving

$$Z_\omega' = \frac{1/R}{(1/R)^2 + (2\pi\omega C)^2} \tag{4.4}$$

$$Z_\omega'' = \frac{2\pi\omega C}{(1/R)^2 + (2\pi\omega C)^2} \tag{4.5}$$

The frequency can be eliminated from equations (4.4) and (4.5), resulting in the equation for a circle with center at (R/2,0) and radius R/2:

$$(Z_\omega'')^2 + \left(Z_\omega' - \frac{R}{2}\right)^2 = \frac{R^2}{4} \tag{4.6}$$

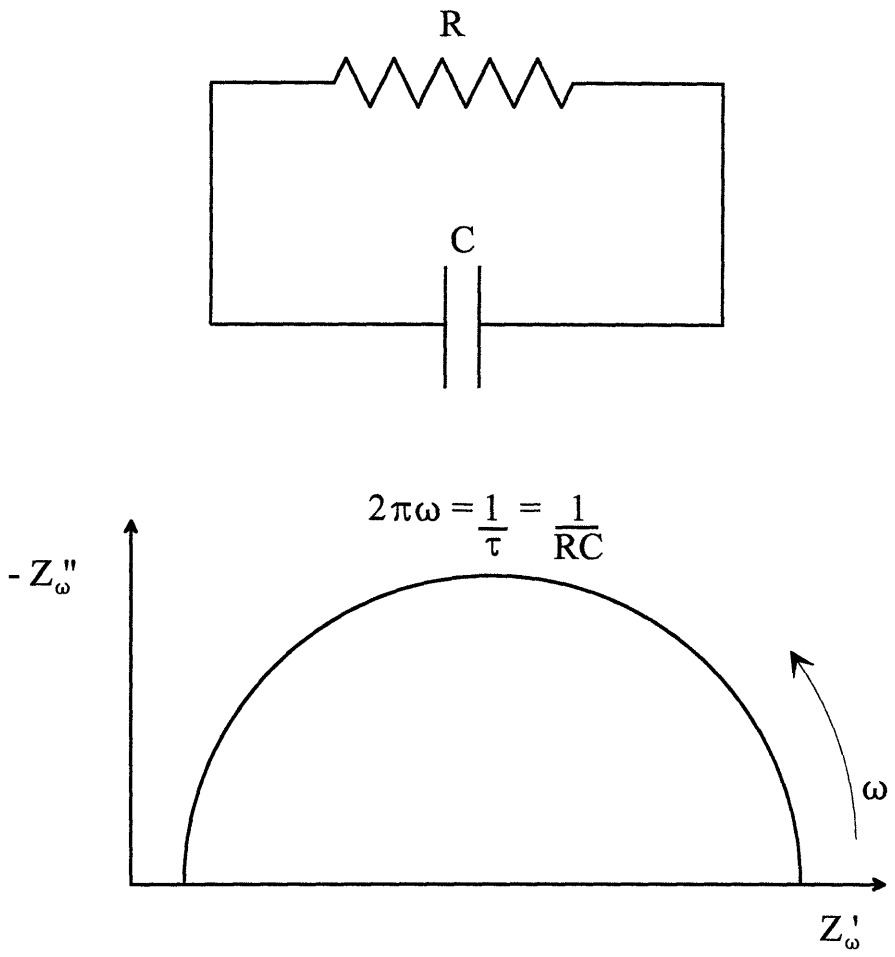

Figure 4.3. RC-circuit diagram for single resistor and capacitor in parallel.

The value for R may therefore be determined by fitting a semicircle to a plot of $-Z_\omega''$ against Z_ω'. (It is convention to reverse the sign of Z_ω'' so that the semicircle is in the first quadrant rather than the fourth quadrant.) To determine the value of C, Z_ω' may be substituted by R/2, its value at the peak of the semicircle, in equation (4.4) to give

$$2\pi\omega = \frac{1}{RC} \tag{4.7}$$

Typically, the resistor R represents a conductive path, while the capacitor C represents a space-charge or interface contribution. These parameters are "lumped", with a single time constant

τ = RC representing the dielectric relaxation time of the material.[78] The resistance (R) and capacitance (C) may, however, represent a distribution of elements having a distribution of time constants. In practice, this leads to the experimental data generally not forming full semicircles centered on the real axis of the complex plane. The center of the experimental arcs is frequently displaced below the real axis, as shown in Figure 4.4. The angle θ by which the semicircular arc is displaced below the real axis is related to the width of the distribution of time constants.[78]

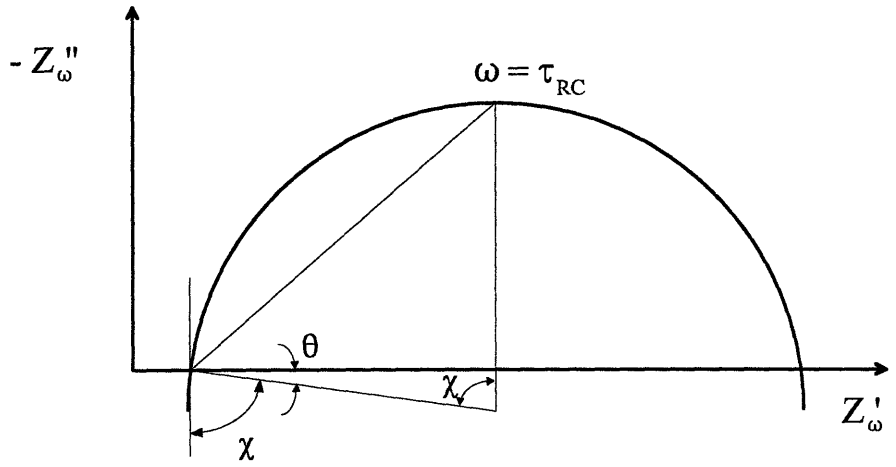

Figure 4.4. Impedance plane plot for a depressed circular arc.

4.2.4.2. Conductivity Dependence on Oxygen Partial Pressure

Measurement of the conductivity of a sample as a function of the partial pressure of oxygen provides important insights into the nature of the conduction process. The dependence of conductivity on oxygen partial pressure can be used to distinguish between two main types of point defects. Doubly-ionized oxygen vacancies $V_O^{\cdot\cdot}$ are in equilibrium with oxygen according to the equation

$$O_O \Leftrightarrow \frac{1}{2} O_2(g) + V_O^{\cdot\cdot} + 2e' \qquad (4.8)$$

which has the mass-action equilibrium constant

$$K_1(T) = K_1^0 \exp\left(\frac{-\Delta H_1}{kT}\right) = \frac{\left[V_O^{\cdot\cdot}\right]\left[e'\right]^2 P_{O_2}^{1/2}}{\left[O_O\right]} \tag{4.9}$$

where K_1^0 is a constant and ΔH_1 is the enthalpy of reduction per $V_O^{\cdot\cdot}$. If reaction (4.8) is the dominant mechanism, electroneutrality is given by $2\left[V_O^{\cdot\cdot}\right] = \left[N_M'\right]$, and since the concentration of oxygen ions is not significantly changed ($[O_O] \approx 1$),

$$\left[e'\right] \propto P_{O_2}^{-\frac{1}{4}} \tag{4.10}$$

and a plot of log σ against log P_{O_2} should have a slope of -1/4.

Doubly ionized cationic vacancies V_M'' are in equilibrium with oxygen according to the equation

$$\frac{1}{2} O_2(g) \Leftrightarrow O_O + V_M'' + 2h^{\cdot} \tag{4.11}$$

which has the mass-action equilibrium constant

$$K_2(T) = K_2^0 \exp\left(\frac{-\Delta H_2}{kT}\right) = \frac{\left[O_O\right]\left[V_M''\right]\left[h^{\cdot}\right]^2}{P_{O_2}^{1/2}} \tag{4.12}$$

where K_2^0 is a constant and ΔH_2 is the enthalpy of oxidation per V_M''. If reaction (4.11) is the dominant mechanism, electroneutrality is given by $\left[h^{\cdot}\right] = 2\left[V_M''\right]$, and since the concentration of oxygen ions is not significantly changed ($[O_O] \approx 1$),

$$\left[h^{\cdot}\right] \propto P_{O_2}^{+\frac{1}{6}} \tag{4.13}$$

and a plot of log σ against log P_{O_2} should have a slope of +1/6.

4.2.4.3. Experimental Setup

To measure DC and AC conductivity, a tube furnace was set up in which a sample could be held in a controlled atmosphere, thereby allowing measurements at varying temperatures and oxygen partial pressures. A schematic of the equipment setup is shown in Figure 4.5. The sample temperature was monitored by a platinum/rhodium thermocouple located at the same axial position in the furnace tube as the sample. Radial temperature gradients within the 1" O.D. alumina furnace tube were assumed to be negligible. To control the atmosphere within the tube furnace, a series of MKS Mass Flow Controllers were used to provide O_2/Ar gas mixtures. With cylinders of pure O_2 and Ar (both Grade 5 UHP, BOC Gases), the lowest concentration of O_2 possible was 2 % due to the inability of the mass flow controller to accurately meter out a gas flow less than 2 % of the full scale of the controller (50 sccm). To achieve lower concentrations of O_2, a certified gas mixture that was 5.01% O_2 in Ar was purchased (BOC Gases). Mixing of this gas mixture with Ar allowed a minimum O_2 concentration of 0.25% to be achieved. The experimental setup was constructed using stainless steel tubing, stainless steel valves, and high purity regulators with stainless steel diaphragms to prevent outgassing of the surfaces.

The equipment setup shown in Figure 4.5 allowed for the collection of either 4-probe DC measurements or 2-probe AC measurements. For the DC measurements, a Keithley Model 236 Source Measure Unit (SMU) was used. This SMU has the capability to source either voltage (±100 μV to ±110 V) or current (±100 fA to ±100 mA) and measure the resulting current (±10 fA to ±100 mA) or voltage (±10 μV to ±110 V). For the AC measurements, a Solartron 1260 Impedance/Gain-Phase analyzer was used. The 1260 unit has a built in synthesizer that produces a stable voltage or current drive over the frequency range 10 μHz to 32 MHz. The reported accuracy of the 1260 unit for impedance measurements of resistance is 0.1% to 10^5 Ω, 1% to 10^7 Ω, and 10% to 10^8 Ω.

A key feature of this experimental setup involved the design of a suitable electrode system that would provide contacts of good electrical and mechanical quality. The materials under investigation introduced certain limitations on the type of electrode that could be used. Typically, conductivity studies are performed on ceramic materials that can be sintered at high temperatures to provide strong, dense pellets that can be machined and subjected to other forms of mechanical and thermal treatments. This allows for specific bonds between the material under investigation and the electrode material to be generated by high-energy processes including sputtering, soldering

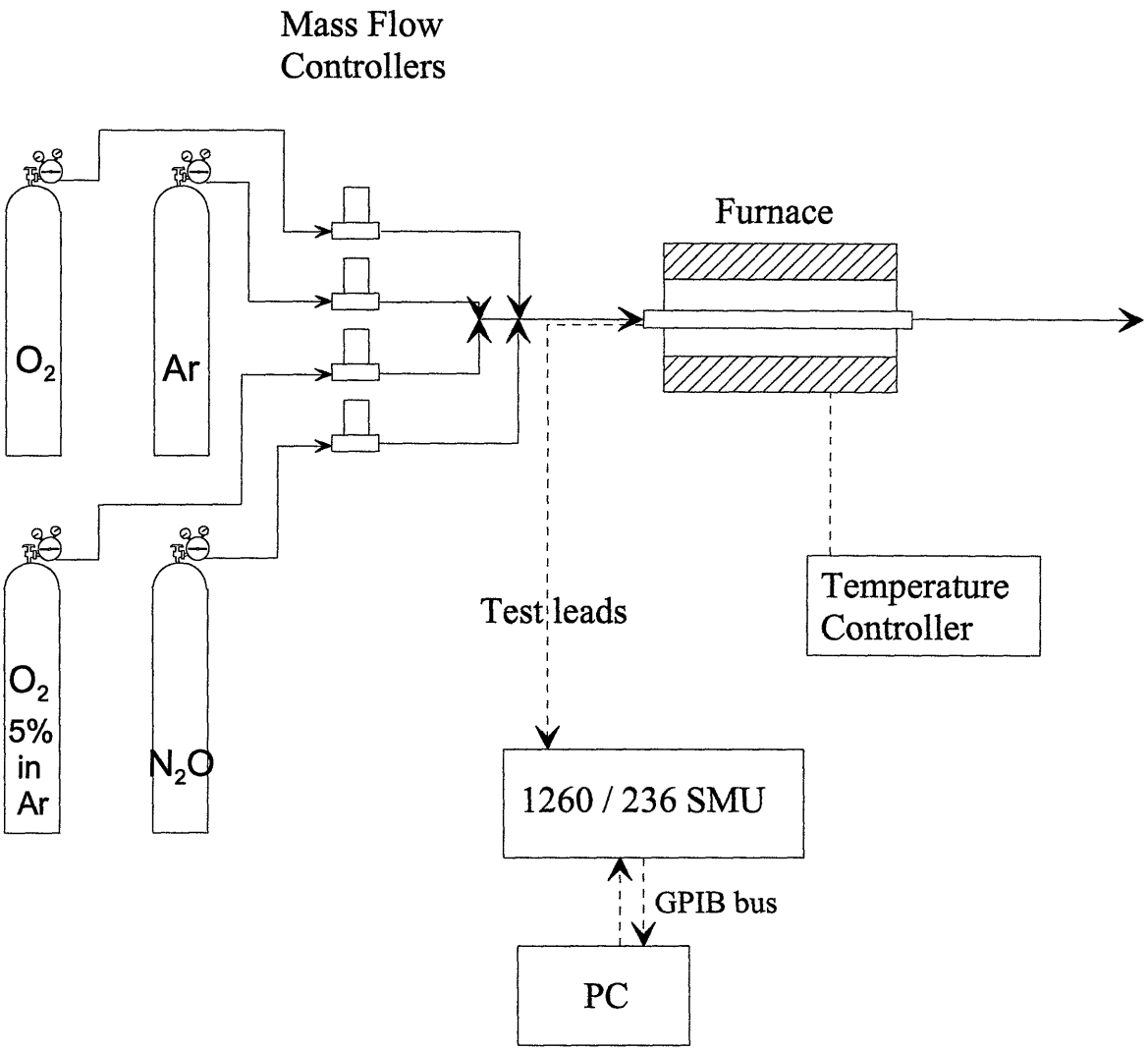

Figure 4.5. Schematic of apparatus for conductivity measurements.

and furnace-cured paints or pastes. The nickel molybdates under investigation though, do not allow for any type of thermal treatment due to the metastability of the β-phase at elevated temperatures that cause them to revert to the α phase on cooling to room temperature. The β→α phase transformation involves a volume change of about 6% that could lead to the separation of an electrode, assuming that an electrode could be applied at elevated temperatures. It would be preferable to have an electroding technique that would allow for a good contact to be maintained through an LTM → β-phase transformation. This led to the use of a mechanical bond formed by wedging a platinum electrode material to the face of a pellet of the specimen under investigation.

It was also desirable to have a setup in which the position of the electrodes was fixed, and therefore did not change as various different samples were investigated. To accomplish these goals, a sample holder, shown schematically in Figure 4.6, was designed and custom machined from 98% Al_2O_3 (Ellis Ceramics, Inc., Bowling Green, KY). This sample holder was designed to reduce variability in the electrode/sample interface between various samples being measured. The electrode positions were fixed by the sample holder, and did not depend on the sample itself. Platinum was used as the electrode material, with the Pt leads being shielded by a 4-bore alumina tube. This design allowed for both 4-probe DC and 2-probe AC conductivity measurements to be performed on the same sample. When performing 2-probe AC conductivity measurements, electrodes 1 and 3 were coupled together, as were electrodes 2 and 4.

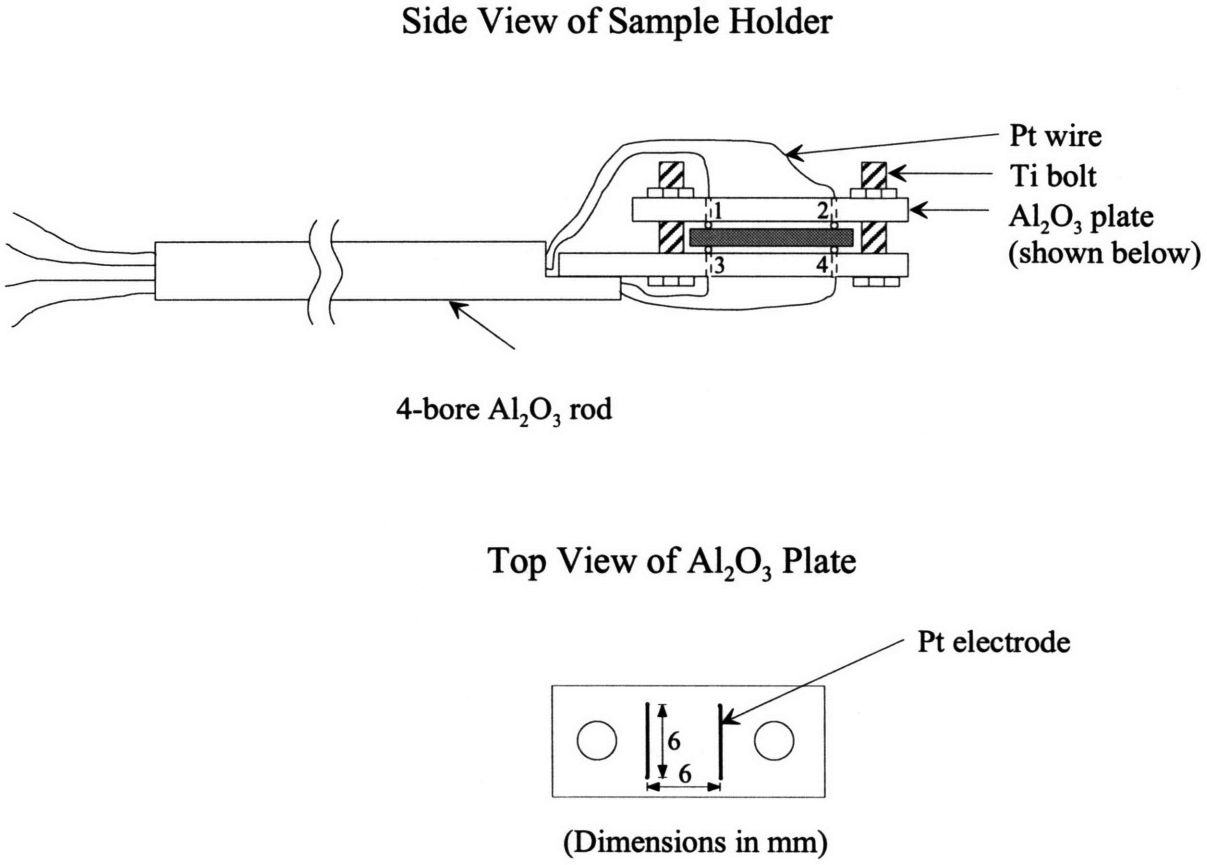

Figure 4.6. Schematic of sample holder for electrical conductivity measurements.

4.2.4.4. Impedance Measurements

The electrical conductivity was measured on samples that had been pressed into cylindrical pellets under a pressure of 2300 kg/cm^2. The initial weight of the pellet was 150 mg. The pellet diameter was 10 mm, and the thickness of the LTM pellet was typically 0.93 mm. After calcination and the conclusion of the experiment, the pellet thickness was redetermined to allow for calculation of the electrical conductivity. The pellet thickness of the nickel molybdate phase was typically 0.86 mm.

AC impedance measurements were performed using a Solartron 1260 Impedance/Gain-Phase analyzer. Control of the analyzer and the collection of data occurred over a GPIB computer interface using Z-60/Z-View for Windows software (Scribner Associates, Inc.). Measurements were collected by controlling the current at 3 mA and sweeping the frequency from 5 MHz down to 1 Hz in logarithmic steps of 10 per decade. Impedance measurements were performed over a temperature range of 630 °C to 550 °C. The resistance of the samples was too high to allow for measurements to be taken at temperatures below 550 °C. Measurements were performed by either holding the temperature constant at 575 °C and varying the O_2 partial pressure from 0.25 kPa to 50 kPa, or by holding the O_2 partial pressure constant and varying the temperature. Before taking any measurements, pellets of the LTM precursor were calcined in 0.25 kPa of O_2 at 700 °C for 1 hour, followed by calcination at 575 °C for 12 hours. This pretreatment was necessary to burn off any hexadecanoic acid used as a lubricant on the pellet die, and to ensure that no shrinkage of the pellet occurred during data collection at the lower temperatures. In a series of experiments, three measurements would be taken at each of various temperatures in 12 - 15 °C intervals from 630 °C to 550 °C, after which the P_{O_2} and the temperature would be raised. Measurements were always collected on the cooling cycle for each P_{O_2} value. The sample was allowed to equilibrate for at least 30 minutes before a measurement was performed.

All the experimental data collected in the study on non-stoichiometric nickel molybdates were in the form of depressed, single arcs. The data were therefore fitted to an equivalent RC circuit consisting of a single resistor and capacitor in parallel, as shown in Figure 4.3. From the fitting parameters, the resistivity (R) was determined, enabling calculation of the electrical conductivity by to the equation:

$$\sigma = \frac{1}{\rho} = \frac{L}{A} \cdot \frac{1}{R} \qquad (4.14)$$

where σ = electrical conductivity ($S.cm^{-1}$), ρ = specific resistivity (Ω.cm), R = resistivity (Ω), A = cross-sectional area of pellet (cm^2), and L = distance between electrodes (cm).

The temperature dependence of the conductivity of a sample typically follows an Arrhenius-type relationship, where

$$\sigma = \frac{\sigma_0}{T} \exp\left(\frac{-E_a}{kT}\right) \qquad (4.15)$$

Consequently, a plot of ln (σT) as a function of the inverse temperature should be linear, and an estimate of the activation energy, E_a, can be determined from the slope of the line.

In summary, the electrical conductivity measurements were performed on the series of non-stoichiometric nickel molybdates to determine the effect of the composition of these materials on the properties that could influence their catalytic performance. Any attempt to explain differences in electrical properties on this series of materials would, however, be futile without a full understanding of the nature of the phase of the materials at the conditions under which the conductivity measurements were performed.

4.3. Phase Determination of Non-Stoichiometric Nickel Molybdates

It was expected that the phase resulting from calcination of the ammonium nickel molybdate precursor, $(NH_4)H_{2x}Ni_{3-x}O(OH)(MoO_4)_2$ would be a form of $NiMoO_4$. Two questions, however, needed to be addressed: (i) which phase of $NiMoO_4$ existed under reaction conditions, and (ii) given the non-stoichiometry of the precursor phase that allowed for Ni/Mo ratios between 0.75 and 1.5, was a single phase of the form $Ni_{1+\delta}Mo_{1-\delta/3}O_4$ produced on calcination?

Besides the LTM precursor that would yield a stoichiometric $NiMoO_4$, precursors having a Ni/Mo ratio of 0.75 and 1.5 were chosen for the high temperature X-ray diffraction studies as they

represent the bounds on the Ni/Mo ratio set by the crystal structure of the layered ammonium nickel molybdate. This precursor, $(NH_4)H_{2x}Ni_{3-x}O(OH)(MoO_4)_2$, has an upper bound on the Ni/Mo ratio that is set by full occupancy of the Ni site. The lower bound on the Ni/Mo ratio is set by the inability of the LTM structure to accommodate further additional protons required for charge balancing as the occupancy of the Ni site is reduced to its minimum value of 1/2. The XRD patterns of the phases present at 550 °C resulting from *in situ* calcination of these three precursors are shown in Figure 4.7. In this figure, two strong peaks at approximately 39° and 46° 2θ have been removed - these peaks correspond to platinum (PDF # 4-0802) and resulted from the presence of two 0.008" platinum wires that ran across the face of the pellet to attach it to the vertical sample holder. This figure clearly shows all three phases to be the same, with no additional phases arising as the Ni content is increased. By comparing the XRD patterns with that of α-$NiMoO_4$ (PDF # 33-0948), it can be concluded that the phase at 550 °C is not the α phase.

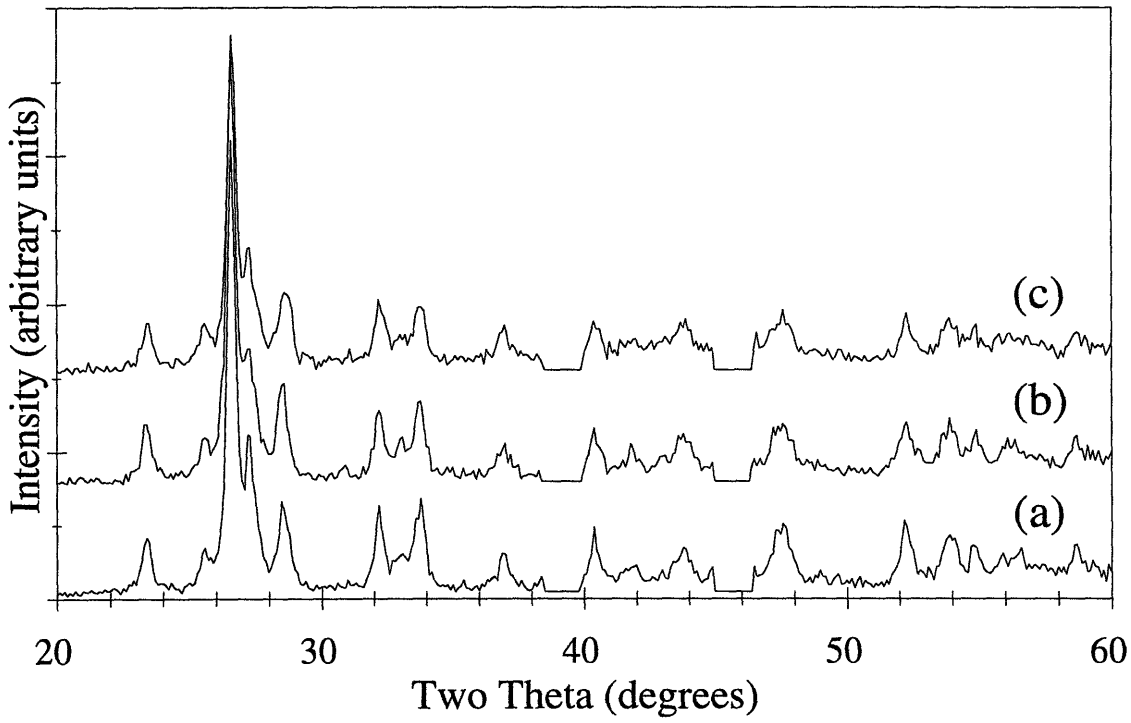

Figure 4.7. XRD patterns collected at 550 °C following *in situ* calcination of precursors with a Ni/Mo ratio of (a) 0.75, (b) 1.0, and (c) 1.5.

To definitively determine that the phase represented by the XRD patterns shown in Figure 4.7 is indeed that of β-$NiMoO_4$, a powder pattern for β-$NiMoO_4$ was simulated using GSAS.[72] It is known that β-$NiMoO_4$ is isostructural to α-$MnMoO_4$, the structure of which has been previously determined.[36] Starting with the structure of α-$MnMoO_4$, the structure of β-$NiMoO_4$ could be modeled by replacing Mn with Ni on the 4(h) and 4(i) crystallographic positions, as detailed in Table 4.3. Cell dimensions of a = 10.13 Å, b = 9.28 Å, c = 7.02 Å, and β = 107.2° were used.[39] Peak broadening was simulated using a multi-term Simpson's rule integration of the pseudo-Voigt function,[80] as implemented in GSAS. Gaussian profile coefficients of U = 200, V = -100, W = 20, Lorentzian coefficients of X = 1, Y = 35, and an asymmetry correction factor of 3 were used. These values represent a rounded average of profile functions used to fit powder X-ray data of the precursors assumed to have a similar particle size to the calcined powders. The simulated powder pattern for β-$NiMoO_4$ is shown in Figure 4.8. Comparison of the experimental XRD patterns shown in Figure 4.7 to the simulated pattern definitively confirms that the phase present at 550 °C following calcination of the $(NH_4)H_{2x}Ni_{3-x}O(OH)(MoO_4)_2$ ($0 \leq x \leq 3/2$) precursors is β-$NiMoO_4$.

Table 4.3. Structure Model for β-$NiMoO_4$.

Atom	Wykoff	*x*	*y*	*z*
Ni (1)	4(h)	0	0.183	1/2
Ni (2)	4(i)	0.7953	0	0.1387
Mo (1)	4(g)	0	0.2516	0
Mo (2)	4(i)	0.2707	0	0.4050
O (1A)	4(i)	0.3587	1/2	0.4635
O (1B)	4(i)	0.2029	0	0.1534
O (2)	8(j)	0.1369	0.3548	0.1083
O (3)	8(j)	0.4584	0.3455	0.1904
O(4)	8(j)	0.3645	0.1504	0.4698

The high-temperature diffraction studies also clearly show that no NiO exists as a secondary phase. Previous studies on the stability of β-$NiMoO_4$ have assumed that NiO exists as a secondary phase due to the presence of a diffraction peak at ~37° 2θ with CuKα radiation.[54] Nickel oxide

does have a Bragg reflection at 37.2°, in addition to reflections at 43.3° and 62.9°, but the presence of a peak at 37.2° cannot be used to confirm the presence of NiO since β-$NiMoO_4$ has a (400) reflection at 37.1°, as shown in Figure 4.8. In addition, the peak at 37° in Figure 4.7(a) for the phase with a Ni/Mo ratio of 0.75 would not be present if this peak was due to the presence of "excess" Ni as NiO. The high-temperature XRD studies of these materials covering a Ni/Mo ratio of 0.75 to 1.5 showed that no diffraction peaks arose at 43.3° that would indicate the presence of NiO.

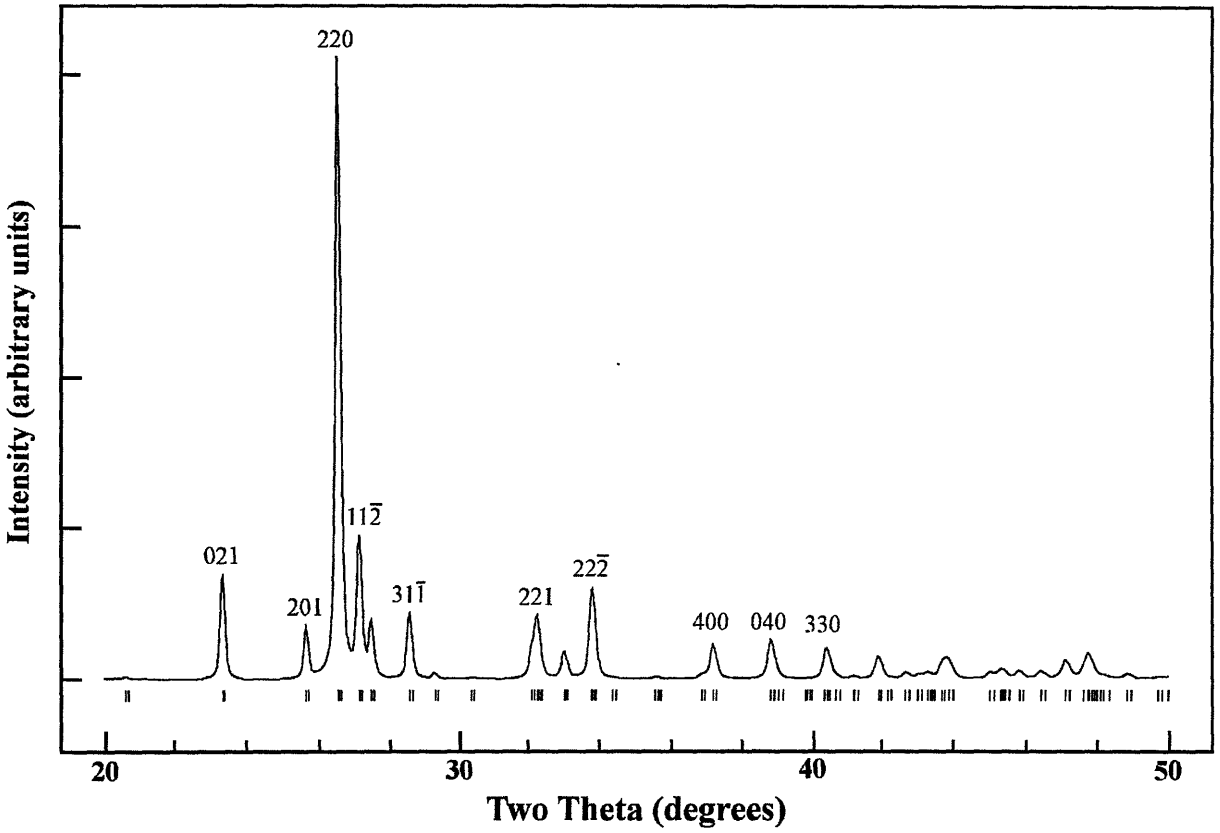

Figure 4.8. Simulated diffraction pattern of β-$NiMoO_4$. The set of short vertical bars below the pattern indicate the position of possible Bragg reflections.

The presence of a pure phase of β-$Ni_{1+\delta}Mo_{1-\delta/3}O_4$ at a temperature of 550 °C results from the use of the $(NH_4)H_{2x}Ni_{3-x}O(OH)(MoO_4)_2$ precursor. If this β-$Ni_{1+\delta}Mo_{1-\delta/3}O_4$ is subsequently allowed to cool back down to room temperature, the material undergoes a β→α phase transformation. Reheating of this α phase to 550 °C does not, however, produce the β phase, as shown in Figure 4.9. In accordance with results published in the literature,[47] a temperature of at least 700 °C was

required to transform the α phase back to the β phase. Since the surface area of the catalyst decreases with an increase in the calcination temperature, the production of a β-nickel molybdate from the α phase is undesirable. All materials tested for catalytic activity were therefore prepared by *in situ* calcination of the LTM precursors to yield the β phase directly.

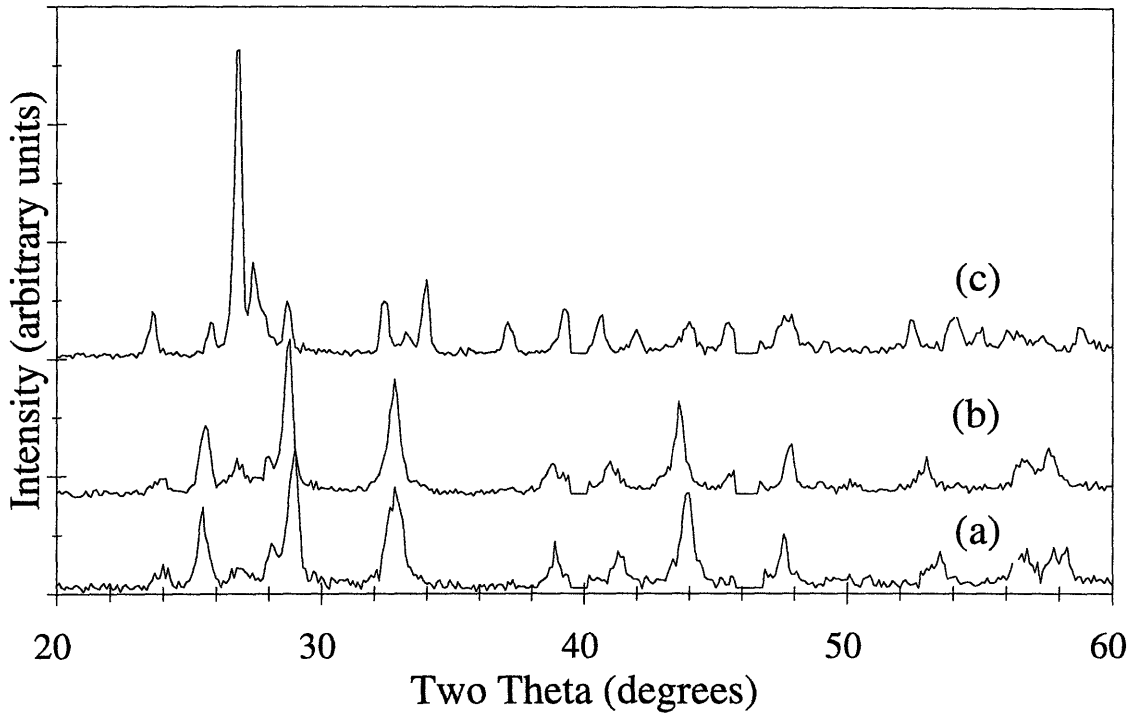

Figure 4.9. XRD patterns of (a) α-$NiMoO_4$ derived by precalcining Ni-LTM at 550 °C, scanned at 25 °C, (b) material in (a) reheated to 550 °C, and (c) material in (a) heated to 700 °C.

The normal stretching modes of the molybdate ions were expected to occur in the region 700-1000 cm^{-1}.[81] Figure 4.10 shows the DRIFT spectra of the phases present at 550 °C resulting from *in situ* calcination of the three precursors having a Ni/Mo ratio of 0.75, 1, and 1.5. This figure shows that all three materials, representing the full range of Ni/Mo ratios possible, have identical stretching modes. The four bands present between 700 and 1000 cm^{-1} suggest that the coordination around the molybdenum ions is tetrahedral. The bands centered at 945 cm^{-1} and 709 cm^{-1} can be assigned to a symmetric stretching vibration and an asymmetric stretch, respectively.[81] The bands centered at 872 cm^{-1} and 799 cm^{-1} can be assigned to ν_1 and ν_3 modes, respectively, noting that the

intensity of ν_3 is slightly greater than that of ν_1, as is typical with oxometallates.[81] These spectra confirm that the phase present under reaction conditions is the β-phase, characterized by a tetrahedral coordination around the molybdenum atoms. These spectra also show that the local oxygen environment surrounding the molybdenum atoms is independent of the Ni/Mo ratio.

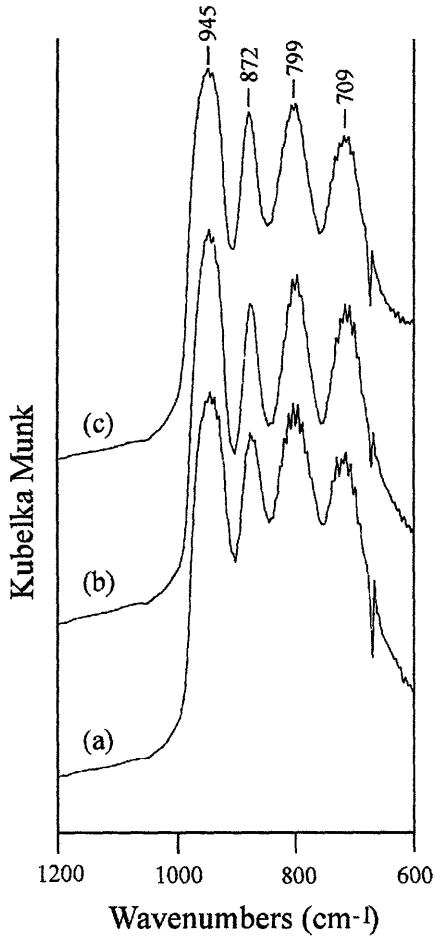

Figure 4.10. DRIFT spectra collected at 550 °C following *in situ* calcination of Ni-LTM precursors with a Ni/Mo ratio of (a) 0.75, (b) 1.0, and (c) 1.5.

4.4. Surface Area Determination of Non-Stoichiometric Nickel Molybdates

The surface areas of the catalysts were determined by assuming that the surface area of the α phase of the nickel molybdates at room temperature was approximately the same as the β phase at 550 °C. The surface areas of the nickel molybdates studied for catalytic activity are presented

in Table 4.4. The surface areas do not correlate to the Ni/Mo ratio and are essentially equal to 44 ± 5 m^2/g. On the basis of these determinations, surface area can be dismissed as a parameter explaining any possible trends in catalytic performance that are present as a function of the Ni/Mo ratio. The B.E.T. surface area of the catalyst calcined at 700 °C was determined to be 22 m^2/g. Therefore, the *in situ* calcination of the LTM precursors to yield the β phase directly at 550 °C results in a 100% improvement in the surface area over a catalyst prepared conventionally by calcination of the α phase.

Table 4.4. B.E.T. Surface Areas of $Ni_{1+\delta}Mo_{1-\delta/3}O_4$ Series Catalysts

Catalyst	B.E.T. Surface Area (m^2/g)
$Ni_{1.333}Mo_{0.889}O_4$	46.7
$Ni_{1.176}Mo_{0.941}O_4$	43.8
$NiMoO_4$	49.4
$Ni_{0.903}Mo_{1.032}O_4$	44.8
$Ni_{0.8}Mo_{1.067}O_4$	38.7

4.5. Modeling the Defect Structure of Non-Stoichiometric Nickel Molybdates

The high temperature X-ray diffraction studies showed that the precursor phases having Ni/Mo ratios between 0.75 and 1.5 produced a single phase isostructural to β-$NiMoO_4$ upon calcination at 550 °C. This non-stoichiometric phase is proposed to have the general formula $Ni_{1+\delta}Mo_{1-\delta/3}O_4$, where δ represents the departure from stoichiometry and $-1/5 \leq \delta \leq 1/3$. This phase can be considered as a combination of the constituent binary oxides NiO and MoO_3, where

$$Ni_{1+\delta}Mo_{1-\delta/3}O_4 = (1 + \delta)\ NiO + (1 - \delta/3)\ MoO_3 \qquad \textbf{(4.16)}$$

To fully understand the behavior of the non-stoichiometric nickel molybdates, a knowledge of the defect chemistry of this ternary ionic crystal is required. In formulating the balance relationships and equilibria existing between various point defects, a basic assumption made is that the point defects can be treated thermodynamically as quasi-particles dissolved in the crystal.[82] It was further assumed that the point defects did not interact with each other.

In order to formulate an unambiguous set of disorder relationships and internal equilibria, the notation of Kröger and Vink[83] will be used to represent defects as chemical species. The defect is represented by a main symbol followed by a subscript and superscript. The main symbol indicates the species concerned that is either an atom represented by its chemical symbol, or a vacancy, V. The subscript shows the site at which the species sits, with interstitial sites designated as $_i$. The superscript shows the effective electrical charge of the defect, with positive effective charges shown as dots (·) and negative effective charges shown as dashes (′). The superscript on a neutral defect is left blank. Table 4.5 lists some examples relevant to the Ni-Mo-O system.

Table 4.5. Kröger and Vink Notation for Some Defects in Ni-Mo-O System.

Notation	Defect
Ni_{Ni}	Nickel cation on its regular lattice site
$Ni_i^{\cdot\cdot}$	Nickel cation on an interstitial site
$V_{Ni}^{//}$	Nickel vacancy
$Ni_{Mo}^{////}$	Nickel cation on regular lattice site of Mo cation

Similar symbols are used for anionic point defects. In addition, the symbol e' will be used to represent an excess electron and $h^{\cdot}$ will be used to represent an electron hole. Despite the structurally non-equivalent lattice positions for Ni and Mo in the structure of β-$NiMoO_4$ (Table 4.3), no differentiation of the sites will be made when setting up the defect chemistry. In developing the defect chemistry relationships for the Ni-Mo-O system, the nickel and molybdenum atoms will initially be considered to be in a +2 and +6 valence state, respectively, and electronic disorder will initially be assumed to be negligible. This analysis of the defect chemistry will therefore only be valid at constant P_{O_2} and will be used primarily as a tool to identify the majority point defects existing in the non-stoichiometric nickel molybdates.

4.5.1. Balance Relationships for Ionic Point Defects in Ternary Molybdates

The non-stoichiometric nickel molybdate can be considered to be composed of its constituent binary oxides NiO and MoO_3 in a variable ratio. In general, if the Ni and Mo concentrations are allowed to vary independently of each other, the non-stoichiometric nickel molybdate can be considered in the form

$$(1 + \alpha)\,NiO \cdot (1 + \beta)\,MoO_3 = Ni_{1+\alpha}Mo_{1+\beta}O_{4+\alpha+\beta} \qquad \textbf{(4.17)}$$

Defining w to be the difference between the number of interstitial oxygens and the number of oxygen vacancies,

$$w = O_i'' - V_O'' \qquad \textbf{(4.18)}$$

the average number of oxygen anions is $4(1 - w)$, and by comparison to equation (4.17),

$$\alpha + \beta + 4w = 0 \qquad \textbf{(4.19)}$$

The nickel molybdate can be characterized chemically by the ratio of the two constituent oxides:

$$(1 + \beta) / (1 + \alpha) \equiv 1 + y \qquad \textbf{(4.20 a)}$$

Therefore, for small deviations from the ideal stoichiometric formula,

$$1 + y \cong 1 + \beta - \alpha \qquad \textbf{(4.20 b)}$$

Equations (4.20 b) and (4.20 a) define y as a measure of the deviation from the ideal stoichiometry. From equations (4.19) and (4.20), it follows that

$$\alpha = -\tfrac{3}{4}\,y - w \qquad \textbf{(4.21)}$$

and

$$\beta = \tfrac{1}{4}\,y - w \qquad \textbf{(4.22)}$$

Using these relations, one can write balance equations for all the ions in the Ni-Mo-O system.

$$[Ni_{Ni}] + [Ni_{Mo}] + [Ni_i] = 1 + \alpha = 1 - \tfrac{3}{4}\,y - w \qquad \textbf{(4.23)}$$

$$[Mo_{Mo}] + [Mo_{Ni}] + [Mo_i] = 1 + \beta = 1 + \tfrac{1}{4}\,y - w \qquad \textbf{(4.24)}$$

$$[O_O] + [O_i] = 4 + \alpha + 3\beta = 4 - 4w \qquad \textbf{(4.25)}$$

A further set of balance equations can be obtained by summing up all the regular sites.

$$[Ni_{Ni}] + [Mo_{Ni}] + [V_{Ni}] = 1 \quad \textbf{(4.26)}$$

$$[Mo_{Mo}] + [Ni_{Mo}] + [V_{Mo}] = 1 \quad \textbf{(4.27)}$$

$$[O_O] + [V_O] = 4 \quad \textbf{(4.28)}$$

In deriving equations (4.23) to (4.28), it has been assumed that the transition metal cations cannot be substituted for oxygen anions on their regular sites, and vice versa. Equations (4.23) to (4.28) can now be combined to obtain a set of equations involving only defect concentrations related to the deviation from the ideal stoichiometry:

$$[Mo_{Ni}] + [V_{Ni}] - [Ni_{Mo}] - [Ni_i] - \tfrac{1}{4}([V_O] - [O_i]) = \tfrac{3}{4}\,y \quad \textbf{(4.29)}$$

$$[Mo_{Ni}] - [V_{Mo}] - [Ni_{Mo}] + [Mo_i] + \tfrac{1}{4}([V_O] - [O_i]) = \tfrac{1}{4}\,y \quad \textbf{(4.30)}$$

$$[V_O] - [O_i] = w \quad \textbf{(4.31)}$$

Equations (4.29) to (4.31) can be used to catalog the possible combinations of ionic disorder with two different kinds of point defects. In doing this, the condition of electrical neutrality for the crystal as a whole has been taken into account. Therefore, in equations (4.23) to (4.28), only those combinations of defects that can occur which satisfy these equations with positive concentrations were considered for $y \cong 0$ (ideal stoichiometry), $y > 0$ (excess of MoO_3) and $y < 0$ (excess of NiO). The results are presented in Table 4.6.

Table 4.6. Ionic Disorder Types with Two Different Kinds of Point Defects

Defect	$Ni_i^{\cdot\cdot}$	$Mo_i^{\cdot\cdot\cdot\cdot\cdot\cdot}$	$V_{Ni}^{//}$	$V_{Mo}^{//////}$	$Ni_{Mo}^{////}$	$Mo_{Ni}^{\cdot\cdot\cdot\cdot}$	$V_O^{\cdot\cdot}$	$O_i^{//}$
$Ni_i^{\cdot\cdot}$			$y \cong 0$	$y < 0$	$y < 0$			$y < 0$
$Mo_i^{\cdot\cdot\cdot\cdot\cdot\cdot}$			$y > 0$	$y \cong 0$	$y < 0$			$y > 0$
$V_{Ni}^{//}$	$y \cong 0$	$y > 0$				$y > 0$	$y > 0$	
$V_{Mo}^{//////}$	$y < 0$	$y \cong 0$				$y > 0$	$y < 0$	
$Ni_{Mo}^{////}$	$y < 0$	$y < 0$				$y \cong 0$	$y < 0$	
$Mo_{Ni}^{\cdot\cdot\cdot\cdot}$			$y > 0$	$y > 0$	$y \cong 0$			$y > 0$
$V_O^{\cdot\cdot}$			$y > 0$	$y < 0$	$y < 0$			$y \cong 0$
$O_i^{//}$	$y < 0$	$y > 0$				$y > 0$	$y \cong 0$	

If the concentration of oxygen defects is small in comparison to the concentration of cationic defects, then the possible combinations of defects reduces to those shown in Table 4.7. The ratio of concentrations of the two majority defects constituting a disorder type can be obtained by applying the condition of electrical neutrality, as shown in Table 4.7.

Table 4.7. Defect Concentration Relations for Cationic Disorder Types in $NiMoO_4$.

$y < 0$	$[Ni_i^{\cdot\cdot}] = 3\,[V_{Mo}^{////}]$	$[Ni_i^{\cdot\cdot}] = 2\,[Ni_{Mo}^{////}]$	$3\,[Mo_i^{\cdot\cdot\cdot\cdot\cdot\cdot}] = 2\,[Ni_{Mo}^{////}]$
$y \cong 0$	$[Mo_i^{\cdot\cdot\cdot\cdot\cdot\cdot}] = [V_{Mo}^{////}]$	$[Mo_{Ni}^{\cdot\cdot\cdot\cdot}] = [Ni_{Mo}^{////}]$	$[Ni_i^{\cdot\cdot}] = [V_{Ni}^{//}]$
$y > 0$	$3\,[Mo_i^{\cdot\cdot\cdot\cdot\cdot\cdot}] = [V_{Ni}^{//}]$	$2\,[Mo_{Ni}^{\cdot\cdot\cdot\cdot}] = [V_{Ni}^{//}]$	$2\,[Mo_{Ni}^{\cdot\cdot\cdot\cdot}] = 3\,[V_{Mo}^{////}]$

4.5.2. The Defect Structure of Non-Stoichiometric Nickel Molybdate

According to equations (4.29) to (4.31), the deviation from ideal stoichiometry is always proportional to the concentrations of the majority point defects of the corresponding disorder type. If $y < 0$, corresponding to an excess of NiO, the nickel molybdate exists with a net excess of cations. As can be seen in the catalyst formulae of Table 4.2, $(N_{Ni} + N_{Mo}) / 2 > 1$ for $Ni/Mo > 1$, where N_i is the number of cations of type *i*. Based on the defect concentration relations tabulated in Table 4.7, it is proposed that the non-stoichiometric nickel molybdates having a Ni/Mo ratio greater than one have interstitial Ni atoms as the major defects that are compensated for by the presence of Mo vacancies.

If $y > 0$, corresponding to an excess of MoO_3, the nickel molybdate exists with a net deficiency of cations. As can be seen in the catalyst formulae of Table 4.2, $(N_{Ni} + N_{Mo}) / 2 < 1$ for $Ni/Mo < 1$, where N_i is the number of cations of type *i*. Based on the defect concentration relations tabulated in Table 4.7, it is proposed that the non-stoichiometric nickel molybdates having a Ni/Mo ratio less than one have Ni vacancies as the major defects that are compensated for by either interstitial Mo atoms, or Mo atoms occupying Ni sites.

4.6. Electronic Properties of Non-Stoichiometric Nickel Molybdates

The modeling of the defect chemistry of the series of non-stoichiometric nickel molybdates presented in Section 4.5 served only to identify the majority point defects that account for the ability to synthesize nickel molybdates isostructural to β-$NiMoO_4$ having Ni/Mo ratios varying between 0.75 and 1.5. Two of the key assumptions made in Section 4.5 were constant valency of the transition metal cations and negligible electronic disorder. However, in addition to the intrinsic atomic disorder discussed in Section 4.5, extrinsic atomic disorder exists as a result of variable valency of the cations, and as a result of further adjustments in the stoichiometry due to variations in the partial pressure of one of the crystal components in the surrounding atmosphere. These variations are small relative to the ionic disorder, and concentrations of electrons and electron holes could therefore be disregarded in setting up the balance equations. However, when analyzing the electronic properties of these systems, the electronic defects make an essential contribution to the electrical conduction because the mobilities of the electronic defects are, in general, several orders of magnitude greater than those of interstitial ions or vacancies. If the concentration of ionic carriers is large, however, substantial fractions of both electronic and ionic contributions to the overall conductivity exist, and the material is termed a mixed conductor.

If the defect concentrations in a material are known, one can use knowledge of the defect mobilities to construct the conductivity behavior. Experimentally, the situation is reversed - given the electrical conductivity behavior, can the defect chemistry of the solid be constructed? In order to attempt this, further experimental data, beyond a measurement of the electrical conductivity, as outlined in Section 4.2.4, is required. The following information is required: ionic and transport numbers (obtained using concentration cells, polarization studies), the number of charges carried by the majority ionic carrier (concentration cells), and the concentration and sign of the charge of the majority electronic carrier (measurements of the Hall or Seebeck effect). This type of study is clearly beyond the focus of this thesis. The studies on the electrical properties of the series of nickel molybdates sought to investigate whether any dependence of the conductivity on the Ni/Mo ratio of the materials exists. Given that most catalytic reactions taking place on the surface of an oxide are redox-type reactions involving the transfer of electron density between reactants and the catalyst surface, an understanding of the electronic properties of a catalyst, even a partial understanding, will help to explain the relationship between the materials properties and its catalytic activity.

4.6.1. Experimental Results

All the experimental data collected in the conductivity study on non-stoichiometric nickel molybdates were in the form of depressed, single arcs. This behavior is very different to that typically seen with dielectric materials for which multiple arcs are noted. This multiple arc behavior is typically modeled using equivalent circuits consisting of three parallel RC units, representing the bulk phase, the grain boundary interface, and the electrode as separate units. The single arc behavior therefore leads to the assumption that a single conduction pathway dominates the conductance of the non-stoichiometric nickel molybdates.

In analyzing the conductance of the non-stoichiometric nickel molybdates, it is important to develop a physical model describing the mechanism of conduction. The conductivity study on the non-stoichiometric nickel molybdates differs from typical conductivity studies on ceramic materials due to differences in the pellet morphologies. Ceramic pellets prepared for conductivity studies are typically densified at high temperatures to achieve as close to full density as possible. In such pellets, the material can be considered as a collection of crystallites separated by grain boundaries, leading to both bulk and grain boundary pathways for conduction. The powder compacts of the non-stoichiometric nickel molybdates were, however, quite porous, with densities estimated to be only 42% of their theoretical value. The preparation of fully dense nickel molybdates is complicated by phase changes occurring on changes in temperature, and by the relatively high volatility of MoO_3 when compared to NiO that could lead to changes in the Ni/Mo ratio of the material on high-temperature sintering. The value of the Ni/Mo ratio is the most important parameter in the electrical conductivity studies, and a pellet that was a higher percentage of full density but having an unknown Ni/Mo ratio is essentially useless. A physical model describing the conduction pathway through a porous pellet is therefore required.

The pellets of the non-stoichiometric nickel molybdates can be modeled as a three-dimensional network of roughly spherical grains that forms under the application of pressure. In such a model, three regions are distinguishable: the particle bulk, assumed to be capable of chemical reduction only by the inward diffusion of oxygen vacancies from the surface, and therefore contributing little to the conduction; the "near" surface, assumed to be capable of oxidation or reduction by the surrounding atmosphere, as well as being capable of exchanging vacancies with the bulk; and the surface/gas interface where chemisorption/physisorption take place. This model

is similar to one used to describe the electrical properties of bismuth iron molybdate ($Bi_3FeO_4(MoO_4)_2$)[84-86] that was based on three premises:[84] (i) the near surface dominates the conductance; (ii) the bulk region acts as a vacancy reservoir, with vacancy exchange rates dependent on the diffusion constant; and (iii) chemisorbed oxygen on the surface reduces the conductance of the near surface region by engaging otherwise free carriers. The single arc seen in the AC impedance spectroscopy of the nickel molybdates suggests that the single pathway dominating the conductance through the sample is through the near surface region.

The AC impedance measurements were performed by sourcing the current at 3 mA and sweeping the frequency. Attempts to measure the impedance of the nickel molybdates by sourcing a voltage and sweeping the frequency were unsuccessful. The reason for this dependence on the method may be a problem of contact resistance between the platinum wire and the pellet, assumed to be a fairly wide bandgap semiconductor. Sourcing the voltage at a low bias may lead to an electric field at the interface that is too low to cause tunnel breakdown of the contact resistance. Sourcing the current at 3 mA may lead to electric fields at the interface that eliminate the contact resistance, thereby removing one of the possible arcs from the impedance plot. Lacking data on the mobility of oxygen ions through the bulk of the beta phase of nickel molybdate, it is difficult to prove that bulk conductance is small, but the single arcs noted in all the AC impedance plots suggests that conductance in the nickel molybdates occurs through the near surface region.

The impedance data for a typical conductivity analysis are shown in Figure 4.11. These data were collected on a sample of $Ni_{0.903}Mo_{1.032}O_4$ at 587 °C in 1 kPa of O_2. Using Equation (4.6), a semicircle can be fitted to these data such that R can be calculated to be $1.3190 \times 10^8\ \Omega$, thereby allowing the determination of $C = 1.37756 \times 10^{-10}$ F by Equation (4.7). The conductivity of this sample under these conditions could then be determined using Equation (4.14) to be $\sigma = 8.82 \times 10^{-8}$ $S.cm^{-1}$. In this manner, the conductivity was determined for each of the non-stoichiometric nickel molybdates listed in Table 4.2 as a function of both temperature and oxygen partial pressure.

The conductivity data for each of the nickel molybdates tested were found to be functions of both temperature and P_{O_2}. As an example, the conductivity of the nickel molybdate having a Ni/Mo ratio of 0.75 is shown in Figure 4.12, where $\log(\sigma)$ is plotted as a function of the reciprocal temperature for two different O_2 partial pressures. As expected, the conductivity follows an Arrhenius type behavior, with an increase in conductivity with increasing temperature.

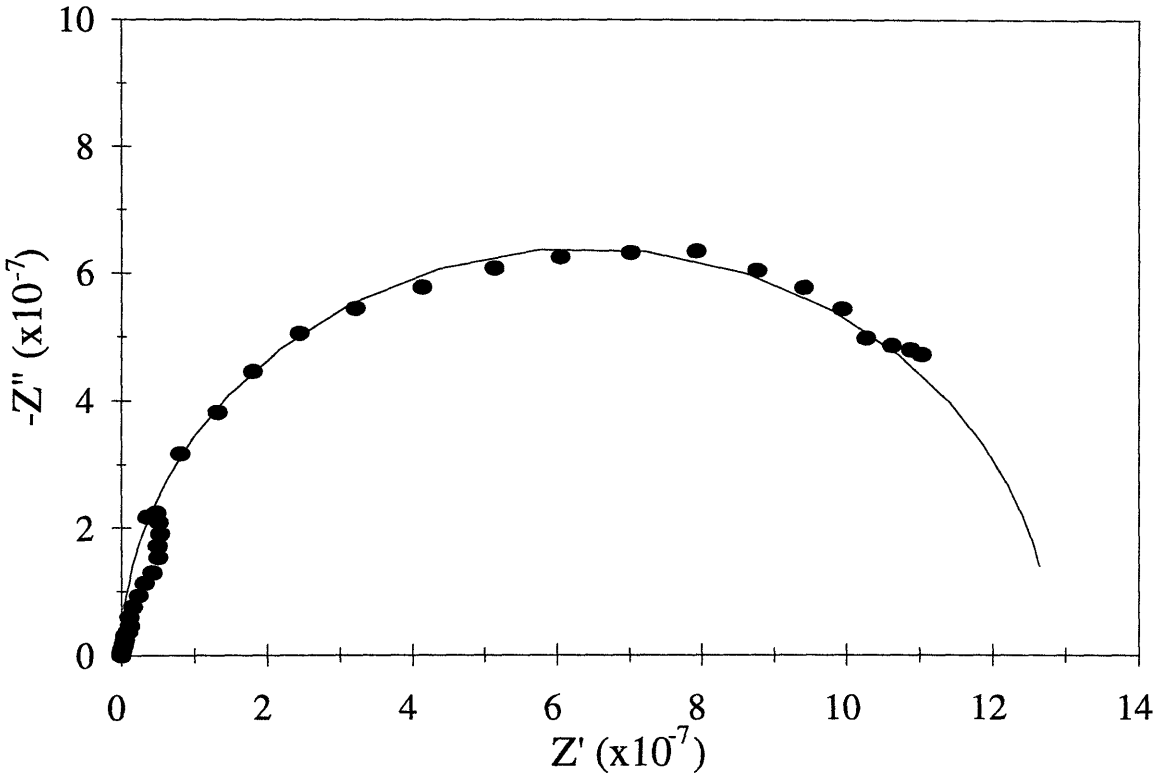

Figure 4.11. Impedance data for $Ni_{0.903}Mo_{1.032}O_4$ at 587 °C in 1 kPa of O_2.

The most important determination in the conductivity studies is the dependence of the conductivity on the partial pressure of oxygen. The composition of the nickel molybdate will change by the addition or removal of oxygen from the structure until an equilibrium is reached between the structure and its surrounding atmosphere. Figure 4.13 shows the dependence of the conductivity on the O_2 partial pressure at 575 °C for the nickel molybdates having Ni/Mo ratios of 0.75, 1.0, and 1.5. As can be seen from Figure 4.13, these three materials have very different dependencies on the partial pressure of O_2. At the lowest Ni/Mo ratio of 0.75, the conductivity decreases with increasing P_{O_2} due to the oxygen up-take by the near surface region, thereby engaging otherwise free carriers. At a P_{O_2} = 2 kPa, there is a change in the downward slope of the graph to a slope that is almost zero, suggesting that the maximum oxygen uptake has been reached, and that a possible change in the charge carrier has occurred. The stoichiometric $NiMoO_4$ also shows a decrease in the conductivity with increasing P_{O_2}, a trend that was constant over the 0.25 kPa to 20 kPa range investigated. Linear regression of the conductivity data for this material showed the slope to be -1/4.3, a value fairly close to a theoretical -1/4 that would indicate specific

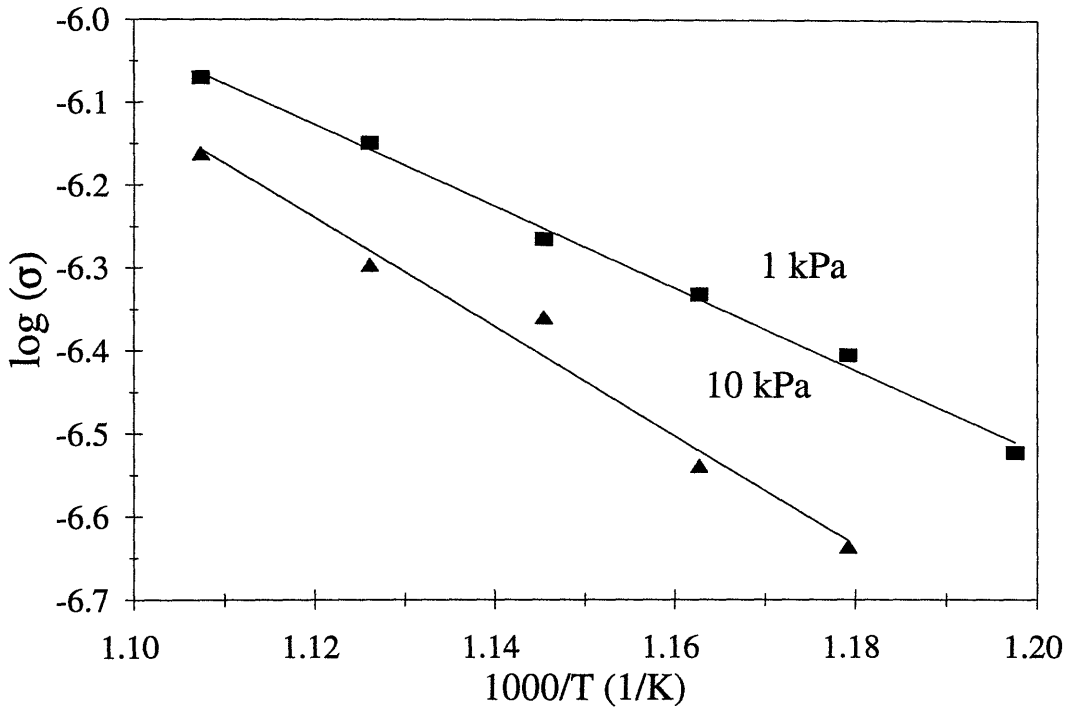

Figure 4.12. Conductivity of $Ni_{0.8}Mo_{1.067}O_4$ in 1 kPa and 10 kPa O_2, displaying Arrhenius-type behavior.

electronic defect chemistry. The conductivity of the stoichiometric $NiMoO_4$ is considerably smaller than that of the Ni-lean molybdate. Figure 4.13 shows, however, that the dependence of the conductivity on the O_2 partial pressure of the Ni-rich molybdate is completely opposite to the trends noted earlier for the stoichiometric and Ni-lean molybdates. The conductivity of the material with a Ni/Mo ratio of 1.5 increases with increasing P_{O_2}. Linear regression of the conductivity data for this material showed the slope to be +1/6.5, a value fairly close to a theoretical +1/6. At a $P_{O_2} < 10$ kPa, the conductivity decreases in the order Ni/Mo = 0.75 > Ni/Mo = 1 > Ni/Mo = 1.5.

The temperature dependence of the conductivity data showing an Arrhenius-type behavior allows for a determination of the activation energy, E_a, of the conduction process. As discussed in Section 4.2, a plot of ln ($\sigma \cdot T$) as a function of the reciprocal temperature should be linear, with the slope of the line being equal to $-E_a/k$, where k is the Boltzmann constant. As an example, the conductivity data for the nickel molybdate having a Ni/Mo ratio of 0.75 are shown in this format in Figure 4.14. Linear regression on these data enables the determination of E_a, the results of which

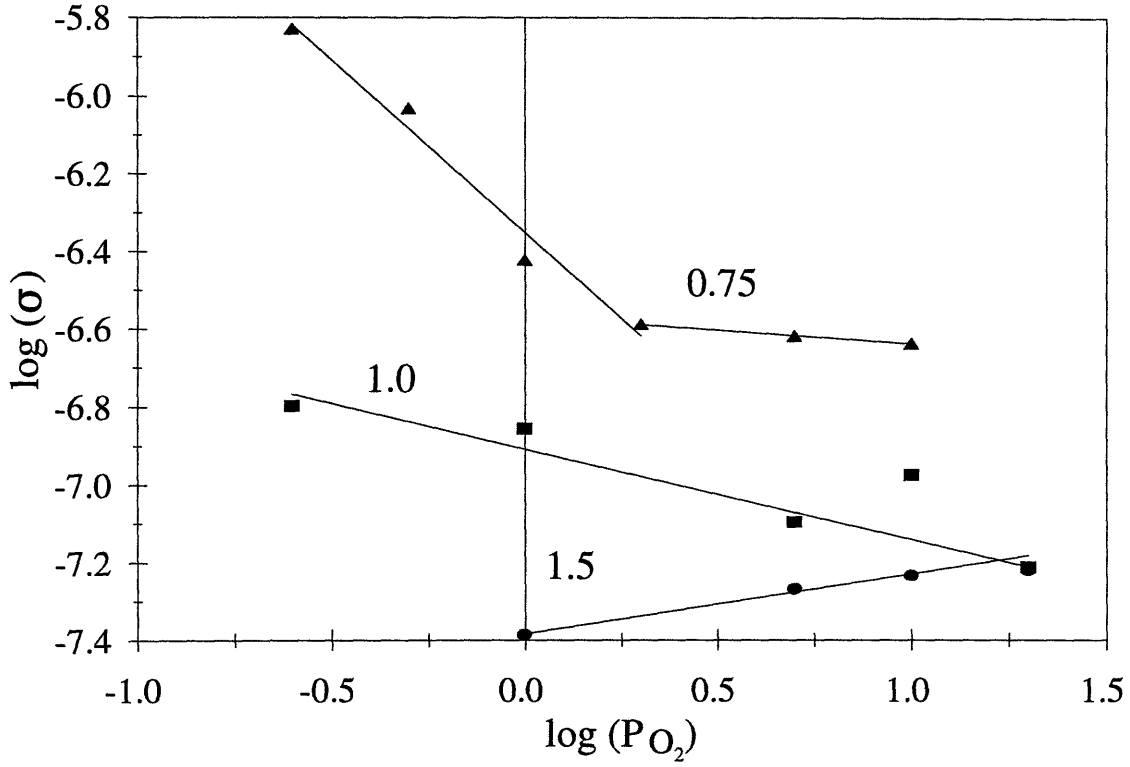

Figure 4.13. Dependence of conductivity on oxygen partial pressure (kPa) for materials with Ni/Mo ratios of 0.75, 1.0, and 1.5.

are tabulated in Table 4.8. As can be seen in Table 4.8., the activation energy for conduction decreases with decreasing Ni/Mo ratio.

Table 4.8. Activation Energy of Conduction at 1 kPa O_2.

Ni/Mo ratio	E_a (eV)
0.75	1.05
1.0	2.42
1.5	2.52

To investigate the dependence of the conductivity on the partial pressure of an oxidant other than oxygen, a determination of the conductivity of the nickel molybdate having a Ni/Mo ratio of 0.75 was carried out in an atmosphere of varying partial pressure of nitrous oxide (N_2O). It is known that N_2O decomposes into nitrogen and O^- ions by the following reaction:

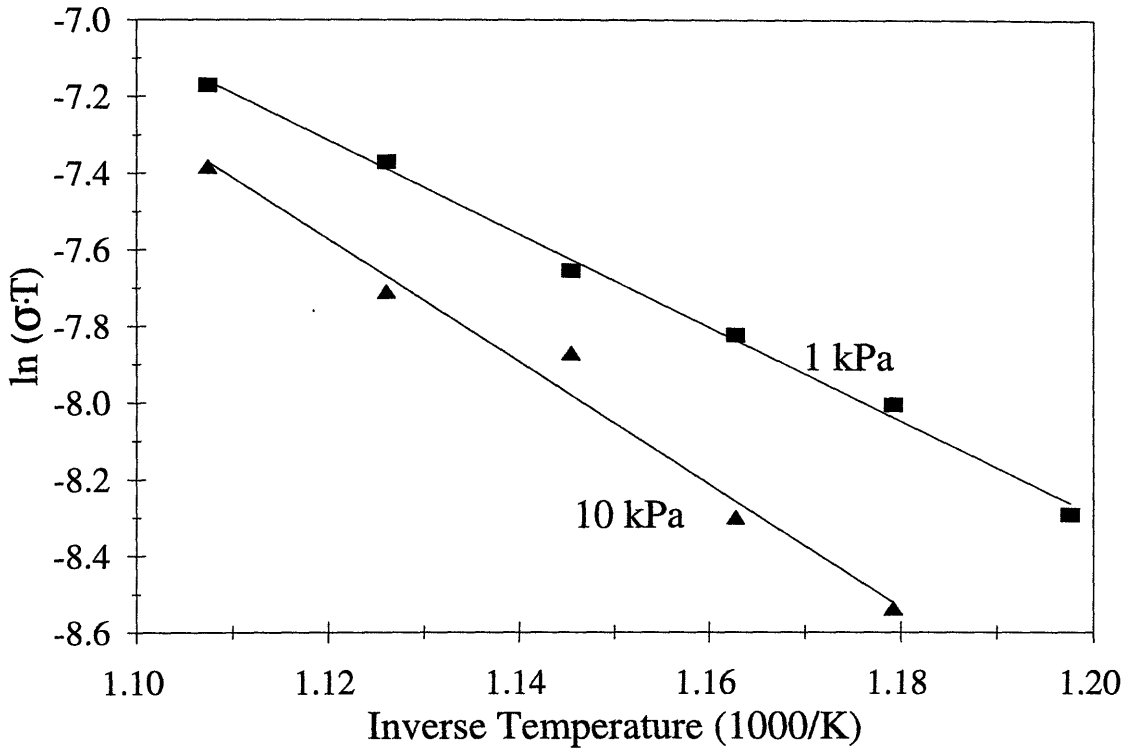

Figure 4.14. Conductivity of $Ni_{0.8}Mo_{1.067}O_4$ displaying Arrhenius-type behavior in format for the determination of E_a.

$$N_2O + e' \rightarrow N_2 + O^- \qquad \textbf{(4.32)}$$

The decomposition of N_2O is generally envisaged as a charge donation from the catalyst into the antibonding orbitals of N_2O, destabilizing the N-O bond and leading to its scission forming N_2 and a surface oxygen.[87] It would therefore be expected that the partial pressure of N_2O would have an influence on the conductivity, with N_2O tying up free electrons, but in doing so produce oxygen ions that may contribute towards ionic conduction. The dependence of the conductivity on the partial pressure of N_2O for the nickel molybdate having a Ni/Mo ratio of 0.75 is shown in Figure 4.15. This figure shows that the dependence of the conductivity on the N_2O partial pressure is completely opposite to the trend noted earlier for the conductivity in an O_2 environment. The conductivity of the material with a Ni/Mo ratio of 0.75 increases with increasing P_{N_2O}. Linear regression of the conductivity data for this material showed the slope to be +1/4.0, a value fairly close to a theoretical +1/3. It is interesting to note that the conductivity of the most Ni-lean molybdate displays the same

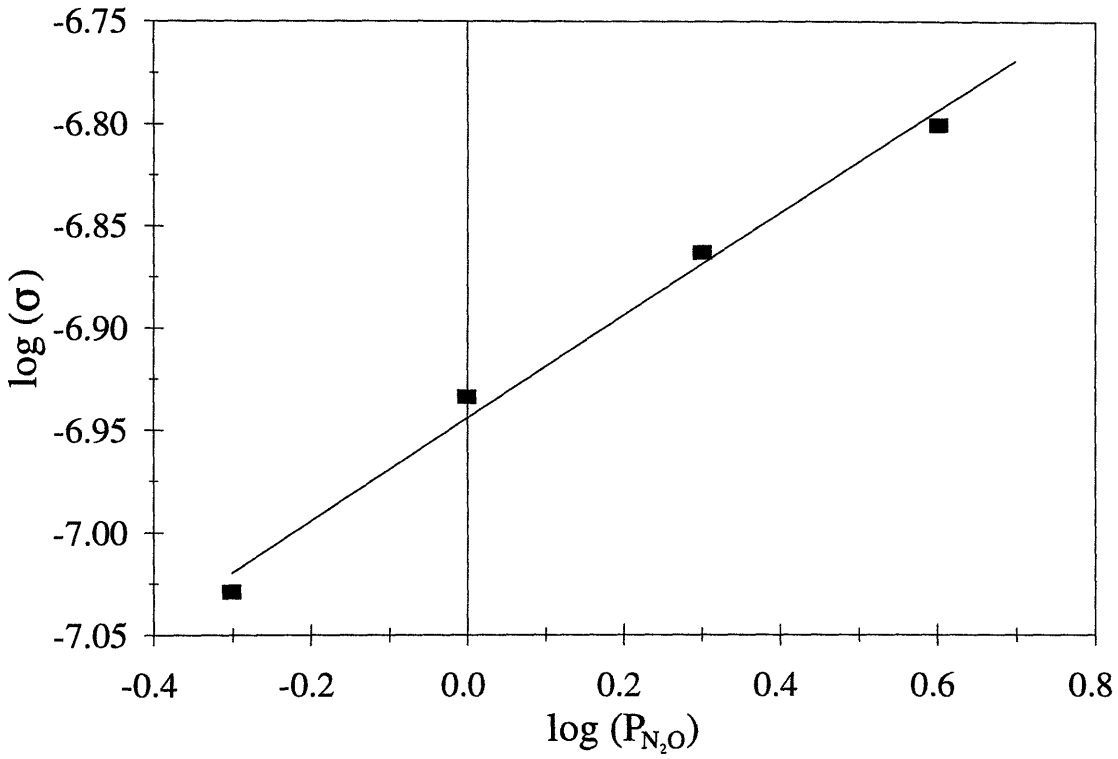

Figure 4.15. Dependence of conductivity on N_2O partial pressure (kPa) for the material having a Ni/Mo ratio of 0.75.

behavior under a N_2O atmosphere that the most Ni-rich molybdate displays under an oxygen atmosphere.

4.6.2. Correlation of Conductivity Data with Defect Structure of $Ni_{1-\delta}Mo_{1-\delta/3}O_4$

If the Ni/Mo ratio is greater than one, corresponding to an excess of NiO, the nickel molybdate exists with a net excess of cations. Based on the defect concentration relations tabulated in Table 4.7, it is proposed that these non-stoichiometric nickel molybdates have interstitial Ni atoms as the major defects that are compensated for by the presence of Mo vacancies. Given this excess of Ni atoms, it is proposed that the majority carrier arises from the oxidation of Ni^{II} to Ni^{III}, represented by the equation

$$2\,Ni_{Ni} + \frac{1}{2}O_2(g) \Leftrightarrow 2\,Ni_{Ni}^{\cdot} + O_O + V_{Ni}^{//} \qquad \textbf{(4.33)}$$

which is equivalent to Equation (4.11). If this is indeed the dominant mechanism, equation (4.13) showed that a plot of log (σ) against log (P_{O_2}) should have a slope of +1/6. As shown in Figure 4.13, the nickel molybdate having a Ni/Mo ratio of 1.5 does indeed show a +1/6 conductivity dependance on P_{O_2}.

If the Ni/Mo ratio is less than one, corresponding to an excess of MoO_3, the nickel molybdate exists with a net deficiency of cations. Based on the defect concentration relations tabulated in Table 4.7, it is proposed that these non-stoichiometric nickel molybdates have Ni vacancies as the major defects that are compensated for by either interstitial Mo atoms, or Mo atoms occupying Ni sites. Given this excess of Mo atoms, it is proposed that the majority carrier arises from the reduction of Mo^{VI} to Mo^{V}, represented by the equation

$$2\,Mo_{Mo} + O_O \Leftrightarrow \frac{1}{2}O_2(g) + V_O^{\cdot\cdot} + 2\,Mo'_{Mo} \qquad \textbf{(4.34)}$$

which is equivalent to Equation (4.8). If this is indeed the dominant mechanism, equation (4.10) showed that a plot of log (σ) against log (P_{O_2}) should have a slope of -1/4. As shown in Figure 4.13, the nickel molybdate having a Ni/Mo ratio of one does indeed show a -1/4 conductivity dependance on P_{O_2}. The conductivity dependence of the most Ni-lean molybdate shows a much stronger dependence on the partial pressure of oxygen, suggesting that Equation (4.34) is not the only reaction taking place. If the most Ni-lean molybdate is taking up oxygen in the form of lattice O^{2-} ions, the conductivity would be expected to fall as excess electrons are incorporated into the lattice in the form of O^{2-}. This mechanism may explain the change in the slope seen at $P_{O_2} = 2$ kPa, above which the structure cannot take up more oxygen.

These conductivity studies have clearly demonstrated that the conductivity of the non-stoichiometric nickel molybdates is a strong function of the defect chemistry of these materials. Given that the physical characterization of these materials has shown them to be equivalent in structure, surface area, and oxygen environment around the Mo, the differences in electronic properties of these materials provide a basis to correlate the catalytic properties of these Ni-Mo-O systems with their structure. These non-stoichiometric nickel molybdates were therefore investigated for catalytic activity towards the oxidative dehydrogenation of propane.

5. OXIDATIVE DEHYDROGENATION OF PROPANE BY NON-STOICHIOMETRIC TRANSITION METAL MOLYBDATES

The selective oxidative dehydrogenation (ODH) of lower alkanes into alkenes is a challenging problem in heterogeneous catalysis. The high bond energy of the primary C-H bond makes alkanes less reactive than the dehydrogenated alkenes. This necessitates the use of high reaction temperatures to activate the alkanes, but which can also lead to the subsequent reaction of the dehydrogenated products with the oxidant to give carbon oxides. To overcome this limitation, it is desirable to have a catalyst that is sufficiently active at low temperature for hydrogen atom abstraction from a C-H bond. The series of transition metal molybdates, the synthesis and characterization of which were discussed in Chapter 4, were tested for catalytic activity towards the oxidative dehydrogenation of propane into propene.

5.1. Experimental

5.1.1 Determination of Steady-State Activity

The catalytic activity of the materials was tested in a 1/4 inch quartz flow-through tubular reactor operated at atmospheric pressure. The reactor was contained within an electrically heated tube furnace. The temperature of the reactor was controlled according to the temperature of the gases at the base of the catalyst bed. The composition and flow rate of the gas feed mixture was measured using MKS mass flow controllers calibrated for each specific gas. Certified gas mixtures with Grade 5 helium (99.999%) as the balance gas were used throughout.

The catalyst was prepared by *in situ* calcination of the precursors. Thermogravimetric analysis showed a 14% weight loss upon calcination to 550 °C, this value being essentially independent of the Ni/Mo ratio of the precursor and the calcination atmosphere. Consequently, 116 mg of precursor were loaded into the reactor tube such that 100 mg of catalyst remained following calcination. Calcination was carried out at 550 °C for one hour under a flow of 20 ml/min He.

The reactor effluent was analyzed by gas chromatography using a Perkin Elmer Autosystem GC equipped with a TCD detector. A two-column setup was used with a 10-port sampling valve to fully separate the gases. Gases entering the GC were passed initially through a 15-foot Poropak

QS column, then a 6-foot Carbosphere column. The Carbosphere column was required to separate oxygen and carbon monoxide. After oxygen and carbon monoxide had passed through both columns, the flow direction was reversed by switching the sampling valve, thereby preventing the elution of the hydrocarbons onto the Carbosphere column. This setup resulted in good separation of the individual gases, allowing for closure of the carbon balance to within ± 5%.

In reporting catalytic data, conversion has been defined as the percentage conversion of propane into all possible products. Selectivity has been defined as the number of moles of propane converted into a specific product divided by the total number of moles of propane converted into all products, expressed as a percentage. The yield of propene has been defined as the product of the propane conversion and the selectivity towards propene, and is expressed as a percentage.

5.1.2. Determination of Transient Catalytic Behavior

The transient catalytic behavior of the series of non-stoichiometric nickel molybdates was investigated by injecting pulses of propane into a continuously flowing oxidant stream, and following the concentration of the products as a function of time. To enable this determination, the inlet to the reactor was modified to include the installation of a 6-port sampling valve, as shown in Figure 5.1. The volume of the sampling loop was 1 cm^3. The sampling valve allowed for the introduction of pulses of a desired gas, typically propane, into the reactor system. The piping between the sampling valve and the reactor was kept as short as possible to minimize the dispersion of the pulse before it reached the catalyst bed. Helium was used as the carrier gas, with the flowrate through the sampling valve controlled by a flowmeter. For the transient pulse experiments, the flowrate of the carrier gas through the sampling valve was set at 20 ml/min such that the total flow through the reactor system was 50 ml/min.

A typical pulse experiment was performed as follows. After calcining the catalyst in flowing He for one hour, N_2O (10 mol % in He) was passed through the reactor at a continuous flowrate of 15 ml/min. Nitrogen was detected in the reactor effluent following the start of the N_2O flow, but the concentration of N_2 decreased exponentially to reach a steady-state value of ~0.02% after 30 min. At this stage, the concentration of surface species on the catalyst was assumed to be at steady state. A 1 cm^3 pulse of propane (5 mol % in He) was then injected into the reactor using the sampling valve shown in Figure 5.1. Analysis of the reactor effluent was carried out at various

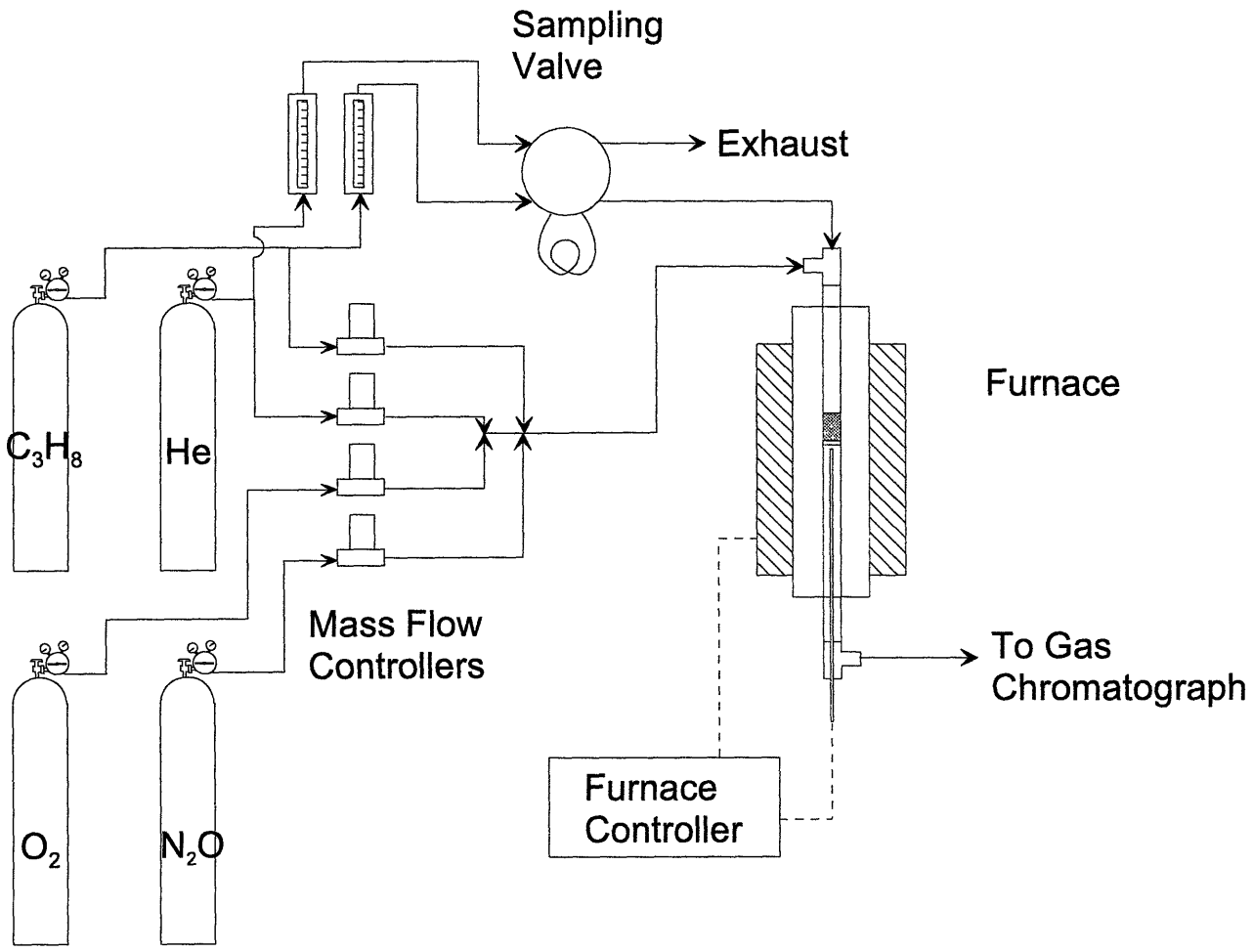

Figure 5.1. Schematic of reactor setup.

intervals after 60 seconds after injection of the pulse, the 60 second lag arising from the time required for the pulse to travel through the reactor and to the GC sampling valve. With a GC analysis time of 15 minutes, a period of ~17 minutes lapsed between successive data points, each data point being collected after a longer time interval following injection of the pulse. During this 17 minute interval between C_3H_8 pulse injections, the catalyst was under a continuous flow of oxidant and He, ensuring that steady-state surface oxygen coverage existed prior to the introduction of the pulses. After the concentration profiles had been sequentially traced out in this manner, the analysis at two arbitrary points along the curve was repeated to ensure that no deactivation of the

catalyst was taking place over the time frame of the experiment. All data points showed excellent repeatability.

For the transient pulse experiments, analysis of the reactor effluent was carried out by gas chromatography using a Perkin Elmer Autosystem GC equipped with a TCD detector. The gases entering the GC were separated using a combination of a 15-foot Poropak QS column, then a 6-foot Carbosphere column, as described in section 5.1.1. The use of nitrous oxide (N_2O) as the oxidant, however, raises the possibility of an oxygen/nitrogen separation being required. To check for the necessity of this separation, a series of pulse experiments were performed using a 6-foot Carbosphere column followed by a 5-foot Molecular Sieve 5A column to achieve separation between oxygen and nitrogen. The continued use of this arrangement of columns was, however, limited by adsorption of hydrocarbons on the molecular sieve at the low temperatures required to achieve good separation between oxygen and nitrogen. These experiments showed, however, that no oxygen was produced during the ODH of propane by nitrous oxide, thereby allowing the use of the Poropak QS/Carbosphere column arrangement.

5.2. ODH of Propane Using Oxygen as the Oxidant

The series of transition metal molybdates tested for oxidative dehydrogenation of propane produced a product spectrum limited to propene, carbon dioxide, carbon monoxide and water. No cracking products such as ethane, or oxygenated products such as aldehydes were present in the exhaust from the reactor.

5.2.1. Effect of Transition Metal in Stoichiometric Transition Metal Molybdates

Stoichiometric transition metal catalysts of the form $A_\epsilon B_{1-\epsilon}MoO_4$, where A and B are Ni, Co or Zn, and $0 \leq \epsilon \leq 1$, having the compositions detailed in Table 4.1, were tested for the ODH of propane using oxygen as the oxidant. The Zn-based catalysts showed very little activity towards the ODH of propane, suggesting that the inability of the Zn to change its oxidation state may be contributing to the lack of catalytic activity. The yield of propene attainable with nickel molybdates of the form $Ni_\epsilon Co_{1-\epsilon}MoO_4$, where $0 \leq \epsilon \leq 1$, is shown in Figure 5.2. These data were collected at 475 °C with a feed flowrate of 30 ml/min composed of 5 mol% O_2, 5 mol% C_3H_8, and the balance being He. Under these feed conditions, at temperatures of 500 °C and above, coking occurred for

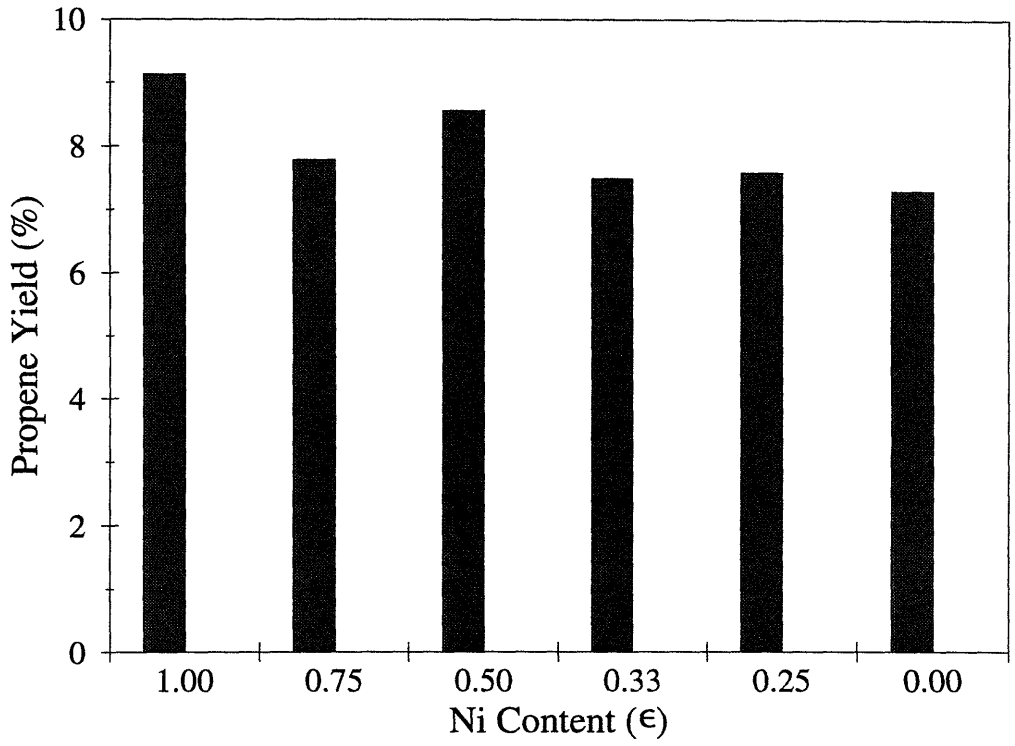

Figure 5.2. Propene yield as a function of Ni content (ϵ) for $Ni_{\epsilon}Co_{1-\epsilon}MoO_4$ catalysts.

all catalysts, with the amount of coking increasing as the Co content of the catalyst increased. The data of Figure 5.2 shows that the yield of propene for this series of stoichiometric catalysts is at a maximum for a pure nickel molybdate. While the addition of Co to the nickel molybdate increases the conversion of propane (Figure 5.3), the selectivity towards propene decreases with increasing Co content, due to increased selectivity towards CO_2 (Figure 5.4). The increase in the conversion of propane with increasing Co content reflects a higher degree of combustion under these reaction conditions, leading to the conclusion that the addition of Co to a nickel molybdate has no benefit for the maximization of propene yield. All future catalytic studies were therefore limited to the Ni-Mo-O system.

5.2.2. Effect of Non-Stoichiometry in the Ni-Mo-O System

The yield of propene attainable with nickel molybdates of the form $Ni_{1+\delta}Mo_{1-\delta/3}O_4$, where $-1/5 \leq \delta \leq 1/3$, is shown in Figure 5.5. These data were collected at 500 °C with a feed flowrate

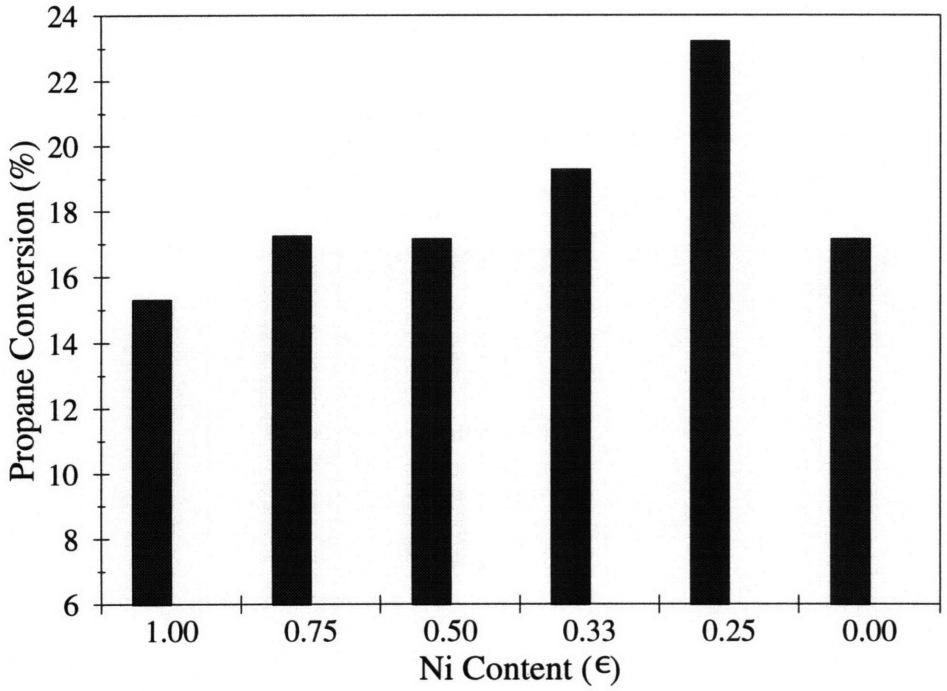

Figure 5.3. Propane conversion as a function of Ni content (ϵ) for $Ni_{\epsilon}Co_{1-\epsilon}MoO_4$ catalysts.

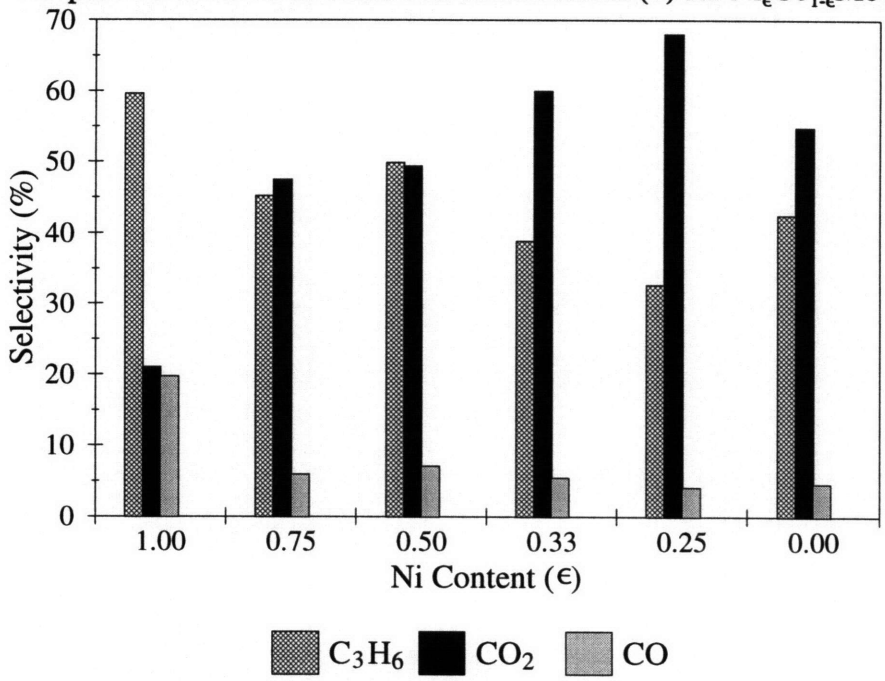

Figure 5.4. Product selectivity as a function of Ni content (ϵ) for $Ni_{\epsilon}Co_{1-\epsilon}MoO_4$ catalysts.

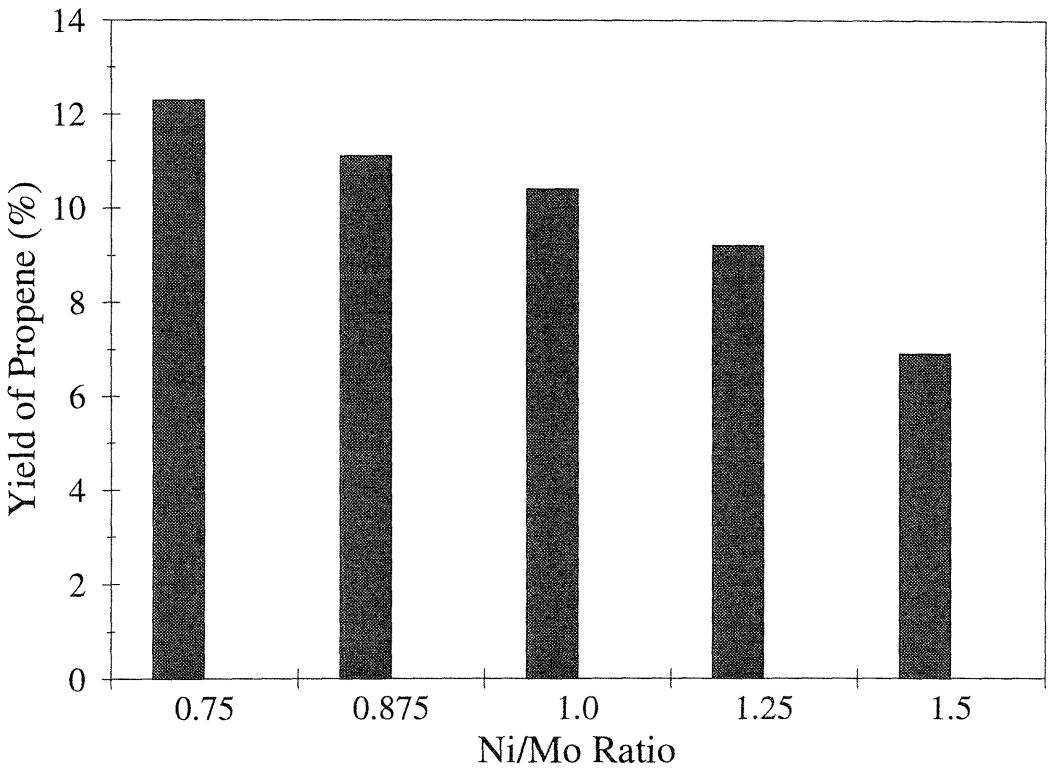

Figure 5.5. Propene yield as a function of Ni/Mo ratio.

of 30 ml/min composed of 5 mol% O_2, 5 mol% C_3H_8, and the balance being He. The data of Figure 5.5 show an increase in the yield of propene with a decrease in the nickel content of the materials. The material with the highest Ni/Mo ratio of 1.5 is a better catalyst for combustion than oxidative dehydrogenation, with approximately 60% of the product spectrum being carbon oxides. The material with the lowest Ni/Mo ratio of 0.75 has the highest activity under the reaction conditions, leading to the highest propene yield.

The series of nickel molybdate catalysts show a decrease in the selectivity towards propene with an increase in conversion. Figure 5.6 shows the selectivity towards propene at a propane conversion level of 20%. As the Ni/Mo ratio increases above 1, the selectivity towards propene decreases almost linearly as carbon oxides become the dominant products. Analysis of the defect chemistry of the Ni-Mo-O system has shown that at Ni/Mo ratios greater that one, Ni interstitials are the majority point defects. These excess Ni cations probably act as active sites for the oxidation of the dehydrogenated products, with the number of active sites therefore increasing linearly with

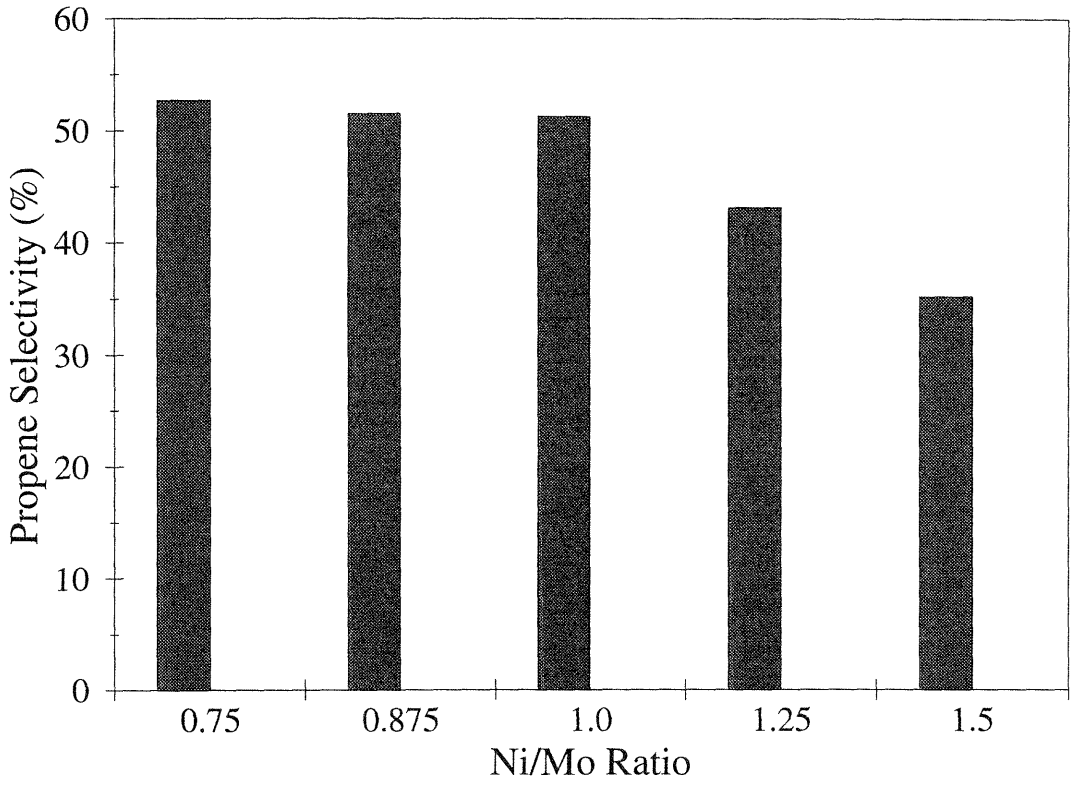

Figure 5.6. Selectivity towards propene at 20% propane conversion.

an increase in the Ni/Mo ratio. It is interesting to note, however, that the selectivity towards propene is essentially independent of the Ni/Mo ratio at values less than and equal to 1. The increase in the propene yield with decreasing Ni/Mo ratios can therefore be attributed to an increase in activity with decreasing Ni/Mo ratios.

5.2.3. Effect of Oxygen:Propane Ratio

To further improve the yield of propene attainable with the non-stoichiometric nickel molybdates, the oxygen:propane molar ratio was varied from a 1:1 ratio to an oxygen-rich 2.5:1 value. The results of this study are shown in Figure 5.7. These data were collected at 550 °C with a feed flowrate of 70 ml/min composed of 1 mol% C_3H_8, an O_2 concentration set by the ratio under investigation, and the balance being He. In an analogous set of results to the data shown in Figure 5.5 collected at a lower space velocity, the series of nickel molybdates showed an increase in propene yield with a decrease in the Ni/Mo ratio. These data also show that the propene yield

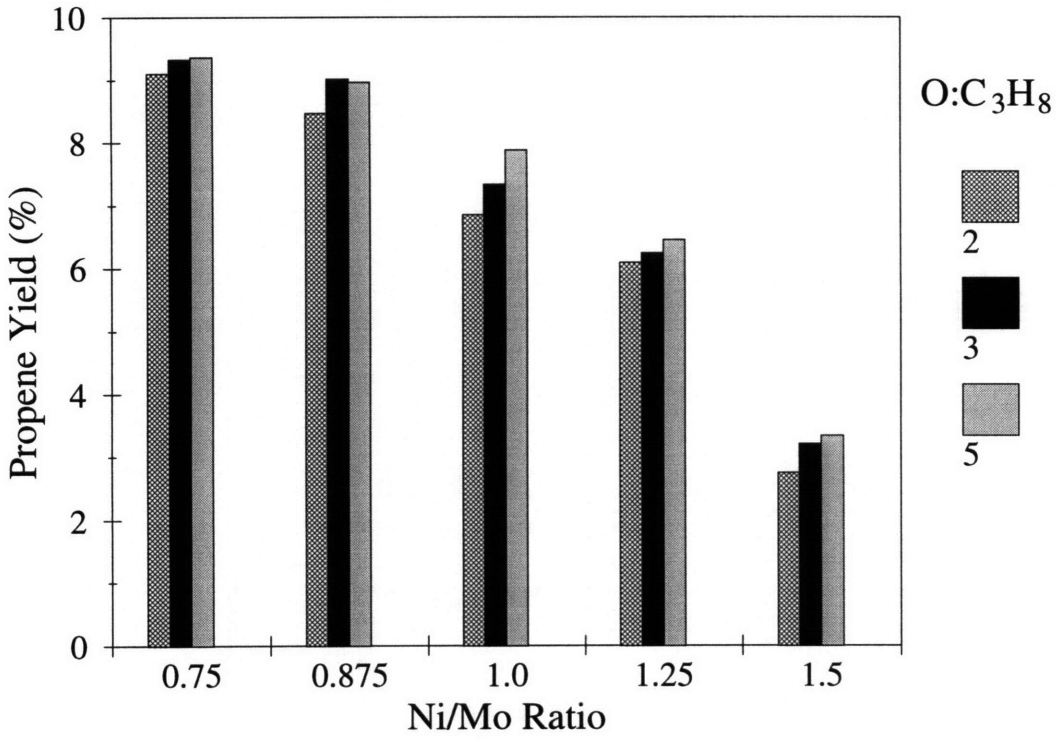

Figure 5.7. Propene yield as a function of Ni/Mo ratio and feed O_2:C_3H_8 ratio.

increases slightly as the oxygen:propane ratio increases, but with the increase becoming less significant as the Ni/Mo ratio decreases.

The effect of increasing the oxygen:propane ratio is more evident when examining the propane conversion. As shown in Figure 5.8, the propane conversion increase with increasing oxygen concentrations is significant for all Ni/Mo ratios. However, as the Ni/Mo ratio decreases, the higher conversion resulting from a higher oxygen concentration does not lead to higher propene yields due to a shift in selectivity towards carbon oxides.

5.3. ODH of Propane Using Nitrous Oxide as the Oxidant

A desirable catalytic system for the oxidative dehydrogenation of lower alkanes would provide a source of highly reactive oxygen at a temperature that minimizes further reaction of the dehydrogenated products. There has been considerable interest in the use of nitrous oxide (N_2O)

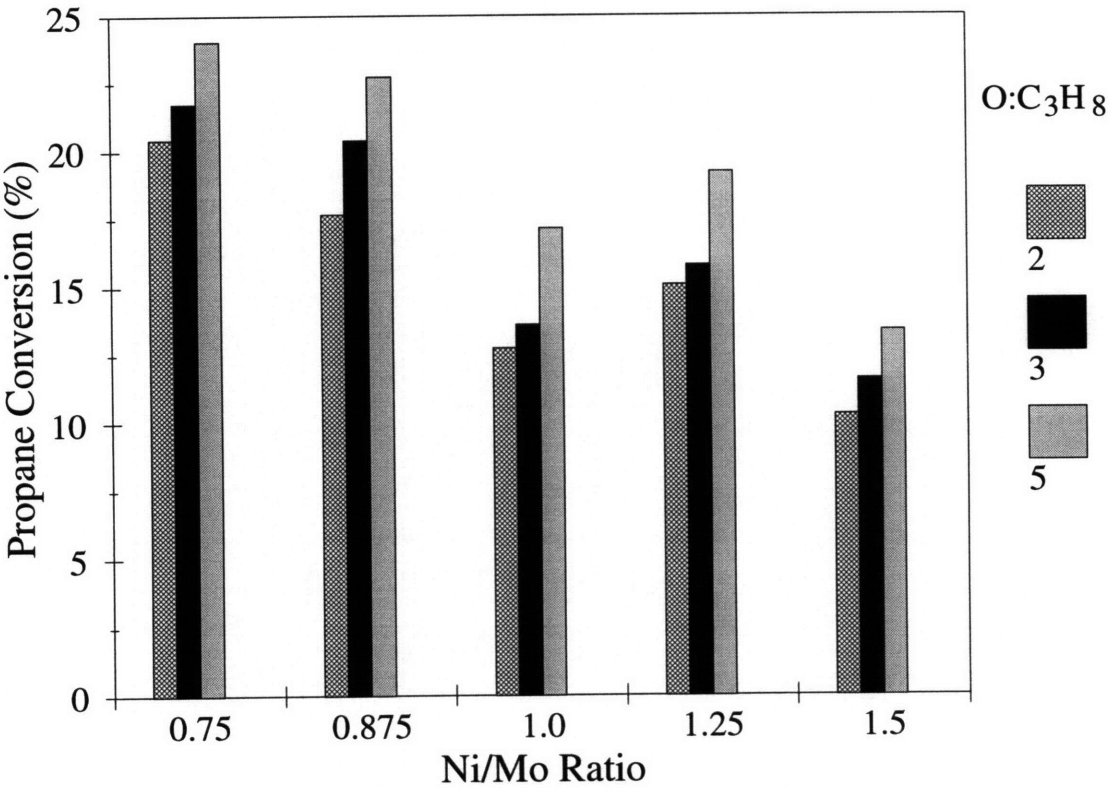

Figure 5.8. Propane conversion as a function of Ni/Mo ratio and feed O_2:C_3H_8 ratio.

as an oxidant to provide this source of reactive oxygen.[88-92] Using a silica-supported molybdenum catalyst, the partial oxidation of ethane has been investigated using N_2O as the oxidant.[88,89] Upon decomposition on the catalyst surface, N_2O provides a source of reactive O^- ions that initiate the catalytic process by hydrogen abstraction to form alkyl radicals. Spectroscopic studies have shown that these O^- ions are capable of hydrogen atom abstraction from CH_4, even at temperatures as low as -196 °C.[90] N_2O, in the presence of steam, has been shown to be able to selectively oxidize methane to methanol and formaldehyde over a silica-supported molybdenum catalyst.[90-92] On the basis of these investigations, it seemed pertinent to extend the use of N_2O as an oxidant for the selective oxidative dehydrogenation of propane.

The series of nickel molybdates tested for oxidative dehydrogenation of propane using nitrous oxide as the oxidant produced a product spectrum limited to propene, carbon dioxide, carbon monoxide, and water. No cracking products such as ethane, or oxygenated products such as aldehydes were present in the exhaust from the reactor. The use of nitrous oxide as the oxidant

produces nitrogen as a by-product, allowing a consistency check between the amount of nitrogen produced and the amount of nitrous oxide consumed.

5.3.1. Steady-State Results: Effect of Non-Stoichiometry

The yield of propene attainable with nickel molybdates of the form $Ni_{1+\delta}Mo_{1-\delta/3}O_4$, where $-1/5 \leq \delta \leq 1/3$, is shown in Figure 5.9. These data were collected at 550 °C with a feed flowrate of 70 ml/min composed of 1 mol% C_3H_8, 2 mol% N_2O, and the balance being He. The data of Figure 5.9 show that the yield of propene is independent of the Ni/Mo ratio of the materials. These results are very different from those found with oxygen as the oxidant, as shown in Figure 5.10. The catalytic results with oxygen as the oxidant were collected at the same temperature and flowrate as for those using N_2O, but with a feed composition that was 1 mol% C_3H_8, 1 mol% O_2, and balance He, to ensure that an equivalent number of oxygen atoms were present with both oxidants. In general, the propene yield with N_2O is less than with O_2, except at high Ni/Mo ratios where the selectivity towards carbon oxides increases significantly when O_2 is used as the oxidant.

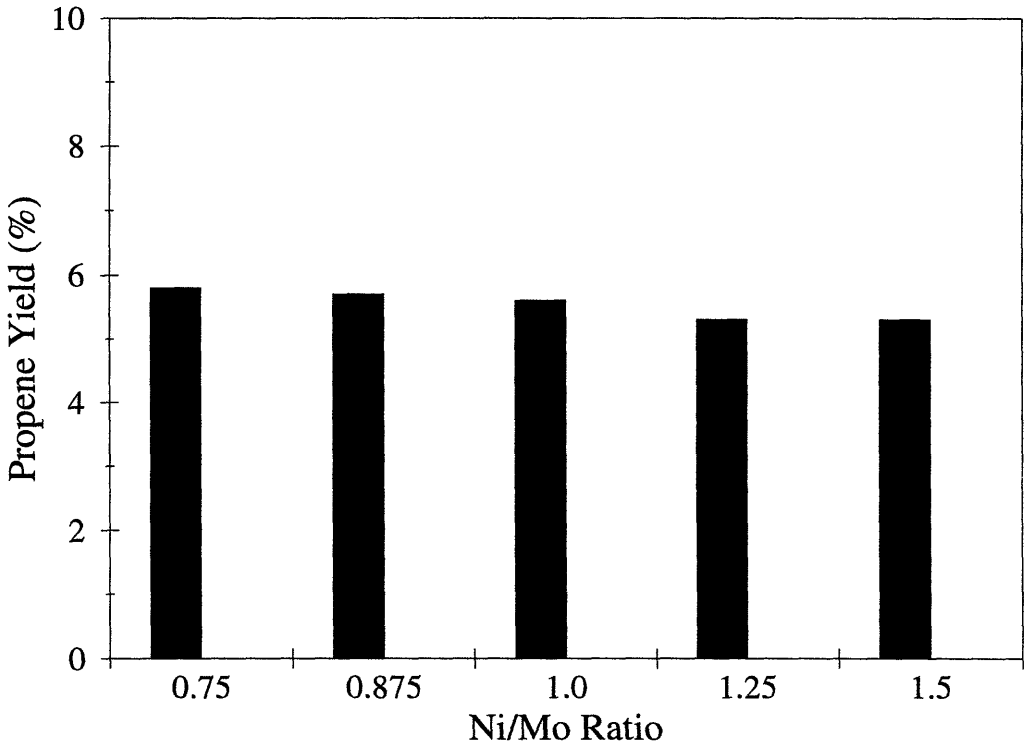

Figure 5.9. Propene yield as a function of Ni/Mo ratio.

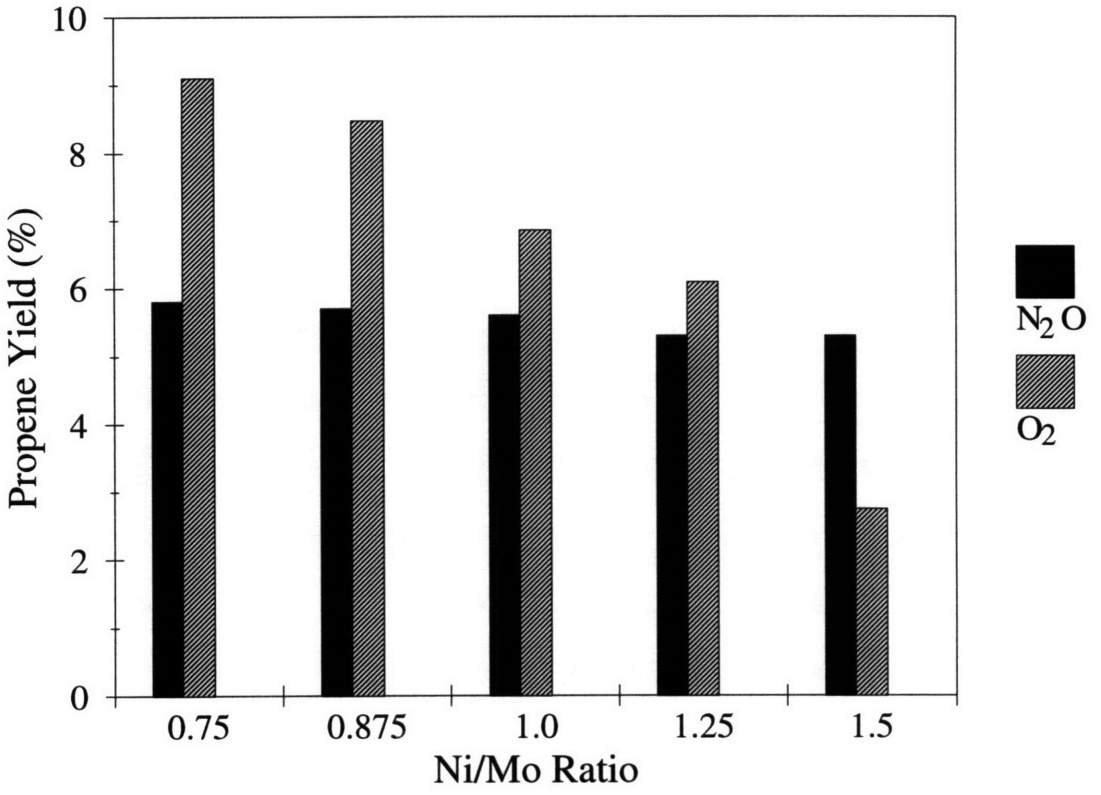

Figure 5.10. Propene yield as a function of Ni/Mo ratio for O_2 and N_2O as oxidants.

5.3.2. Effect of Nitrous Oxide:Propane Ratio

Studies using oxygen as the oxidant have shown that the yield of propene could be increased by increasing the oxidant:propane ratio. In an attempt to improve the yield of propene attainable with the non-stoichiometric nickel molybdates, the nitrous oxide:propane molar ratio was varied from a 1:1 ratio to an oxidant-rich 3:1 value. The results of this study are shown in Figure 5.11. These data were collected at 550 °C with a feed flowrate of 70 ml/min composed of 1 mol% C_3H_8, a N_2O concentration set by the ratio under investigation, and the balance being He. The series of nickel molybdates shows no significant dependence of the propene yield on the Ni/Mo ratio at all N_2O concentrations studied. These data also show that the propene yield increases as the nitrous oxide:propane ratio increases, with the expection of the sample that is most Ni-lean.

The effect of increasing the nitrous oxide:propane ratio is more evident when examining the propane conversion. As shown in Figure 5.12, the propane conversion increase with increasing N_2O

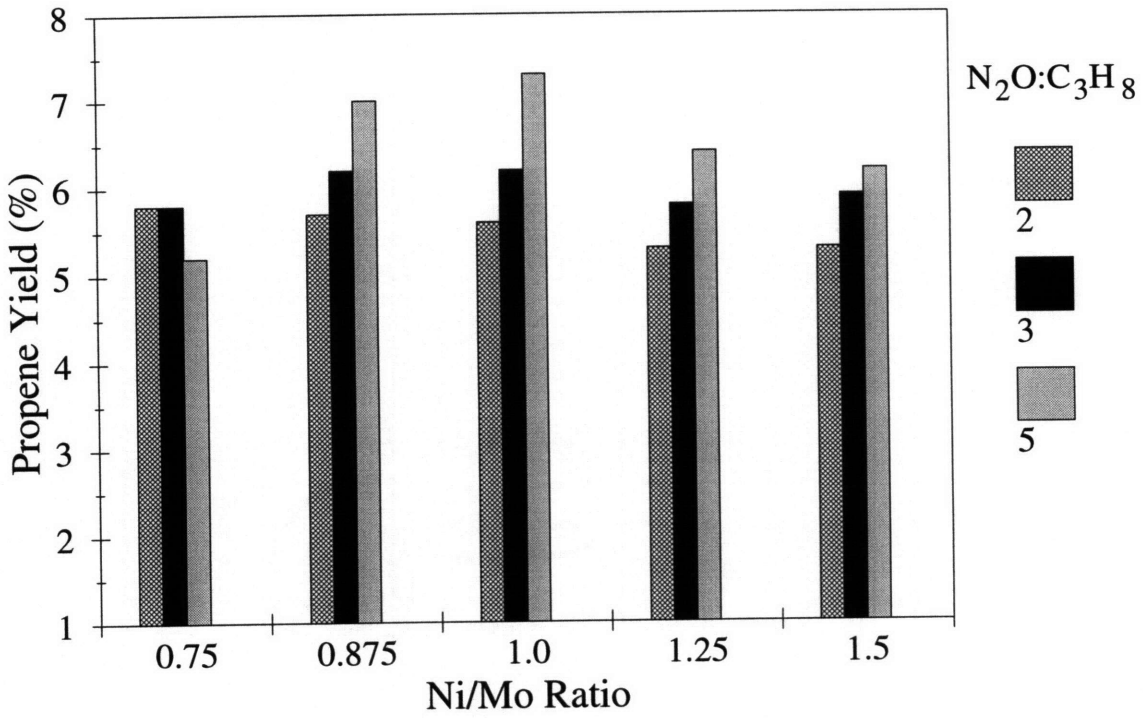

Figure 5.11. Propene yield as a function of Ni/Mo ratio and feed $N_2O:C_3H_8$ ratio.

concentrations is significant for all Ni/Mo ratios except 0.75. The reason for this difference in behavior at very low Ni/Mo ratio is unknown. The analogous set of data for oxygen as the oxidant is shown in Figure 5.7. The data in Figure 5.7 were collected at the same temperature and flowrate as for those using N_2O, but with a feed composition that ensured that an equivalent number of oxygen atoms were present with both oxidants. Comparing Figures 5.12 and 5.7 shows a fundamental difference in the behavior at the same catalyst series for the two oxidants. With N_2O as the oxidant, propane conversion increases with an increase in the Ni/Mo ratio, but decreases with increasing Ni/Mo with O_2 as the oxidant. This difference in behavior suggests that the initiation of the oxidative dehydrogenation reaction may be occurring by two different mechanisms taking place on two different sites, with the surface oxygen initiator and its associated site being dependent on the nature of the oxidant.

In an analogous manner to that with other lower alkanes, the first step in the mechanism of ODH of propane is proposed to involve the abstraction of a hydrogen to produce an alkyl radical:

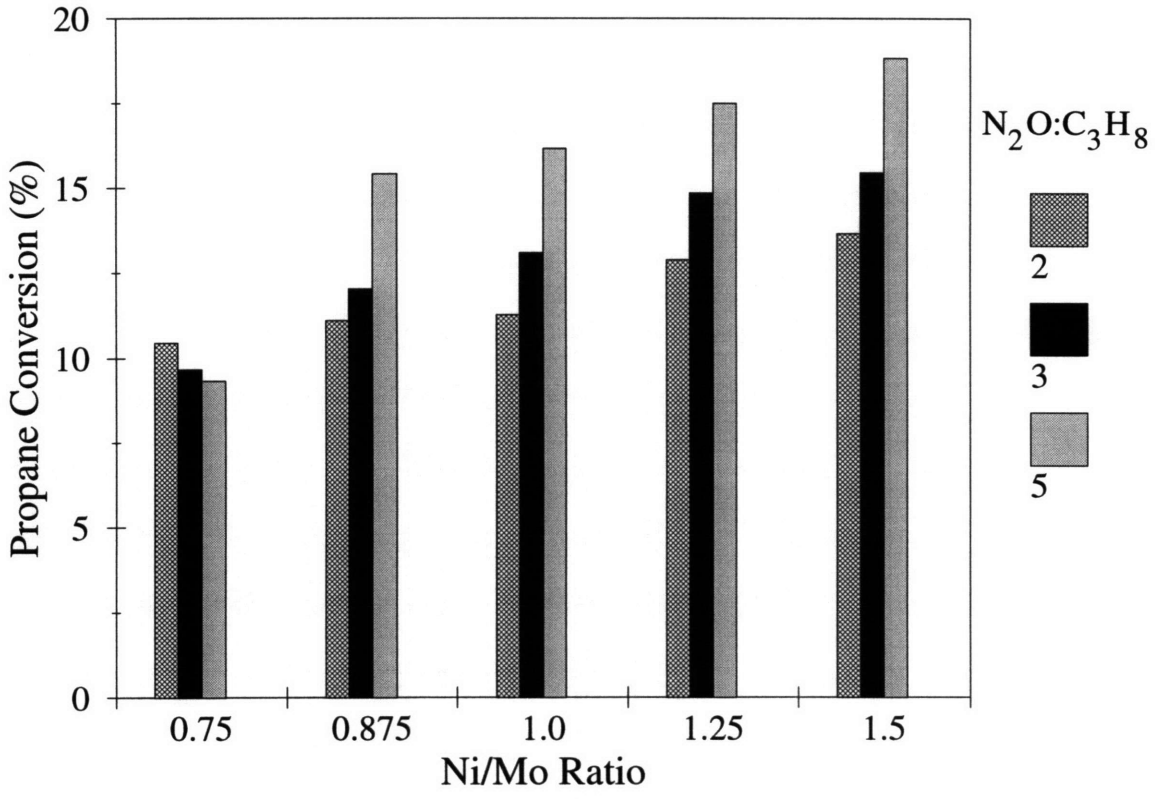

Figure 5.12. Propane conversion as a function of Ni/Mo ratio and feed N_2O:C_3H_8 ratio.

$$C_3H_8 + \text{surface oxygen species} \rightarrow C_3H_7\cdot + \text{surface hydroxyl species.} \qquad \textbf{(5.1)}$$

Using N_2O as the oxidant, the surface oxygen species is known to be O^-.[88,89] Given that with N_2O as the oxidant, the propane conversion increases with an increase in the Ni/Mo ratio, it is expected that the amount of this surface O^- species should increase with an increase in the Ni/Mo ratio, thereby increasing the rate of reaction (5.1). To gain a measure of this "concentration" of surface O^- species, a series of pulse experiments were performed using the decomposition of N_2O leading to the production of detectable N_2 as an indirect measure of the amount of O^- species being generated.

5.4. Pulse Experiments: Effect of Non-Stoichiometry

A typical profile of the concentrations of all the detectable species during a pulse experiment over $NiMoO_4$ is shown in Figure 5.13. This figure shows the formation of propene, CO and CO_2

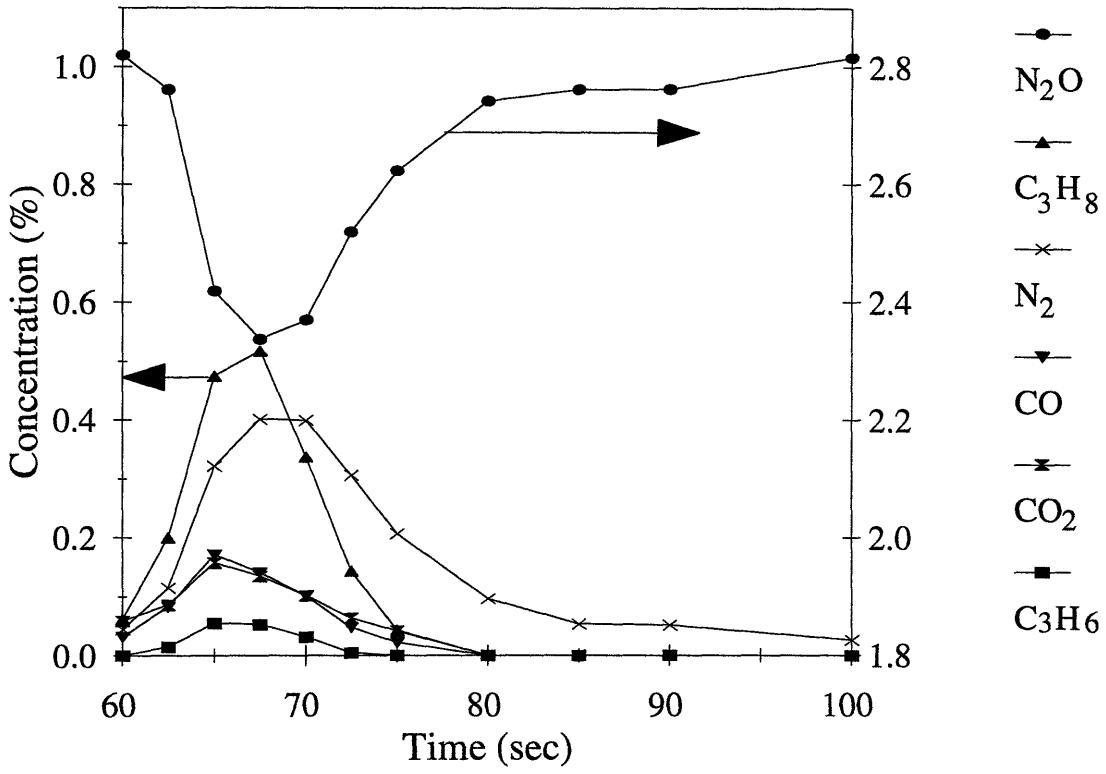

Figure 5.13. Concentration profiles of all species in pulse experiment. All species concentrations on the left-hand axis except N_2O which is on the right-hand axis.

as the propane pulse passes through the reactor. The most important feature of this figure is the fact that nitrogen is still being formed (and N_2O is correspondingly being consumed) after the hydrocarbons have cleared the reactor system. This suggests that after the propane pulse has cleared the catalyst bed, some of the continuously flowing N_2O decomposes on the catalyst surface to produce O^- ions and N_2. This process thereby rebuilds the surface concentration of O^- ions to the steady-state value prior to the introduction of the pulse. The amount of nitrogen produced thereby provides an indirect measurement of the amount of surface O^- ions being generated by the following reaction:

$$N_2O + e^- \rightarrow N_2 + O^- \qquad \textbf{(5.2)}$$

The reaction of N_2O on an active site on the catalyst surface is generally envisaged as a charge donation from the catalyst into the antibonding orbitals of N_2O, destabilizing the N-O bond and

leading to its scission forming N_2 and a surface oxygen.[87] This surface oxygen can desorb by combining with another oxygen ion, or by reacting directly with another molecule of N_2O according to the equations:

$$2\,O^- \leftrightarrow O_2 + 2\,e' \qquad \textbf{(5.3)}$$

and

$$O^- + N_2O \rightarrow N_2 + O_2 + e' \qquad \textbf{(5.4)}$$

However, no molecular oxygen was detected during the pulse experiments at any stage, including that at which nitrogen was being produced, suggesting that reactions (5.3) and (5.4) were not occurring. The presence of molecular N_2, however, confirms that N_2O decomposition is taking place via reaction (5.2) on the surface of the nickel molybdate catalysts, leading to the formation of O^-. The fact that O_2 was not produced by reactions (5.3) or (5.4) was not unexpected, since transfer of an e^- from O^- only occurs if the Fermi level of the surface is below the ionization potential of O^-, and is therefore most likely to occur in p-type materials.[93] Reactions (5.3) and (5.4) do not occur to any appreciable extent on Ni_1MoO_4, thereby suggesting that $NiMoO_4$ is an n-type material.

Figure 5.14 shows the N_2 concentration profiles for the series of nickel molybdate catalysts. This figure clearly shows that the amount of N_2, and correspondingly the amount of O^-, increases with an increase in the Ni/Mo ratio. The increase in the amount of O^- observed with increasing Ni/Mo leads to an increase in the conversion of propane, as shown in Figure 5.12. However, while the increase in the amount of O^- with increasing Ni/Mo ratio led to an increase in conversion, the propene yield was not affected, suggesting that the higher amounts of O^- results in an increase in the selectivity towards carbon oxides.

5.5. Structure/Catalytic Property Relationship

The detailed investigation into the physical characterization of the phase present under catalytic reaction conditions allows for speculation on the structure/catalytic property relationship of this class of non-stoichiometric nickel molybdates. It has been shown that a single β-phase of $Ni_{1+\delta}Mo_{1-\delta/3}O_4$ is present at 550 °C following calcination of the $(NH_4)H_{2x}Ni_{3-x}O(OH)(MoO_4)_2$ precursors. The defect chemistry of these non-stoichiometric nickel molybdates was discussed in

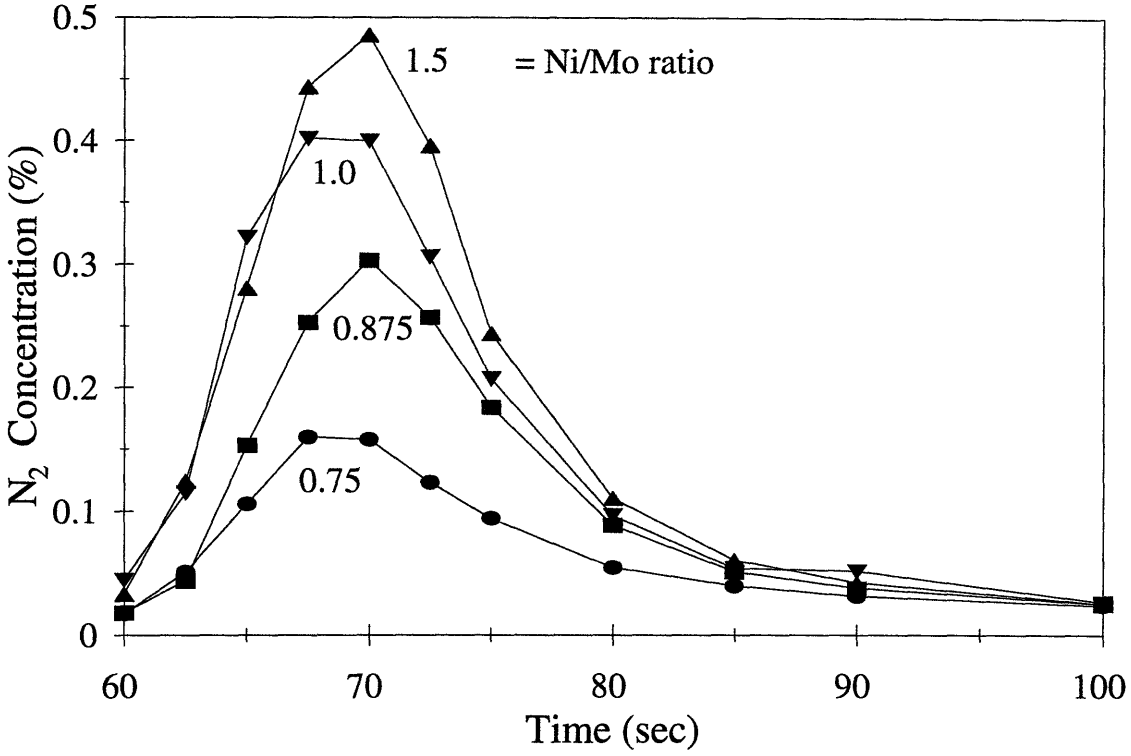

Figure 5.14. N_2 concentration profiles in pulse experiments over catalysts having a Ni/Mo ratio of 0.75 (●), 0.875 (■), 1.0 (▾), and 1.5 (▴).

Section 4.5, where the majority point defects were identified under conditions of electrical neutrality. Superimposed on this identification was a consideration of the variable valence of the cations making up these structures, leading to a correlation between the electrical conductivity and the defect structure. This correlation is summarized below.

For nickel molybdates having a Ni/Mo ratio greater than one, corresponding to an excess of NiO, the structure is proposed to have interstitial Ni atoms as the major defects that are compensated for by the presence of Mo vacancies. Given this excess of Ni atoms, it was proposed that the majority carrier arises from the oxidation of Ni^{II} to Ni^{III}, represented by the equation

$$2\,Ni_{Ni} + \frac{1}{2}O_2(g) \Leftrightarrow 2\,Ni_{Ni}^{\cdot} + O_O + V_{Ni}'' \qquad \textbf{(5.5)}$$

This formation of Ni^{III} leads to the formation of electron-acceptor levels close to the valence band, leading to hole conductivity (*p*-type semiconductor.) For nickel molybdates having a Ni/Mo ratio less than one, corresponding to an excess of MoO_3, the structure is proposed to have Ni vacancies as the major defects that are compensated for by either interstitial Mo atoms, or Mo atoms occupying Ni sites. Given this excess of Mo atoms, it was proposed that the majority carrier arises from the reduction of Mo^{VI} to Mo^{V}, represented by the equation

$$2\,Mo_{Mo} + O_O \Leftrightarrow \frac{1}{2}O_2(g) + V_O^{\cdot\cdot} + 2\,Mo_{Mo}^{/} \qquad \textbf{(5.6)}$$

This formation of Mo^{V} leads to the formation of electron-donating levels close to the conduction band, leading to electron conductivity (*n*-type semiconductor.)

Given this understanding of the defect chemistry provided by the electrical conductivity, a correlation between the electrical properties and the catalytic behavior can now be sought. Physical characterization of the catalysts has shown that all factors, except the electrical properties, are essentially identical over the Ni/Mo ratio range of 0.75 to 1.5. Therefore, differences in catalytic behavior can only be related to differences in the electrical properties. Differences in electrical properties will have an influence on the type of oxygen species that adsorb on the surface of these non-stoichiometric nickel molybdates.

It has been reported in the literature that adsorbed oxygen species transform at the surface of an oxide according to the general scheme:

$$O_{2(ads)} \rightarrow O_{2(ads)}^{-} \rightarrow O_{(ads)}^{-} \rightarrow O_{(lattice)}^{2-} \qquad \textbf{(5.7)}$$

in which they are gradually becoming richer in electrons.[94] Transition metal oxides containing cations that are capable of increasing their degree of oxidation and thereby supplying adsorbed oxygen molecules or atoms with electrons (i.e. *p*-type materials) tend to form electron-rich species such as O^- and O^{2-}. Transition metal oxides that are *n*-type in nature have a small concentration of donor centers capable of transmitting electrons to the adsorbed oxygen and tend to form oxygen species that are less rich in electrons, such as O_2^- ions.

Focusing on the nickel molybdate having a Ni/Mo ratio of 1.5 ($Ni_{1.333}Mo_{0.889}O_4$), it can be seen that both the high number of Ni atoms capable of oxidation and the low number of Mo atoms capable of reduction leads to a high number of electrons available for the formation of electron-rich species. This is confirmed by the *p*-type behavior of this material, with increasing conductivity with increasing oxygen partial pressure. It is therefore proposed that the dominant surface oxygen species on this nickel molybdate is O^-.

Turning to the nickel molybdate having a Ni/Mo ratio of 0.75 ($Ni_{0.80}Mo_{1.067}O_4$), it can be seen that both the low number of Ni atoms capable of oxidation and the high number of Mo atoms capable of reduction leads to a low number of electrons available for the formation of electron-rich species. This is confirmed by the *n*-type behavior of this material over the range of P_{O_2} used in the catalytic studies, with decreasing conductivity with increasing oxygen partial pressure. It is therefore proposed that the dominant surface oxygen species on this nickel molybdate is O_2^-.

With these two nickel molybdates forming the bounds on the range of Ni/Mo ratios possible, it can therefore be proposed that as the Ni/Mo ratio is varied through this range, the nature of the surface oxygen species changes with increasing amounts of electron-rich species as the Ni/Mo ratio increases. It must, however, be mentioned that this would only be true with O_2 as the oxidant. Since N_2O only produces one type of surface oxygen species, that being the electron-rich O^- ion, it would be expected that the nature of the surface oxygen coverage would be independent of the Ni/Mo ratio if N_2O is used as the oxidant. The amount of this electron-rich O^- species would, however, be dependent on the amount of electrons that the material is capable of donating to N_2O according to Equation (5.2). As shown in Figure 4.15, the conductivity of $Ni_{0.80}Mo_{1.067}O_4$ increases with increasing P_{N_2O}, thereby suggesting that the surface coverage of oxygen for the nickel molybdate having the lowest Ni/Mo ratio in a N_2O atmosphere is the same as the nickel molybdate having the highest Ni/Mo ratio in an O_2 atmosphere.

It has been shown that when oxygen is used as the oxidant, conversion decreases with an increase in the Ni/Mo ratio (Figure 5.7). This can be attributed to a decrease in the reactivity of the surface oxygen species as the nature of the surface oxygen coverage shifts from an O_2^- majority to an O^- majority. The catalytic data suggest that the O_2^- form of adsorbed oxygen is more reactive than O^- for H atom abstraction from propane. It is interesting to compare the conversion of propane for two different catalysts under the same conditions of temperature, space velocity, and $O:C_3H_8$

ratio, that are proposed to have the same surface oxygen coverage. The catalyst $Ni_{1.333}Mo_{0.889}O_4$ is proposed to have O^- as the majority oxygen species under an oxygen atmosphere, and the conversion of propane at 550 °C (1% C_3H_8, 1% O_2, 70 ml/min feed rate) is 10.3%. The catalyst $Ni_{0.80}Mo_{1.067}O_4$ is proposed to have O^- as the majority oxygen species under a nitrous oxide atmosphere, and the conversion of propane at 550 °C (1% C_3H_8, 2% N_2O, 70 ml/min feed rate) is 10.4%. The similarity in conversion between these two catalysts at opposite ends of the Ni/Mo ratio range suggests that under conditions of similar reactivity of the surface oxygen species, the activation of propane will be the same.

In addition to the nature or reactivity of the surface oxygen coverage, attention should also be focused on the amount of surface oxygen ions formed. This is difficult to do with O_2 as the oxidant due to the changing nature of the surface coverage. However, with N_2O as the oxidant, only one type of surface oxygen ion, that being O^-, is formed. Since the formation of this species is dependent on electron donation from the catalyst surface to N_2O, it would be expected that the higher the number of electrons available from a material, the higher the number of O^- species that should form. Since the number of electrons available increases with an increase in the Ni/Mo ratio (increasing numbers of Ni^{III} formed, decreasing numbers of Mo^V formed), it would be expected that the number of surface O^- ions formed should increase with an increase in the Ni/Mo ratio. Two sets of experimental evidence exists to confirm this proposition. In the transient pulse experiments, the amount of O^- ions formed, as indicated by the production of N_2 upon the decomposition of N_2O, was shown to increases with increasing Ni/Mo ratios (Figure 5.14). The steady-state catalytic data have shown that the conversion of propane using N_2O as the oxidant increases with an increase in the Ni/Mo ratio (Figure 5.12), indicating an increase in the number of surface oxygen species capable of H atom abstraction from the propane molecule.

In conclusion, the electronic nature of the non-stoichiometric nickel molybdate serves to influence both the nature and the extent of the oxygen surface coverage. When O_2 is used as the oxidant, the amount of electrons available for donation to adsorbed oxygen molecules decreases as the Ni/Mo ratio decreases, resulting in a more reactive oxygen surface coverage that leads to higher propane conversion. When N_2O is used as the oxidant, the amount of electrons available for donation to adsorbed N_2O molecules decreases as the Ni/Mo ratio decreases, resulting in a lower number of O^- species formed that leads to lower propane conversion.

6. CONCLUSIONS AND FUTURE DIRECTIONS

The work in this thesis describes the development of a family of transition metal molybdate catalysts that are active for the oxidative dehydrogenation of propane into propene. This thesis has focused not only on the engineering of a catalyst for this reaction, but also on the development of an understanding of the relationship between the catalyst properties and its synthesis history. The discovery of the *chimie douce* synthesis method led to the preparation of a family of layered transition metal molybdate (LTM) materials. The crystal structure solution of these layered transition metal molybdate precursors having the general formula $(NH_4)H_{2x}A_{3-x}O(OH)(MoO_4)_2$, where A is the transition metal and $0 \leq x \leq 3/2$, identified inherent non-stoichiometry in these precursors that allowed for the careful manipulation of the transition metal to molybdenum ratio. By manipulating the chemical composition of these precursors, catalysts of the form $A_{1+\delta}Mo_{1-\delta/3}O_4$, where $-1/5 \leq \delta \leq 1/3$ could be synthesized. Characterization of these catalytic phases showed similarities existed in all aspects between these materials over the full range of transition metal to molybdenum ratios possible, with the exception of their elemental composition that influenced their electronic properties. Modeling the defect chemistry of these non-stoichiometric transition metal molybdates led to the identification of the major point defects that affect the electronic properties of these materials. The electronic nature of these catalytic phases were corroborated by measurements of their conductivity using AC Impedance Spectroscopy that allowed for speculation on the nature of the surface oxygen species. Differences in the reactivity and extent of the surface oxygen coverage leads to a difference in the nature and rate of the initiating step of hydrogen atom abstraction from a C-H bond, the first step in the mechanism of oxidative dehydrogenation of lower alkanes. This difference in the reactivity of the surface oxygen coverage is manifested in the differences in the conversion of propane noted in the catalytic studies. The catalyst maximizing the yield of propene was produced by preparing a non-stoichiometric nickel molybdate with the smallest Ni/Mo ratio possible. In an oxygen environment, this catalyst is thought to have the more reactive, less electron-rich O_2^- ion as the majority species due to the small concentration of donor centers capable of transmitting electrons to the adsorbed oxygen, leading to higher conversion.

By focusing on how the processing procedures and parameters affected the structures of the various precursors and the catalyst itself, phases having optimal catalytic activity were prepared. A knowledge of the relationship between the properties and the structure of these catalyst could provide a framework for the design of new catalysts by molecular-level engineering.

Future Directions

The research covered in this thesis has raised many interesting questions on how the properties of the catalyst surface itself affects the catalytic reactions taking place on the surface. A fundamental understanding of the electronic nature of semiconducting catalysis is one area of research awaiting further exploitation. Detailed studies of the changes in the electronic properties of the surface due to changes in the oxidation states of the constituent cations making up the surface could be studied using a technique such as X-ray Photoelectron Spectroscopy. The nature of the adsorbed surface species should also be investigated in greater detail. For example, the types of negative oxygen species on the surface of the non-stoichiometric nickel molybdates could be investigated using the EPR method since all the mono- and polynuclear oxygen species, with the exception of O_2^{2-} and O^{2-} are paramagnetic. A fundamental understanding of the ability of a catalyst surface to interact with adsorbed gas molecules through the transfer of electron density will assist in the development of new catalysts having desired electronic properties.

7. REFERENCES

(1) Satterfield, C. N., "Heterogeneous Catalysis in Industrial Practice," Second Edition, McGraw-Hill, Inc., New York, 1991.

(2) Brindley, G. W., and Sempels, R. E., *Clay Minerals* **12**, 229 (1977).

(3) Lahav, N., Shani, U., and Shabti, J., *Clays Clay Minerals* **26**, 107 (1978).

(4) Pinnavaia, T. J., Tzou, M.-S., Landau, S. D., and Raythatha, R. H., *J. Molec. Catal.* **27**, 195 (1984).

(5) Occelli, M. L., and Tindwa, R. M., *Clays Clay Minerals* **31**, 22 (1983).

(6) Tokarz, M., and Shabtai, J., *Clays Clay Minerals* **33**, 89 (1985).

(7) Schutz, A., Stone, W. E. E., Poncelet, G., and Fripiat, J. J., *Clays Clay Minerals* **35,** 251 (1987).

(8) Jones, S.L., *Catalysis Today* **2**, 209 (1988).

(9) Sterte, J., *Catalysis Today* **2**, 219 (1988).

(10) Kwon, T., Tsigdinos, G. A., and Pinnavaia, T. J., *J. Am. Chem. Soc.* **110**, 3653 (1988).

(11) Kwon, T., and Pinnavaia, T. J., *Chem. Mater.* **1**, 381 (1989).

(12) Doeuff, M., Kwon, T., and Pinnavaia, T. J., *Synthetic Metals* **34**, 609 (1989).

(13) Kwon, T., Pinnavaia, T. J., *J. Molec. Catal.* **74**, 23 (1992).

(14) Wang, J., Tian, Y., Wang, R.-C., Colón, J. L., and Clearfield, A., *Mat. Res. Soc. Symp. Proc.* **233**, 63 (1991).

(15) Wang, J., Tian, Y., Wang, R.-C, and Clearfield, A., *Chem. Mater.* **4**, 1276 (1992).

(16) Drezdzon, M. A., *US Patent 4,774,212* (1988).

(17) Drezdzon, M. A., *Inorg. Chem.* **27**, 4628 (1992).

(18) Knözinger, H., *Proc. 9th Intern. Congr. Catal.*, Phillips, M. J., and Ternan, M., eds., **5**, 20, The Chemical Institute of Canada, Ottawa (1988).

(19) Cusumano, J. A., Dalla Betta, R. A., and Levy, R. B., "Catalysis in Coal Conversion", Academic Press, 1978.

(20) Callahan, J. L., Grasselli, R. K., Milberger, E. C., and Strecker, H. A., *Ind. Eng. Chem., Prod. Res. Develop.* **9**, 134 (1970).

(21) Haber, J., in "Molybdenum: An Outline of its Chemistry and Uses", Braithwaite, E. R., and Haber, J., eds., Elsevier, 477, 1994.

(22) Pezerat, H., *C. R. Acad. Sci.* **261**, 5490 (1965).

(23) Pezerat, H., Mantin, I., and Kovacevic, S., *C. R. Acad. Sci., Ser. C* **262**, 95 (1966).

(24) Pezerat, H., Mantin, I., and Kovacevic, S., *C. R. Acad. Sci., Ser. C* **263**, 60 (1966).

(25) Pezerat, H., *Bull. Soc. Fr. Mineral. Cristallogr.* **90**, 549 (1967).

(26) Pezerat, H., *C. R. Acad. Sci., Ser. C* **265**, 368 (1967).

(27) Peltre, M. J., and Pezerat, H., *J. Less Common Metals* **36**, 61 (1974).

(28) Peltre, M. J., and Pezerat, H., *J. Solid State Chem.* **23**, 19 (1978).

(29) Peltre, M. J., Olivier, D., and Pezerat, H., *J. Solid State Chem.* **24**, 57 (1978).

(30) Peltre, M. J., and Pezerat, H., *J. Solid State Chem.* **26**, 245 (1978).

(31) Clearfield, A., Sims, M. J., and Gopal, R., *Inorg. Chem.* **15**, 335 (1976).

(32) Clearfield, A., Gopal, R., and Saldarriaga-Molina, C. H., *Inorg. Chem.* **16**, 628 (1977).

(33) Clearfield, A., Moini, A., and Rudolf, P. R., *Inorg. Chem.* **24**, 4606 (1985).

(34) Moini, A., Rudolf, P. R., Clearfield, A., and Jorgensen, J. D., *Acta Cryst.* **C42**, 1667 (1986).

(35) Moini, A., Peascoe, R., Rudolf, P. R., and Clearfield, A., *Inorg. Chem.* **25**, 3782 (1986).

(36) Abrahams, S. C., and Reddy, J. M., *J. Chem. Phys.* **43**, 2533 (1965).

(37) Smith, G. W., and Ibers, J. A., *Acta. Cryst.* **19**, 269 (1965).

(38) Keeling, R. O., *Acta. Cryst.* **10**, 209 (1957).

(39) Sleight, A. W., and Chamberland, B. L., *Inorg. Chem.* **7**, 1672 (1968).

(40) Ozkan, U., Schrader, G. L., *J. Catal.* **95**, 120, 137, 147 (1985).

(41) Cavani, F., and Trifirò, F., *Catalysis Today* **24**, 307 (1995).

(42) Chaar, M. A., Patel, D., and Kung, H. H., *J. Catal.* **109**, 463 (1988).

(43) Kung, M. C., and Kung, H. H., *J. Catal.* **134**, 668 (1992).

(44) Burch, R., and Crabb, E. M., *Appl. Catal. A* **100**, 111 (1993).

(45) Corma, A., López Nieto, J. M., and Paredes, N., *J. Catal.* **144**, 425 (1993).

(46) Carrazán, S. R. G., Peres, C., Bernard, J. P., Ruwet, M., Ruiz, P., and Delmon, B., *J. Catal.* **158**, 452 (1996).

(47) Mazzocchia, C., Aboumrad, C., Diagne, C., Tempesti, E., Herrmann, J.M., and Thomas, G., *Catal. Lett.* **10**, 181 (1991).

(48) Mazzocchia, C., Anouchinsky, R., Kaddouri, A., Sautel, M., and Thomas, G., *J. Therm.*

Anal. **40**, 1253 (1993).

(49) Mazzocchia, C., Kaddouri, A., Anouchinsky, R., Sautel, M., and Thomas, G., *Solid State Ionics* **63**, 731 (1993).

(50) Minow, G., Schnabel, K., and Ohlmann, G., *React. Kinet. Catal. Lett.* **22**, 389 (1983).

(51) Hardman, H. F., *US Patent 4,255,284* (1981).

(52) Mazzocchia, C., Tempesti, E., and Aboumrad, Ch., *Fr. Patent 89-00522* (1989).

(53) Yoon, Y. S., Fujikawa, N., Ueda, W., and Moro-oka, Y., *Chem. Lett.* 1635 (1994).

(54) Mazzocchia, C., Di Renzo, F., Aboumrad, Ch., and Thomas, G., *Solid State Ionics* **32**, 228 (1989).

(55) Martin-Aranda, R. M., Portela, M. F., Madeira, L. M., Freire, F., and Oliveira, M., *Appl. Catal. A* **127**, 201 (1995).

(56) Cavani, F., Trifirò, F., and Vaccari, A., *Catalysis Today* **11**, 173 (1991).

(57) Allmann, R., *Acta Cryst.* **B24**, 972 (1968).

(58) Puxley, D. C.., Kitchener, I. J., Komodromos, C., and Parkyns, N. D., in *Preparation of Catalysts III*, Poncelet, G., Grange, P., Jacobs, P. A. (Eds), Elsevier Science, Amsterdam, 237 (1983).

(59) Sato, T., Wakabayashi, T., and Shimada, M., *Ind. Eng. Chem. Prod. Res. Dev.* **25**, 89 (1986).

(60) Rey, F., Fornés, V., and Rojo, J. M., *J. Chem. Soc. Faraday Trans.* **88**, 2233 (1992).

(61) Chibwe, K., and Jones, W., *Chem. Mater.* **1**, 489 (1989).

(62) Misra, C., and Perotta, A. J., *US Patent 5,075,089* (1991).

(63) Narita, E., Kaviratna, P., and Pinnavaia, T. J., *Chem. Lett.* 805 (1991).

(64) Chibwe, K., and Jones, W., *J. Chem. Soc., Chem. Commun.* 926 (1989).

(65) Thevenot, F., Szymanski, R., and Chaumette, P., *Clays Clay Minerals* **37**, 396 (1989).

(66) Waddington, T. C., *J. Chem. Soc.* 4340 (1958).

(67) Engelhard, G., and Michel, D., *High Resolution Solid State NMR of Silicates and Zeolites*, Wiley, New York, 1987.

(68) McKenzie, A. L., Fishel, C. T., and Davis, R. J., *J. Catal.* **138**, 547 (1992).

(69) Astier, M. P., Dji, G., and Teichner, S. J., *Ann. Chim. Fr.* **12**, 337 (1987).

(70) Cox, D. E., Hastings, J. B., Thomlinson, W., and Prewitt, C. T., *Nucl. Instr. and Meth.* **208**, 573 (1983).

(71) Sheik Saleem, S., Aruldhas, G., and Bist, H. D., *J. Solid State Chem.* **48**, 77 (1983).

(72) GSAS, General Structure Analysis System, Larson, A. C., and von Dreele, R. B., LANSCE, Los Alamos National Laboratory, copyright 1985-1994 by the Regents of the University of California

(73) O'Keeffe, M., *Struct. Bonding* **71**, 162 (1989).

(74) Brese, N.E., and O'Keeffe, M., *Acta Cryst.* **B47**, 192 (1991).

(75) O'Keeffe, M., and Brese, N.E., *J. Am. Chem. Soc.* **113**, 3226 (1991).

(76) Gutowsky, H. S., Pake, G. E., and Bersohn, R., *J. Chem. Phys.* **22**, 643 (1954).

(77) Ichikawa, M., *Acta Cryst.* **B34**, 2074 (1978).

(78) Macdonald, J. R., editor of "Impedance Spectroscopy Emphasizing Solid Materials and Systems", John Wiley & Sons, New York, 1987.

(79) Moon, P. K., Ph.D. Thesis, Massachusetts Institute of Technology, 1988.

(80) Thompson, P., Cox, D. E., and Hastings, J. B., *J. Appl. Cryst.* **20**, 79 (1987).

(81) Sheik Saleem, S., Aruldhas, G., and Bist, H. D., *J. Solid State Chem.* **48**, 77 (1983).

(82) Schmalzried, H., *Progress in Solid State Chemistry* **2**, 265 (1965).

(83) Kröger, F. A., and Vink, H. J., *Solid State Physics* **3**, 307 (1956).

(84) Sears, W. M., *Semicond. Sci. Technol.* **7**, 1464 (1992).

(85) Sears, W. M., and McIntyre, S. M., *J. Appl. Phys.* **79**, 7703 (1996).

(86) Sears, W. M., *Sensors and Actuators B* **12**, 95 (1993).

(87) Kapteijn, F., Rodriguez-Mirasol, J., and Moulijn, J. A., *Appl. Catal. B* **9**, 25 (1996).

(88) Mendelovici, L., and Lunsford, J. H., *J. Catal.* **94**, 37 (1985).

(89) Ward, M. B., Lin, M. J., and Lunsford, J. H., *J. Catal.* **50**, 306 (1977).

(90) Liu, R.-S., Iwamoto, M., and Lunsford, J. H., *J. Chem. Soc. Chem. Commun.* 78 (1982).

(91) Liu, H.-F., Liu, R.-S., Johnson, R. E., and Lunsford, J. H., *J. Am. Chem. Soc.* **106**, 4117 (1984).

(92) Khan, M. M., and Somorjai, G. A., *J. Catal.* **91**, 263 (1985).

(93) Dell, R. M., Stone, F. S., and Tiley, P. F., *Trans. Faraday Soc.* **49**, 201 (1953).

(94) Bielański, A., and Haber, J., *Catal. Rev. - Sci. Eng.* **19**, 1 (1979).